Università degli Studi di Napoli

Federico II

Doctoral Program in

PHYSICS

XXX Cycle

Coordinator: Prof. Salvatore Capozziello

Light-driven directional mass transport in azobenzene containing materials for complex textures on surfaces

Scientific and Disciplinary Sector FIS/03

Candidate
Oscurato Stefano Luigi

Tutors
Prof. Pasqualino Maddalena
Dr. Antonio Ambrosio

Years 2014/2017

...to my grandparents, living by my side and in my heart…

Abstract

Azobenzene-containing materials are one of the most investigated photo-responsive material classes over the last decades. The main reason of such huge interest is their ability to develop superficial reliefs in response to the irradiation with spatially structured optical fields in the UV/visible optical range. This phenomenon has been understood as generated by a light-driven macroscopic mass transport of the host material (typically an amorphous polymer) driven in non-trivial way by the microscopic photo-isomerization dynamics of the azobenzene molecules embedded into it. Even if the exact physical link between the light-induced molecular dynamics and the macroscopic mass displacement is still debated, some of the fingerprints of the phenomenon are fully established. The mass migration, indeed, happens only in illuminated areas of the material and it is highly directional, with a very peculiar sensitivity to the intensity and polarization distributions of the irradiating light field. Since its discovery in 1995, the possibilities offered by this effect for superficial pattering have been largely exploited and recent advances in this field are now oriented toward the realization of complex superficial textures. In the present thesis are proposed two main ideas to accomplish this complex light-driven structuration onto the azopolymer surfaces. The first idea is based on the use of complex structured intensity patterns to irradiate a plane azopolymer film. Such approach can have a two-fold relevance in the azobenzene related research fields. If, on one hand, the use of complex illumination patterns has already been demonstrated to be a fundamental tool in order to highlight new aspects of the mass migration phenomenon, on the other hand the possibility to achieve a precise control on the complex illumination patterns allows the actual employment of the azomaterials as versatile platform in photo-lithographic applications. In particular, the holographic illumination technique described in this thesis opens unprecedented possibilities in both the mentioned research areas. The second idea is instead based on the light-driven reconfiguration of azopolymer surfaces presenting a pre-patterned micro texture. In this situation the illumination pattern can be maintained as simple as conceivable, being constituted even only by a single polarized light beam. However, a great variety of three-dimensional micro-architectures can be obtained using this approach. In particular, azopolymer surfaces having a directional and reversible geometrical asymmetry are achieved by tuning few illumination parameters. These asymmetric microstructures, furthermore, have the ability to tailor

several physical macroscopic features of the surfaces, as for example the wettability properties of the azomaterial films. In this thesis is reported a detailed study of such light-controlled wettability tuning, highlighting once more the possibilities offered by this unique photo-responsive material framework for applications in many fields of science.

Preface

The research reported in this thesis has been carried out in the laboratory of Nano-Optics at the Physics Department of the University of Naples Federico II under the supervision of Prof. Pasqualino Maddalena and Dr. Antonio Ambrosio. I am very grateful to my supervisors for providing me with the opportunity and the confidence to work in the fascinating and open field of research of the azomaterials. I want to express my gratitude also to Dr. Fabio Borbone (Chemistry Department of University of Naples Federico II) for his guidance through the extensive world of the azomaterial chemistry. During fall 2015 I had the pleasure to visit the research group of Prof. Federico Capasso at Harvard University in Boston. I would acknowledge them for providing me hospitality and many new interesting scientific ideas. I wish to express also my gratitude to Prof. Arri Priimagi and his group at Tampere University of Technology. My visit at their laboratories during summer 2016 enriched significantly my global view of the scientific subjects related to the azobenzene-containing materials and triggered new research ideas hopefully leading to fruitful collaborations in the next future.

Table of contents

List of Figures

List of Tables

Introduction

Azobenzene-containing materials (or briefly azomaterials) are material systems in which the azobenzene molecules are bonded, via covalent or supramolecular interactions, to another material, typically a polymer. Many of the peculiar physical properties of this class of materials are to be attributed to the particular kinetics that the azobenzene molecules undergo when illuminated with UV and visible light. Indeed, the absorption of a photon with suitable energy (λ= 200 – 550 nm), produces cyclic structural transitions of the azomolecules between the *trans* and *cis* isomerization states. These two isomerization molecular states differ in terms of conformational geometry, occupied volume and molecular dipole moment [1–4]. More specifically, in the trans form the molecule assumes a planar rod-like configuration, with an almost zero dipole moment. In the cis form, instead, a 3D molecular configuration is realized, with a non-zero dipole moment. The interaction of the azochromophores with the irradiating light field can be described as a dipole interaction. The probability of the absorption of the photon having the proper energy depends on the reciprocal orientation of the molecular dipole moment and the actual direction of the radiation electric field ($P \sim \left|\vec{E} \cdot \vec{p}\right|^2$). This type of interaction causes a reorientation of the of free azomolecules illuminated with linearly polarized light, obtaining a final configuration in which all the molecules are aligned in the direction perpendicular to the light polarization direction [1]. Depending on the material environment, a wide variety of physical phenomena have been recognized as driven by the photoisomerization in azobenzene-containing materials. These include material anisotropy, non-linear optical response, photo-alignment of liquid crystal networks and even mechanical photo-actuation effects [1,4].

The most attractive phenomenon related to the azobenzene photo-isomerization dynamics occurs with good efficiency in solid films of amorphous azomaterials (polymers and molecular glasses) irradiated by UV/visible light. When exposed to non-uniform light patterns, the free surface of the azomaterial films is subject to a light-driven structuration which depends strongly on the intensity and the polarization distribution of the optical field over the surface. The first studies, in 1995, related to this phenomenon reported about the appearance of sinusoidal surface modulations when the azopolymer is irradiated with the sinusoidal intensity pattern produced in the

interference of two coherent light beams. The peculiar dependence of the growing rate of the inscribed *Surface Relief Gratings* (SRG) on the polarization state of the interfering beams, together with the possibility to erase the surface reliefs by shining polarized (or unpolarized) light [5] and eventually rewrite them with a new interference pattern, have allowed to reject any hypothesis which would ascribe the surface modulation to some destructive phenomena (e.g. material ablation) [6,7]. Indeed, the phenomenon occurs at light intensity much smaller than that necessary for ablation and for temperatures well below the glass transition temperature T_g of the polymers. On the contrary, the surface structuration has been found to arise from a macroscopic light-driven material transport, initiated by the intricate dynamics of the azomolecules embedded in the material matrix. Once the main aspects of the surface structuration have been phenomenologically understood, a huge variety of different illumination schemes and engineered azomaterials have been proposed over the years to achieve efficient surface relief inscription [8–11]. At the present, this phenomenon represents a valid technique for complex surface structuring and it has found applications in many technological areas as surface engineering [3,12], photonics [4,13] and biology [14], among the others. However, despite the huge diffusion of the azomaterials in application-oriented experiments, a complete fundamental understanding of the microscopic physical mechanism driving the peculiar macroscopic material motion is still lacking. While the mass migration is recognized to be initiated certainly by the photoisomerization dynamics of the azochromophores, none of the microscopic models [15–20] proposed over the years is able to unambiguously and quantitatively relate the dynamics at the micro and nanoscale to the directional motion at the macroscale of the azopolymers. The use of spatially structured complex illumination patterns has revealed to be a tool of crucial importance to elucidate some fundamental aspects of the phenomenon. The most clear example is represented by the spiral surface reliefs inscribed into the azopolymer films under irradiation of focused optical vortex beam [8]. Very recently, the study of these peculiar surface reliefs allowed the development of a phenomenological model for the mass transport which is gaining increasingly importance for the description of many surface topographies obtained in non-standard illumination conditions.

The ability in precisely control the intensity pattern of the irradiating light can give new chances not only for the studies at fundamental level, but also in practical applications. At this aim, the use of Computer-Generated Holograms (CGH) [21] is certainly a very promising approach to generate almost arbitrary illumination patterns, opening to a more inclusive use of the complex surface reliefs inscribed onto the azopolymer films in the field of the photo-lithography. The access to complex

superficial topographies onto the azomaterial films does not necessitate always the use of complex illumination schemes. Even the quasi-homogeneous field of an expanded Gaussian beam can induce complex topographies onto the surface. Indeed, while the irradiation of an homogenous light field is able to inscribe periodic surface modulations (the *Spontaneous Surface Relief Gratings*, SSRG) onto the surface of flat azopolymer films [22], the same illumination condition produces complex superficial textures if the azopolymer surface is pre-structured in form of an array of micro-posts [3,10,23]. In this situation, the directional dependence of the azomaterial displacement can be used to control the degree of asymmetry that the light-reconfigured microstructures confer to the surface. In this way, macroscopic physical properties as the adhesion and the wetting properties can be finely tuned by controlling the irradiation conditions [12].

The present thesis moves in this application-oriented field of research, where the complex light-induced surfaces of azomaterials are gaining more and more relevance. Also the potential perspectives offered by the interaction of the complex illumination fields with the azomaterial surfaces toward the understanding of the mass migration phenomenon at the fundamental level are not left out from the discussion conducted in the thesis. The work presented herein is the result of the efforts that I and my group made in the last years toward the investigation of the mass migration phenomenon and its possible applications, in both well-established and new experimental situations. For this reason, the thesis contains experimental data about new illumination approaches (as the use of computer-generated holographic intensity patterns), peculiar surface reliefs obtained in non-standard illumination conditions and specific applications (the wettability tailoring of the azopolymer surfaces). Furthermore, whenever it was possible, our own experimental data concerning also the standard illumination configurations (as the SRG, the SSRG and the surface reliefs arising from focused Gaussian beams) were included and discussed.

The compendium of this thesis is organized as follows: Chapter 1 gives a description of the photochemistry and of the photo-initiated dynamics of the azobenzene molecules. The main aspects of the light-induced mass migration occurring in azobenzene-containing materials under standard illumination conditions are also discussed here, together with an overview on the existing theoretical models describing light-driven macroscopic phenomenon. The peculiar spiral-shaped surface reliefs and the reason why they cannot be explained by the standard mass migration models are presented in the last paragraph of this chapter. In Chapter 2, the description of the phenomenological mass migration model able to correctly predict the spirals is given. The agreement between the predictions of this model and the experimental peculiar surface reliefs obtained onto the azopolymer surface are used here to characterize two

light-modulating devices, namely a spin-to-orbit angular momentum converter and the commercial θ-cell used to produce radially and azimuthally polarized beams. In Chapter 3, the principles of the computer-generated holography and the complex surface reliefs achievable in this illumination technique are extensively discussed. Chapter 4 gives an overview on the superficial textures achieved by the irradiation of azopolymer films with a single uniform light beam. In particular, the structures obtained by the light-driven reconfiguration of superficial pre-patterned micro-architectures are experimentally characterized and, accordingly to the recent literature, interpreted in the same theoretical framework of the phenomenological model presented in chapter 2. In Chapter 5 the wettability properties of such light-reconfigured surfaces are presented. An overview on the geometry-driven wettability is given for both the situations well-described by standard thermodynamic models and for few situations which requires new extended models. This is the case of the array of our azopolymer microstructures, which necessitates the inclusion of other parameters describing the actual geometry of the superficial roughness, instead of just quantifying the extent of the wetted surface area as needed by the thermodynamic models, to correctly interpret the values of the water contact angle observed experimentally. The wide range of possibilities offered by the mass migration phenomenon in wettability non-trivial applications is also presented. The Conclusions and the future outlooks are finally presented. Appendix A contains the description of the properties of the azopolymer used in all the experiments presented in the thesis.

1 The light-induced mass migration in azobenzene-containing materials

The azobenzene molecule is a two-state system characterized by trans and cis isomerization forms differing significantly in terms of conformational structure, occupied volume and molecular dipole moment. The illumination of an azomolecule with UV/Visible light is able to trigger both the trans-cis and cis-trans transitions and produces cyclic trans-cis-trans photo-isomerizations which make the azomoieties a peculiar photo-responsive system. Following the division originally proposed by Natanshon and Rochon [1], this microscopic photo-induced motion constitutes the base-level of a series of movements occurring at different length scales in the material systems incorporating the azochromophores. These movements involve the amplification of the processes at molecular level by the cooperative interactions of the azomolecules between themselves and with the environment of the host material, and also a very intriguing phenomenon: the light-induced macroscopic mass-migration. Under proper illumination conditions, the free surface of the azomaterials in form of thin films develops topographic modulations as consequence of this light-driven mass transport. The inscribed surface reliefs depend on the intensity distribution and the polarization state of the irradiating light. The present chapter focuses mainly on the description of the characteristics of this light-induced phenomenon and of the peculiar surface reliefs resulting from it. Even if a complete theoretical framework able to relate the many experiment facets of the light-induced material transport to the azobenzene dynamics at molecular scale is still lacking, an overview of the several mass-migration models, valid in some simple illumination conditions, is also given. Finally, the inadequacy of these models in describing complex illumination conditions is highlighted through the phenomenology related to recently observed spiral-shaped surface reliefs, which are described in the last paragraph of the chapter.

1.1 Azobenzene photochemistry and molecular dynamics

1.1.1 The photo-isomerization reactions

The term azomolecules is commonly used to identify the class of molecules comprising the parent azobenzene molecule and the entire set of substituted compounds obtained from it. The chemical architecture of the azomolecules (Figure 1.1) is characterized by two phenyl rings linked together through the azo bond $(-\mathrm{N}=\mathrm{N}-)$ [1,2,24]. When excited by a photon of suitable energy ($\lambda = 200 - 550$ nm), an azomolecule can be switched between two distinct molecular isomerization states having different optical, electronic and electrochemical properties. The two states are the thermodynamically stable *trans* isomer (Figure 1.1 (a)) and the meta-stable *cis* isomer (Figure 1.1 (b)).

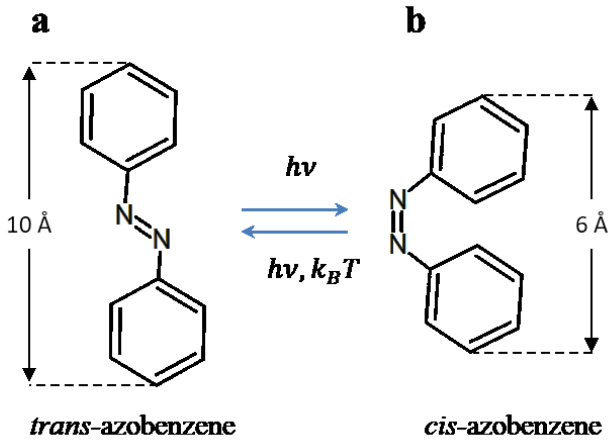

Figure 1.1| The two isomerization states of the azobenzene molecules. Conformational structures of the thermodynamically stable trans-isomer (a) and of the meta-sable cis-isomer (b). The absorption of photons in the UV/visible range can initiate both the isomerization reactions, giving rise to photo-isomerization cycles.

The absorption of a photon with energy matching the *trans*-isomer absorption band switches the molecule in the *cis* state. This can return to the trans state either by a thermal relaxation or by a new photo-induced isomerization process through the absorption of a photon in its absorption band. The overlap in terms of wavelength between the absorption bands of the two isomers can be controlled by properly choosing the substituent groups in the azomolecules [2]. In this way, the molecule can be

designed to behave either as photo-switchable two-state system (if the absorption bands of the two isomers are sufficiently separated), or to give rise to photo-isomerization cycles between the trans and cis forms. In this last case, a significant overlap between the absorption bands is desirable so that the irradiation of a photon with a given energy is able to trigger simultaneously the photo-isomerization reactions [1,2,24] in both directions. The photo-induced isomerization cycles obtained in the last type of azomolecules has been found to initiate some peculiar phenomena in material systems containing the azomolecules, as the molecular photo-alignment, the optically driven mechanical actuation and the light-induced material transport.

The photo-isomerization reaction, occurs on a time-scale of few picoseconds [2,25], and involves the bending of the phenyl rings around the azo bond. This movement implies a significant change in the size and in the spatial conformation of the molecule. The isomerization conversion reduces the distance between the phenyl rings from approximately 10Å to 6Å (Figure 1.2(a)) and results also in a change of the molecular dipole from $p_{trans} \approx 0$ Debye to $p_{cis} = 3$ Debye [26,27]. The two isomers differ also in terms of occupied volume, requiring a free volume of about 30 nm^3 [2] in order that the photo-isomerization reaction takes place. This volume variation generates a significant force at the nanoscale [28] which can be even transferred in a macroscopic actuation when the molecules are embedded in a host material matrix [29].

1.1.2 The light-induced photo-alignment

The molecular motion of the cyclically isomerizing azomolecules can give rise to the photo-alignment of the molecules when they are illuminated with linearly polarized light. This situation is presented schematically in Figure 1.2 and is due to the enhanced absorption probability, and hence a more efficient photo-isomerization dynamics, for the molecules illuminated with light polarized in the direction parallel to the molecular transition dipole (which is oriented along the molecular main axis for the trans-isomer).

More specifically, regarding the light absorption as a dipole interaction, the excitation probability varies as $cos^2\varphi$, where φ is the angle between the electric field of the polarized light and the molecular dipole direction. This implies maximum absorption efficiency for the molecules aligned in the light polarization direction, whereas the molecules oriented at 90° respect to the polarization direction will not absorb light efficiently. A trans azomolecule which has successfully absorbed a photon starts a photo-isomerization reaction which, after an isomerization cycle, brings back the molecule again in the trans state (Figure 1.2(a)). The orientation of its molecular

axis, however, changes randomly and there is a non-zero probability that after a certain number of isomerization cycles, it results oriented in the direction orthogonal to the light polarization direction. As in this case the probability to undergo a new isomerization cycle by the absorption of a new photon is low, this molecule remain oriented in the direction orthogonal to the polarization even if the light irradiation continues (Figure 1.2(a)). Considering the ensemble of azomolecules in a material system, the result of this orientational alignment is that after many isomerization cycles there is the depletion of the population of trans-molecules oriented parallel to the polarization and the concomitant enrichment of the population of molecules in the perpendicular direction (Figure 1.2(b)).

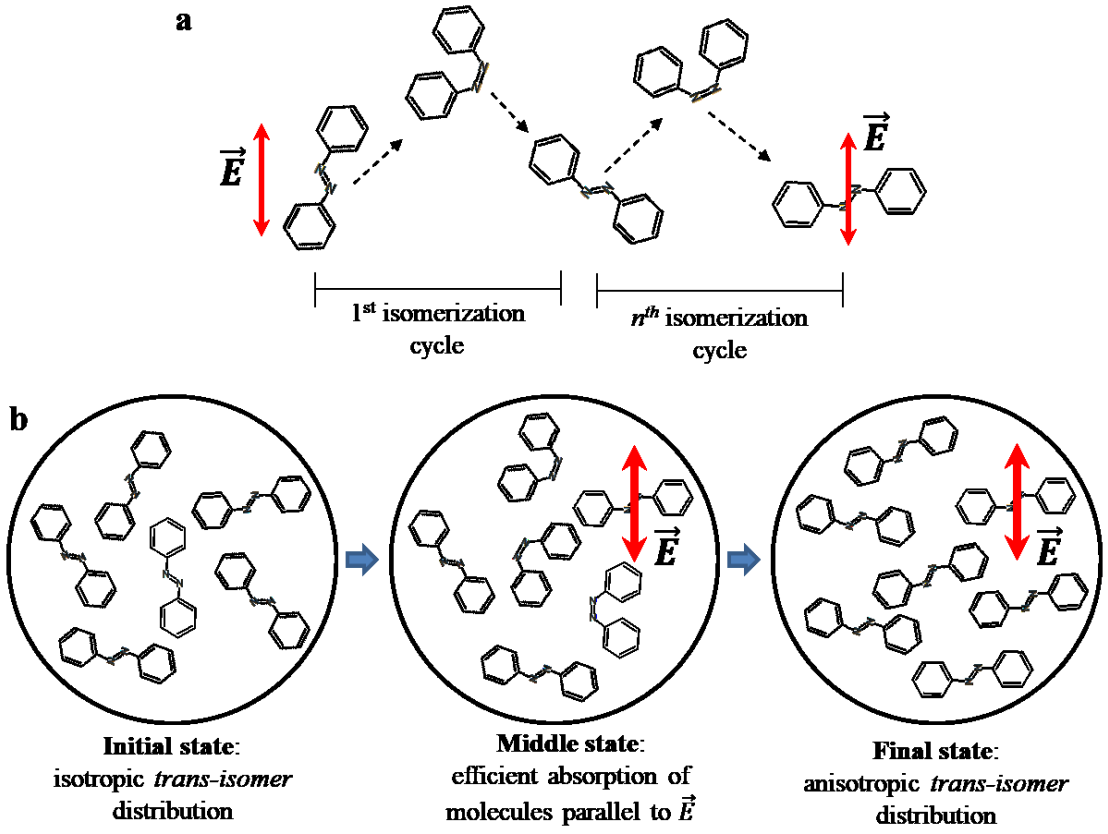

Figure 1.2| Azobenzene photoinduced alignment. (a) Stochastic photo-alignment process of the azomolecules irradiated by linearly polarized light. (b) Enrichment of azomolecules population aligned in the direction perpendicular to the light polarization as the irradiation process proceeds.

The photo-orientation effect of the azomolecules under linearly polarized light irradiation is commonly referred as orientational *hole-burning*, and gives rise to strong birefringence and dichroism in material systems containing the azo-moieties [1,2]. Furthermore, this molecular photo-alignment is reversible and reconfigurable: a new orientational alignment can be induced in a new desired direction of the material plane simply by a rotation of the irradiating linear polarization direction. Eventually, even the initial isotropic molecular distribution can be easily restored by the irradiation of circularly polarized or non-polarized light.

1.1.3 Cooperative motion in azomaterials

The dynamics at the molecular scale can be greatly amplified through the collaborative motions of many azomolecules interacting in a material matrix. A simple example is constituted by the liquid-crystalline azopolymers, where the photo-alignment of the azomolecules can be used to orient (even in a reversible way) the entire polymer matrix, giving rise to liquid-crystalline to isotropic phase transitions [30,31]. The reorientation of the azomolecules is also the key factor in the applications related to the optical-to-mechanical energy conversion induced in liquid crystals elastomers (LCE) by the photo-induced molecular dynamics [32–34]. In particular, this class of photo-responsive azomaterials is currently finding many applications in the emerging field of the light-driven bioinspired research [35,36].

However, the most fascinating phenomenon related to the photo-response of the azobenzene-containing materials is the photo-induced material mass transport, occurring with good efficiency especially in amorphous material systems. In these materials, where the azochromophores are bonded through covalent or supramolecular interactions to the host material matrix (azopolymers, supramolecular azopolymers, molecular glasses, etc. [3,4]), the microscopic molecular dynamics actuated by the light irradiation discussed so far, leads to an ensemble of complex interactions of the azomolecules with the material environment that results in the rising of surface relief patterns onto the free surface of the azomaterial in the form of thin films. The main features of the light-induced mass migration phenomenon and the superficial modulations it generates onto the free surface of the azomaterial films are discussed in the next paragraph.

1.2 The directional mass migration in azomaterials

1.2.1 The Surface Relief Gratings

In 1995, Natanshon and Rochon [6], and independently Kim et al [7], reported about the large-scale periodic modulations induced onto the free surface of an azopolymer thin film under irradiation with a light interference pattern. They found that in response to the sinusoidal spatially modulated intensity pattern, the polymer surface develops a texture which replicates the pattern of the incident irradiation in form of sinusoidal surface reliefs that now are commonly identified as *Surface Relief Gratings* (SRG). The surface modulation was found to happen at very low irradiation intensities, allowing to discard any explanation of the polymer structuration in terms of the ablative or destructive processes [37]. On the contrary, the phenomenon was understood as a real material movement, induced by the irradiating light at temperatures significantly lower than the glass transition temperature T_g of the amorphous azomaterial. The non-destructive nature of the phenomenon was also confirmed by the possibility of erasing the superficial modulations either by rising the temperature above T_g or by irradiating the SRG with circularly polarized and non-polarized light [5,38].

The typical experimental configuration used for the inscription of the surface relief gratings in azomaterials is schematized in Figure 1.3(a). In particular, taking advantage from the description of the SRG inscribed onto the azopolymer we have used for all the experiments reported in this thesis (see Appendix A for details about its chemical structure and absorption spectrum), the images presented in Figure 1.3 allow to highlight another very peculiar feature of the phenomenon: the dependence on the irradiating light polarization of the light-induced mass migration.

In the SRG inscription experiment, two coherent coplanar laser beams, having a wavelength $\lambda = 488\,nm$ in the overlapping absorption bands of the trans and cis azomolecules of the azopolymer, interfere in the azopolymer film plane. The polarization state of the two beams is chosen alternatively as p-p or s-s in order to have a sinusoidal spatially modulated intensity over the sample, while intensity of the two beams during the experiment is about $20\ mW/cm^2$. The AFM images of the surface reliefs obtained onto the polymer for 1h irradiation time in these two illumination conditions are shown in Figure 1.3(b) and Figure 1.3(c), respectively. From the comparison of these images, it emerges that while the p-p polarization configuration gives rise to a topographical modulation in the range of several hundred of nanometers (Figure 1.3(b)), the illumination of the film with s-s polarized beams produces only small modulations of the azopolymer surface (Figure 1.3(c)).

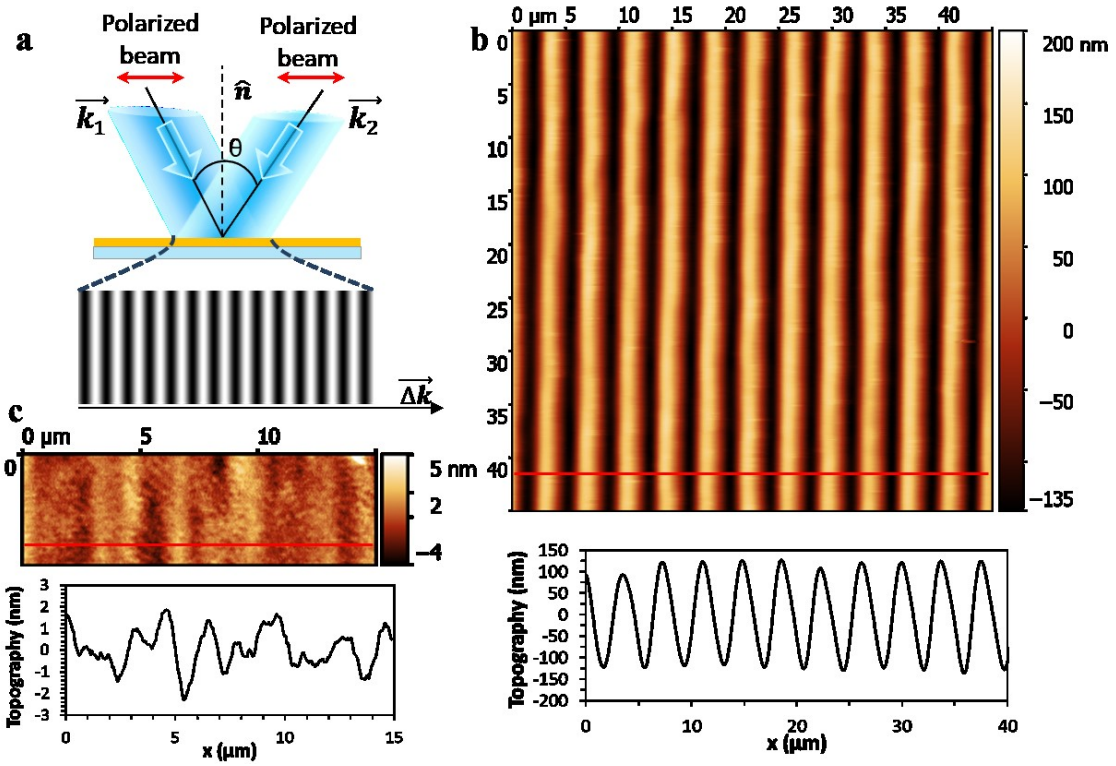

Figure 1.3| Surface relief gratings induced onto the azopolymer film surface under two-beam interference irradiation. (a) Schematic representation of the typical experimental situation for SRG inscription. The illumination pattern is the spatially modulated interference pattern generated by two polarized (in this case) laser beams. (b) AFM image (top) and topography profile measured along the red line (bottom) of the superficial modulation resulting from the polymer irradiation with p-p polarized beams. (c) Same as in (b) but with irradiation of s-s polarized interference pattern. The beam intensity during the exposure is $\sim 20\ mW/cm^2$.

The polarization dependence of the SRG inscription efficiency shown here resulted clear since the first experiments about the light-driven mass migration phenomenon [4]. In particular, it has suggested that the presence of both a spatially varying intensity pattern and the simultaneous non-vanishing component of the optical electric field in the direction of the intensity gradient are necessary to have an efficient material movement. This condition is indeed verified in the case of the interfering p-p polarized beams, while it does not occur for the case of s-s polarized, where the intensity gradient and the electric field are oriented in perpendicular directions. The differences in the SRG inscription efficiencies imply a directionality of the material displacement, which took place with good efficiency only in the direction parallel to the light polarization, while it is mostly inhibited in the direction perpendicular to it.

This type of considerations about the SRG inscription processes and its efficiency are also typically derived by the analysis of the measurements of diffraction experiments, where a light beam having a wavelength outside the azomolecule absorption band is used to monitor in real-time the diffraction that the periodic SRG's growth produces. However, both the topographic characterization of the surface modulations by a-posteriori AFM measurements (as performed in the case of Figure 1.3(b)) and the monitoring of the SRG growth with diffraction experiments do not allow the understanding of the phase relation existing between the positions of the maxima in the intensity pattern and the position of the resulting crests in the surface topography.

1.2.2 Surface reliefs from focused light beams

Before the development of recent AFM setups able to monitor *in-situ* and simultaneously both the intensity pattern and the superficial topography [39–42], crucial experiments toward the understanding of the directional properties of the light-fueled material movement made use of spatially confined intensity patterns. An example of such patterns is represented by a polarized gaussian laser beam, focused onto the azopolymer film [17,43] through an high numerical aperture objective, as schematized in Figure 1.4(a).

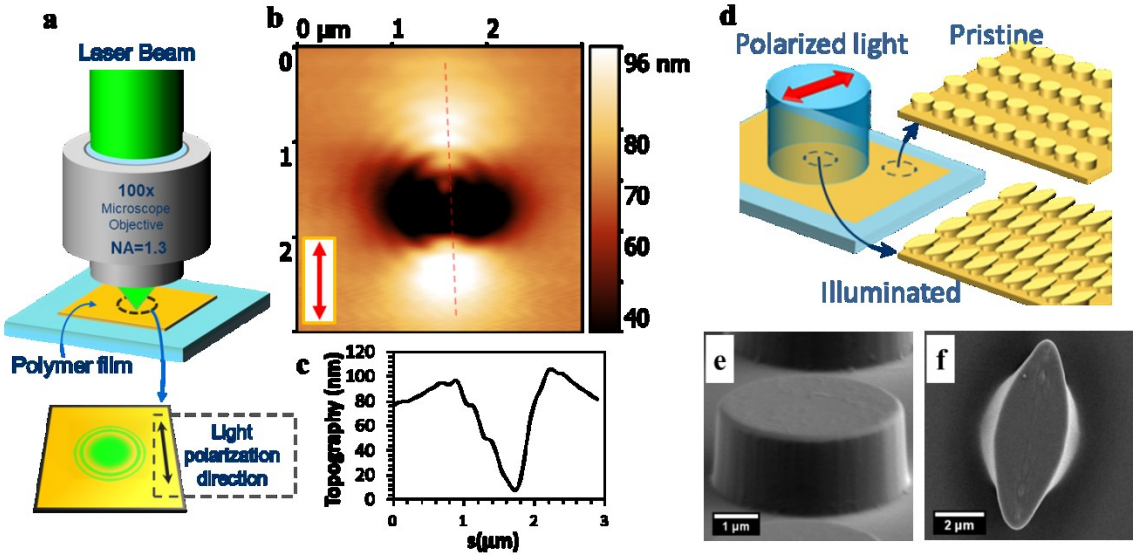

Figure 1.4| Dependence of the directional azomaterial displacement on the polarization direction of the irradiating light. (a) Schematic representation of the focused beam configuration used to inscribe the surface relief in the AFM image (b). The linear polarization direction is specified by the red arrows. (c) Topographic profile of the relief measured along the dashed red line. (d) Representation of the light-induced reconfiguration process able to turn the cylindrical micro-volume (e) of azopolymer in an asymmetric polarization dependent structure (f).

Differently from the periodic intensity distribution obtained from the interfering beams, the polymer irradiation through the focused gaussian beam has the advantage to precisely reconstruct the absolute position of the maximum intensity in the illumination spot in the successive AFM characterization. This permits the investigation of the actual direction in which the material movement during surface relief inscription.

The typical surface relief obtained onto the azopolymer film with a linearly polarized gaussian beam is presented in Figure 1.4(b). The relief is characterized by a hollow appearing in correspondence of the maximum intensity in the spot, and two lobes, raising above the non-exposed film quote, and oriented in the direction of the light polarization (indicated by the red arrow in Figure 1.4(b)). Similar observations permitted to conclude that the material movement takes place in the direction of the light polarization and proceeds from the regions at higher intensity (the center of the gaussian spot) toward darker sample regions. A similar phenomenology involves also a π-phase shift between the intensity maxima and the topographic crests of the SRG reported in Figure 1.3(b), as effectively observed by many *in-situ* analysis [39–42].

The dependence of the material displacement direction on the light polarization becomes even more evident in the experimental situations schematized in Figure 1.4(d), where a single light beam, assimilable to a plane wave with uniform intensity, is used to illuminate isolated micro-volumes of pre-patterned azopolymer surface. As will be discussed in detail in chapter 4, this simple illumination condition gives rise to a macroscopic material displacement in the direction of the light polarization, which transforms the initial symmetric micro-volume into asymmetric three-dimensional micro-structures, elongated in the light polarization direction.

1.2.3 The theoretical models for the mass migration description

While the principles of the surface relief formation described so far hold for the great majority of the azomaterials, including the amorphous azopolymers, several situations where the phenomenon behaves differently depending on the particular material architecture have been reported. For example, it was found that the interfering beams in s-s polarization configuration are able to induce appreciable surface modulations in some materials. In this case, moreover, the material accumulates in the areas at highest intensity of the illumination pattern, showing an inverted direction of the material movement respect to the p-p configuration. This inversion is observed also in the surface relief grating inscribed in certain liquid-crystalline azopolymers [4,44]. Also pure-polarization interference patterns (where the intensity is constant over the sample,

but light polarization is spatially modulated), as those generated in the interference of right- circularly (RC) and left- circularly (LF) polarized beams, have been proved to induce efficient surface relief gratings [42]. Moreover, the recent spiral-shaped surface reliefs obtained in peculiar illumination conditions [8] further complicate the overall experimental scenario, describing also a non-trivial dependence of the phenomenon on the wavefront actual profile, as well as the intensity and polarization effects.

A complete theoretical description of the light-induced mass migration phenomena should take into account of all these experimental observations in a coherent and comprehensive framework. This, however, has resulted to be a very intricate and complex task and, despite many theoretical efforts over the years that have been made in this direction, at the moment a complete understanding of the phenomenon has not been accomplished.

While the photo-isomerization of the azomolecule is thought as absolutely necessary to observe any superficial modulation, the physical link between this microscopic movement and the observed macroscopic azomaterial mass displacement has not been unambiguously recognized yet. Several different theoretical models have been proposed over the years with the aim of establishing this relation. However, none of them is able to effectively describe all the experimental observations, while their validity is typically limited to the description of the phenomenon in specific materials systems or to specific illumination conditions. The proposed models include [3]: the pressure gradient force model [15,45], the mean-field model [16], the optical field gradient force model and the anisotropic diffusion or random-walk models [18,19].

The pressure gradient model describes the azomaterial displacement in the SRG inscription experiments, in particular, as arising from the variations of the azomolecules mean occupied volume during the photo-isomerization process. The intensity gradient in the illumination pattern leads to a pressure gradient inside the material which induces a macroscopic material displacement. While the model predicts well the SRG in the case of intensity modulated interference, it is not able to describe the SRG generated with the LC-RC polarizations, as well as the light-induced reconfiguration of the isolated azopolymer micro-volumes [3,12].

The mean-field model is instead based on the dipolar attractive forces among the photo-aligned azomolecules during the light exposure. This model predicts the accumulation of the material in the bright illuminated regions, resulting valid for the description of the SRG in some liquid-crystalline azopolymers. However, it is not suitable to describe the effects of the mass migration observed in the whole class of amorphous materials, where the phenomenon is found to be more efficient.

The model based on the optical force gradient acting onto the average medium polarization induced in the azopolymer during the light illumination is able to effectively describe the polarization dependence observed in Figure 1.4 for focused optical fields, and also partially the SRG formation under the interfering beams. This model assumes a two-step mechanism, in which the photo-isomerization is thought to soften the material, enhancing its mobility in response to the illumination induced electro-magnetic forces. However, there are studies demonstrating that the forces necessary for the material movement predicted by this model are too high respect to the actual strength of the electromagnetic interactions in the material [31].

In the models based on the anisotropic diffusion of the azomolecules, the directional material motions is described as resulting from an inchworm-like or a random-walk translation of the azounits along the light polarization direction. These models are able to predict many of the observed mass-migration phenomena in low exposure intensity regimes, but they do not take into account the hole-burning effects due to the reorientation of the azomolecules under irradiation with linearly polarized light and also the saturation of the mass transport observed for long or intense irradiations.

All the mentioned models share a common feature: they require the presence of an optical gradient in the intensity and/or polarization of the illuminating light. These illumination conditions are met in typical experiments where the illumination pattern is kept relatively simple (as in the case of the interfering beams or the focused gaussian beams). In the next paragraph is given a description of the optical gradient force model, taken as exemplifying theoretical framework highlighting the proper description of the surface reliefs arising is simple illumination conditions enabled by the models mentioned above.

However, all the cited models fail in the description of the light-driven spiral-shaped surface reliefs observed under the irradiation of the azopolymer film with a focused light beam having an optical vortex along its propagation axis (for example a Laguerre-Gauss beam). These peculiar surface reliefs have led to the formulation of a new phenomenological microscopic model [46], based on the anisotropic diffusion hypothesis of the azomolecules, which assumes also an enhanced material mobility at the film free-surface respect to the bulk polymer. Beside the spiral-shaped surface reliefs, which will be introduced in the end of the next paragraph, this model has resulted suitable also to predict the phenomenology of the micro-volume reconfiguration [10] (see chapter 4), and other peculiar surface reliefs we have obtained in other non-trivial illumination conditions (see chapter 2).

1.3 The optical gradient force model

The optical gradient force model ascribes the photo-driven mass migration of the azopolymers to the microscopic forces that the optical field induces onto the polarizable material during the exposure. This model is able to describe the polarization dependence of the directional light-induced mass migration observed in many standard illumination conditions, even if it does not take into account the actual photo-isomerization kinetics of the azomolecules. Indeed, the material is typically described as a dielectric medium, responding to the optical electric field $\boldsymbol{E}(\boldsymbol{r},t)$ through a linear medium polarization vector (Figure 1.5(a)

$$\boldsymbol{P}(\boldsymbol{r},t)=\varepsilon_0\chi\boldsymbol{E}(\boldsymbol{r},t), \tag{1.1}$$

where ε_0 is the permittivity of the vacuum and χ is the medium susceptibility. The photo-isomerization at the molecular level in this model is thought to be responsible of photo-induced plasticization of the material, which becomes free to respond to the action of the optical induced forces.

In order to illustrate the main aspects of the optical gradient force models, here is presented its original version [17,47,48], oversimplified in both the description of the optical forces acting on the material, and on the description of the material movement resulting from these forces. However it successfully predicts, at least qualitatively, the SRGs and the focused SR under standard illumination conditions. The complete version of the model, reported in reference [49], on the contrary takes into account the full description of the different aspects of the phenomenon (for example the use of actual solutions of Navier-Stokes equations for the material movement description), leading to a very intricate and complex mathematical framework. Some of the predictions of this complete model are discussed in section 3.3.4 of this thesis for the interpretation of some our experimental results reported in that section.

In the simplified model, the time-averaged force acting onto the azochromophores is a small volume is given by[1]

$$\boldsymbol{f}(\boldsymbol{r})=-\left\langle\left[\nabla\cdot\boldsymbol{P}(\boldsymbol{r},t)\right]\boldsymbol{E}(\boldsymbol{r},t)\right\rangle=-\left\langle\left[\varepsilon_0\chi\nabla\cdot\boldsymbol{E}(\boldsymbol{r},t)\right]\boldsymbol{E}(\boldsymbol{r},t)\right\rangle, \tag{1.2}$$

where ⟨ ⟩ indicates the average across the irradiance time. Equation (1.2) states that the material experiences a force only in directions where both the electric field and its

[1] The total force should include also a magnetic term [49]: $\boldsymbol{f}=-(\boldsymbol{\nabla}\cdot\boldsymbol{P})\boldsymbol{E}+\frac{\partial\boldsymbol{P}}{dt}\times\boldsymbol{B}$.

gradient are not vanishing, while the force is zero when the polarization is orthogonal to the optical field gradient.

Let us now to specify the situation, described in Figure 1.5(b), to the case of the surface modulation produced by a focused 2D gaussian beam. The polymer surface extends in x-y plane, while the x-polarized Gaussian beam propagates along the z axis and irradiates normally the surface. Using the expression of a gaussian optical field

$$E(x,y,z) = E_0 \exp\left[-\frac{\left(x^2+y^2\right)}{\omega^2}\right]\exp\left(-\frac{\alpha z}{2}\right), \tag{1.3}$$

equation (1.2) is written as:

$$\begin{aligned} \boldsymbol{f}(x,y,z) &= -\left(\frac{\varepsilon_0 \chi'}{\omega^2}\right)\exp(-\alpha z) I_0\, x \exp\left[-2\frac{\left(x^2+y^2\right)}{\omega^2}\right]\hat{\boldsymbol{x}} = \\ &= \frac{1}{4}\varepsilon_0 \chi' \exp(-\alpha z)\frac{\partial I(x,y)}{\partial x}\hat{\boldsymbol{x}}, \end{aligned} \tag{1.4}$$

where α is the absorption coefficient of the material, $I_0 = E_0^2$ and $I(x,y)$ is the intensity distribution in the x-y plane and χ' is the real part of the material susceptibility. The growth of the surface relief is attributed to the lateral displacement of a thin layer of polymer that is made photo-fluidized by the repeated trans-cis-trans photo-isomerization of the azomolecules. The flow of this mobile layer is described as a surface velocity field $\boldsymbol{v}_s(x,y,z)$, proportional (through a factor μ) to the optical force $\boldsymbol{f}(x,y,z)$:

$$\boldsymbol{v}_s(x,y,z) = \mu\, \boldsymbol{f}(x,y,z). \tag{1.5}$$

The factor μ takes into account the viscous drag generated between the mobile surface material and the bulk material, and it is assumed to be independent on the illumination strength (weak irradiance regime). Assuming the incompressibility of the polymer, the surface deformation velocity v_z is derived from the continuity equation $\nabla \cdot \boldsymbol{v} - \partial\rho/dt = 0$ and gives:

$$\nabla \cdot \boldsymbol{v}(x,y,z) = 0, \tag{1.6}$$

which leads to:

$$\frac{\partial v_z}{\partial z} = -\left(\frac{\partial v_x}{\partial x} + \frac{\partial v_y}{\partial y}\right) = -\nabla \cdot \boldsymbol{v}_s. \tag{1.7}$$

Integrating equation (1.7) along polymer total thickness d yields:

$$v_z(x,y,d) - v_z(x,y,0) = v_z(x,y,0) = -\int_0^d (\nabla_s \cdot \boldsymbol{v}_s)\, dz$$
$$-\mu \int_0^d (\nabla_s \cdot \boldsymbol{f})\, dz = -\mu h \left[\nabla_s \cdot \boldsymbol{f}\right]_{z=0} \tag{1.8}$$

where ∇_s refers to the derivation only respect to the lateral coordinates, h is the thickness of the effective mobile polymer layer and the boundary condition $v_z(x,y,d) = 0$ has been used.

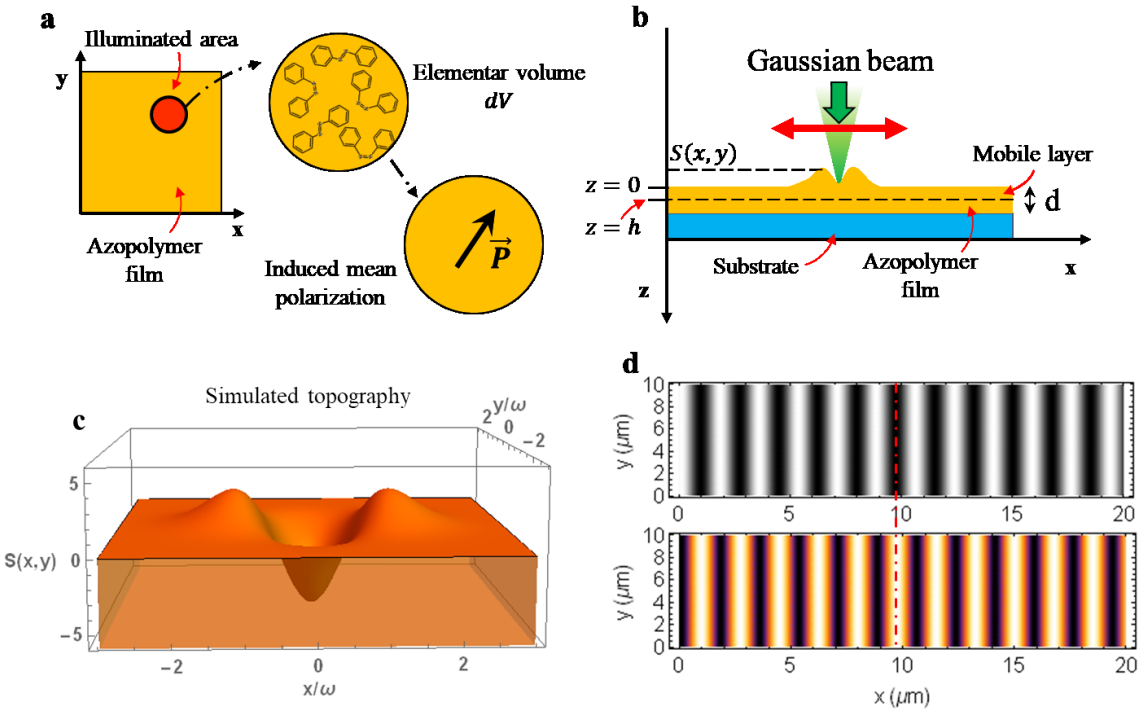

Figure 1.5| The optical gradient force model for the light-induced mass migration. (a) Hypothesis of the average material polarization induced in the illuminated azomaterial. (b) Schematic representation of the geometrical configuration describing the system. (c) Simulated superficial topography obtained from the azopolymer illumination with a linearly polarized gaussian beam. (d) Simulated sinusoidal intensity profile of two interfering beams (top) and simulated surface relief grating predicted by the model. The red dashed line indicates the phase relation between the maxim in the intensity pattern and the crests in the simulated SRG.

Using expression (1.4) for the driving force in the actual situation of linearly polarized beam along the x-direction in the relation (1.8), we obtain the explicit

expression for $v_z(x,y,0)$, which can be used to calculate the surface displacement $S(x,y,t)$ by integrating over the exposure time t:

$$\begin{aligned} S(x,y,t) &= \int_0^t v_z(x,y,0)\,dt' \\ &= \frac{1}{4} h\mu\varepsilon_0\chi' \frac{\partial^2 I(x,y)}{\partial^2 x} t. \end{aligned} \tag{1.9}$$

The relation (1.9), valid in the limit of weak irradiance power, states that the surface relief arising onto the polymer film is proportional to the second derivative of the intensity pattern. Furthermore, the sign of χ' determines the direction of the material displacement along the z axis. Using the assumption $\chi' < 0$, a good qualitative agreement of the predicted surface relief (Figure 1.5(c)) with the surface relief experimentally observed in this situation (reported in Figure 1.4(b)) is found.
The same calculations made for the gaussian beam can be performed easily also for the optical filed resulting from two p-p polarized beams. The simulated images reporting the sinusoidal intensity pattern and the predicted SRG by the relation (1.9) are presented in Figure 1.5(d), showing the correct predictions of the model also in this illumination configuration. However, as we will see in the next section, this model is inadequate to describe the surface relief appearing onto the azopolymer surface, when a focused Laguerre-Gauss beam, having a helical wavefront and an optical-vortex at its axis, is used to illuminate the azomaterial in a condition similar to the one presented in Figure 1.4.

1.4 The spiral surface reliefs

The beams endowed by an optical vortex at their axis [50] are light beams characterized by a dependence $\exp[iq\varphi]$ of the optical phase on the azimuthal angle φ in the planes transversal to the optical propagation axis. This phase dependence confers a helical shape to the wavefront of these beams (Figure 1.6(a)), which accumulate a phase shift of a quantity $2\pi q$ by circling once the beam axis. The integer number, positive or negative, q is called *vortex topological charge*, and defines the handedness of the beam helical wavefront. The azimuthal dependence of the phase evolution around the propagation axis implies a phase singularity point on this axis in each transversal plane, where the undefined phase results in a doughnut-like intensity profile (Figure 1.6(a)). Typical examples of such class of beams are the Laguerre-Gauss beams [51,52], which, because of their helical-shaped wavefront (Figure 1.6(a)) are known to carry also

orbital-angular momentum [53,54]. More detailed description of these beams and how they can be generated is presented in the next chapter.

The use of a Laguerre-Gauss beam for the illumination of an azopolymer film (Figure 1.6(b)) produces unexpected spiral-shaped surface relief topographies [8] (Figure 1.6c). Assuming a dependence of the mass migration phenomenon only on the intensity gradient and polarization, as described for example by the optical gradient force model, no information about the helicity of the beam wavefront should be visible in the surface reliefs because no information of such phase dependence is contained in the doughnut-shaped intensity profile of a Laguerre-Gauss beam.

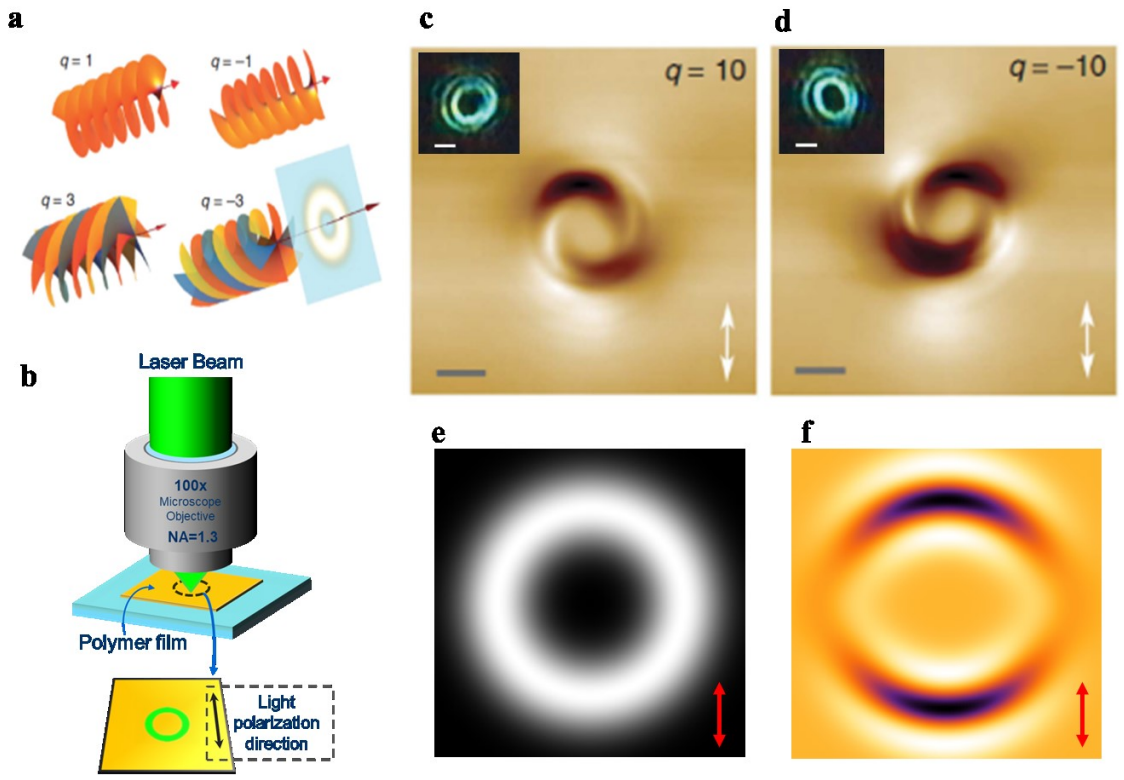

Figure 1.6| Inadequacy of the optical force gradient model in describing the surface reliefs obtained from the illumination of the azopolymer with a vortex beam. (a) Schematic representation of the helical wavefront and the doughnut-shaped intensity profile of a vortex beam. (b) Representation of the illumination condition for the surface relief inscription. Actual AFM topography of the surface relief obtained from the irradiation with a beam having q=10 (c), and q=-10 (d), in the same polarization conditions of the simulated images. The inset in the panels (c) and (d) shows the intensity pattern of the irradiating beam on the azopolymer sample. Images reproduced from reference [8]. The scale bars in panels (e-f) corresponds to 1 μm. (e) Simplified simulated intensity profile. (f) Surface topography predicted by the optical force gradient model with linearly polarized beam in the direction of the red arrow.

In this illumination configuration, indeed, the optical gradient force model predicts only a spatially dependent efficiency of the surface modulation. This can be observed from the surface relief reported in Figure 1.6(f) simulated through the optical gradient force model for a doughnut-shaped beam, linearly polarized along the vertical direction of the image (Figure 1.6(e)). The simulated surface reliefs show the expected efficient mass migration along the doughnut diameter in the vertical direction and zero surface modulation along the doughnut diameter in the x direction (being the intensity gradient in this direction orthogonal to the polarization direction), while no traces of any spiral structures appear.

In reference [8] has been found a direct dependence of the experimental spiral surface reliefs lateral shape on the absolute value and relative sign of the beam topological charge q. In particular, larger values of $|q|$ translate into larger spiral diameters, while the inversion in the topological charge sign produces an inversion of the handedness of the spiral arms inscribed onto the polymer. This peculiar behavior can be immediately observed by the comparison of the surface reliefs reported in Figure 1.6(c) and Figure 1.6(d), obtained in the same irradiation conditions but with beams having opposed topological charge signs [8].

As, the wavefront handedness, and not the intensity distribution (inset Figure 1.6(c-d)), is the only beam quantity explicitly sensitive to the topological charge q, the natural hypothesis for the interpretation of the observed spiral mass transport is that this originates from an unprecedented sensitivity of the light-induced mass migration phenomenon to the wavefront of the illuminating optical field. As we will see in the next chapter, the *photo-induced anisotropic diffusion* model proposed by A. Ambrosio et al. in references [8,46] is able to take into account this peculiar response of the azomaterial to the illuminating optical field, attributing the observed wavefront sensitivity to a surface-initiated interference between the components of the higly focused optical field in the azopolymer plane.

2 The photo-induced anisotropic molecular diffusion model

The peculiar spiral surface reliefs arising under the illumination of an azomaterial with beams having an optical vortex at their axis has brought to light, in the already rich scenario of the light-induced mass migration phenomenon, another ingredient in the complex dependence of the photo-driven material movement on the configuration of the irradiating light: the apparent sensitivity to the spatial wavefront structure of the illuminating beam. The first tentative to rationalize this observation was made through the formulation of a symmetry-based phenomenological model, which included an enhanced effect in the photo-induced material migration at the surface. Even if qualitatively, this model is able to fully explain all the observed findings in the spiral surface relief [8]. This phenomenological model could be in principle compatible with different molecular mechanisms able to relate the azobenzene photo-isomerization dynamics to the spiral mass transport observed in the azopolymer. However, a solid physical picture of the microscopic underlying phenomenon can be given by a molecular model based on the anisotropic diffusion of the photo-isomerizing azochromophores under irradiation. This model includes, in a coherent way, both the new wavefront sensitivity and the well-known intensity/polarization dependences, typically observed in the formation of the surface reliefs with standard illumination conditions. Furthermore, its predictions can permit the use of the light-induced surface reliefs as a topographic recording of the actual distribution of complex optical field patterns. After the detailed description of the model, in this chapter two of this experimental situations are presented, in which surface reliefs are inscribed onto the azopolymer surface with the irradiation of light beams obtained from two light-modulating devices: a meta-surface acting as a spin-to-orbital angular momentum converter, and the liquid-crystal *θ-cell*, demonstrated to generate (modified) radially and azimuthally polarized beams [55]. The agreement between the experimental and the predicted surface modulations allows the test of the hypothesized optical field

distributions of the beams and represents an indirect characterization of the light-modulating devices. Furthermore, the model presented here has also the ability to correctly describe the light-induced reconfiguration of isolated azopolymer micro-structures under uniform beam irradiation, as we will see in chapter 4.

2.1 The molecular anisotropic diffusion model

As already mentioned, the model uses the concept of the anisotropic diffusion of the azochromophores as the molecular driving mechanism of the macroscopic mass migration occurring in azomaterials under illumination. Respect to other models, based on the same microscopic driving mechanism [18,19,56], this model takes into account the possibility of a different efficiency for the diffusion of the azomolecules situated in the proximity of the free azopolymer surface respect to the diffusion occurring in the bulk film. The enhanced mobility at the surface produces a light-driven material transport which interlaces the optical field components in non-trivial way under particular illumination configurations, while it results negligible in most of the reported standard experimental illumination conditions (for example in the inscription of SRG). As we will see, this term is essential in order to explain the spiral mass transport observed in the surface reliefs induced by focused vortex-beams.

As discussed below, the model is oversimplified in several aspects, and a quantitative discrepancy between the predictions and the observation is found as consequence of the adopted approximations. However, it catches the fundamental qualitative aspects of all the reported experiments related to the mass migration in amorphous azomaterials, resulting as a worthy candidate for eventual further theoretical insight.

Let us to consider an azopolymer film of initial thickness L deposited onto a rigid substrate (Figure 2.1(a)). The coordinate reference system is chosen such that the film extends in the x-y plane, with the polymer-substrate interface situated at the $z = 0$ and the polymer free surface at the quote $z = L$. After the light irradiation, the free surface of the polymer manifests the appearance of the surface reliefs, which can be described as position-dependent height variations $\Delta h(x, y) = z(x, y) - L$ of the free-surface quote respect to the height of the unexposed film L.

In the model, the surface modulations appearing under irradiation are assumed to be caused by a light-induced polymer mass transport in the x-y plane, which can be described by a mass-current density vector **J**. Assuming the incompressibility of the

material, the in-plane light-induced mass displacement leads to a surface modulation which can be described by the relation [7,44]:

$$\Delta h(x,y) = -\frac{L\Delta t}{\rho}\partial_k \bar{J}_k, \quad \text{with } k = x,y \tag{2.1}$$

where Δt is the irradiation time, ρ is the polymer mass density, ∂_k denotes the derivative respect to the transverse coordinates x-y and $\bar{\boldsymbol{J}} = (\int_0^L \boldsymbol{J}\, dz)/L$ is the averaged mass current across the film thickness L. In relation(2.1), as in the rest of the paragraph, the sum over repeated indices is intended. From this equation we can see that, in order to determine the surface relief pattern over the surface, we need to know the derivatives $\partial_x J_x$ and $\partial_y J_y$ of the current in the x-y plane.

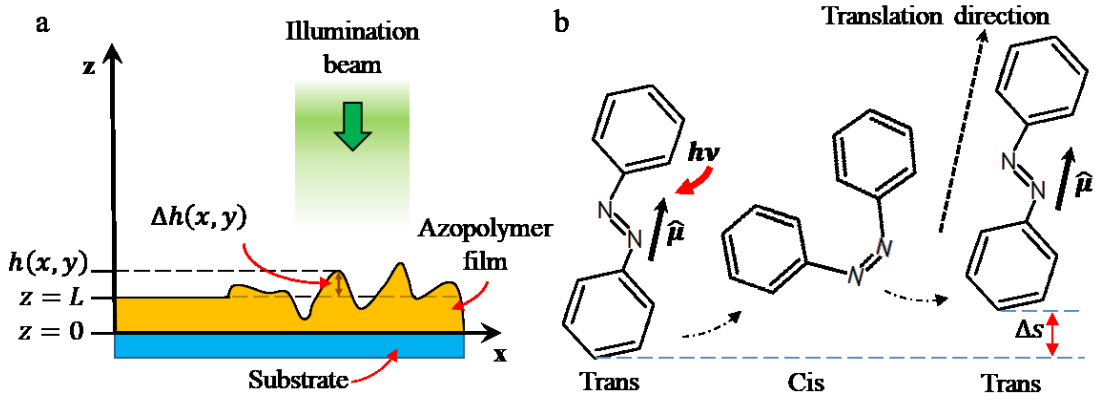

Figure 2.1| Photoinduced anisotropic diffusion model. (a) Definition of the geometrical parameters. (b) Schematic representation of the anisotropic diffusion of the azomolecule as a result of the absorption of a light photon. The molecule translates along of the direction of the molecular dipole moment $\hat{\boldsymbol{\mu}}$.

In order to relate the mass density current to the microscopic dynamics induced by the illuminating optical field, let us to describe the azomolecules embedded in the polymer matrix by their position vector $\mathbf{r}$ and by the unit vector $\hat{\boldsymbol{\mu}}$, defining the orientation of the molecular main axis which also coincides with the molecular transition dipole direction Figure 2.1(b).

Assuming a dipole electric interaction, the absorption probability $p(\boldsymbol{r}, \hat{\boldsymbol{\mu}})$ for the azomolecules to absorb a photon of the irradiating light field is:

$$p(\boldsymbol{r}, \hat{\boldsymbol{\mu}}) = \alpha \left| \hat{\boldsymbol{\mu}} \cdot \mathbf{E}(\mathbf{r}) \right|^2, \tag{2.2}$$

where **E**(**r**) is the complex optical electric field vector and α is a constant proportional to the absorption coefficient at the considered illumination wavelength. As the molecules absorbing a photon are subject to the photo-isomerization process, the probability $p(\boldsymbol{r}, \hat{\boldsymbol{\mu}})$ described by the relation (2.2) determines the number density of the excited molecules per unit volume and solid angle $n_e(\boldsymbol{r}, \hat{\boldsymbol{\mu}})$ contributing to the molecular diffusion process. In order to define such number density, let us denote with $n(\boldsymbol{r}, \hat{\boldsymbol{\mu}})$ the total number density (both excited and non-excited) of the azomolecules per unit volume and solid angle.

At equilibrium, before the illumination starts, the position and the orientation of the molecules can be considered as approximately uncorrelated, and hence we can write:

$$n(\mathbf{r}, \hat{\boldsymbol{\mu}}) = N(\mathbf{r}) f(\hat{\boldsymbol{\mu}}), \tag{2.3}$$

where N(**r**) is the molecule number density per unit volume irrespective to the orientation, and $f(\hat{\boldsymbol{\mu}})$ is the initial orientational distribution of the azomolecules. Assuming a uniform distribution of the azomolecules across the film sample, N(**r**) can be simply written as:

$$N(\mathbf{r}) = N_0\, \theta(z)\theta(L-z), \tag{2.4}$$

where N_0 is the uniform bulk number density, and $\theta(z)$ is the Heaviside step function ($\theta(z) = 0$ for $z < 0$ and $\theta(z) = 1$ for $z > 0$), introduced to describe the polymer surfaces located at $z = 0$ and $z = L$. The initial orientational equilibrium distribution is assumed to be isotropic, so that we have:

$$f(\hat{\boldsymbol{\mu}}) = \frac{1}{4\pi}. \tag{2.5}$$

Writing explicitly these factors in the relation (2.4), we have:

$$n(\mathbf{r}, \hat{\boldsymbol{\mu}}) = \frac{N_0}{4\pi}\theta(z)\theta(L-z). \tag{2.6}$$

Under illumination, the initial molecular distribution described by (2.6) is certainly altered by the molecular photo-isomerization processes which tend to reorient the molecules orthogonal to the electric field (the orientational hole-burning effect described in section 1.1). Moreover, the molecules also translate as a result of the mass migration phenomenon, so that also their spatial distribution can be altered during the irradiation. However, if the fraction of excited molecules is assumed to be small, these

molecular rearranged configurations can be neglected and we may retain the equilibrium distribution described by the relation (2.6) also during the light exposure. As we will see below, this approximation is equivalent to assume a first order interaction (linearized in the field intensity) and makes the model valid only for weak and/or short irradiations.

To go further toward the approximated form of $n_e(\boldsymbol{r},\hat{\boldsymbol{\mu}})$, we assume also that at each excitation event a molecule moves only a short distance respect to the characteristic length of the optical gradients and changes orientation only slightly. In these approximations, we can write the following rate equation for the number density of excited molecules for a given location and orientation:

$$\frac{dn_e}{dt} = p\left(n - n_e\right) - \frac{n_e}{\tau_e}, \tag{2.7}$$

where $(n - n_e)$ is the number of non-excited molecules for the same position and orientation and τ_e is the excited-state lifetime. In the first order approximation, we can neglect n_e respect to n in (2.7) and, at the steady state ($dn_e/dt = 0$), we find for the number-density of excited molecules per unit volume and solid angle the expression:

$$n_e\left(\boldsymbol{r},\hat{\boldsymbol{\mu}}\right) = p\left(\boldsymbol{r},\hat{\boldsymbol{\mu}}\right)\tau_e\, n\left(\boldsymbol{r},\hat{\boldsymbol{\mu}}\right). \tag{2.8}$$

From equation (2.8) it is evident that any non-equilibrium term in n (depending explicitly on the molecule-field interaction) would produce, after the multiplication with the factors contained in p (equation (2.2), higher-order powers in the fields, which are neglected in this simplified description of the light-driven molecular dynamics. Substituting relations (2.2) and (2.6) in (2.8), we finally obtain:

$$n_e\left(\boldsymbol{r},\hat{\boldsymbol{\mu}}\right) = \frac{\alpha\tau_e N_0}{4\pi}\left|\hat{\boldsymbol{\mu}}\cdot\mathbf{E}\left(\mathbf{r}\right)\right|^2 \theta\left(z\right)\theta\left(L - z\right), \tag{2.9}$$

which defines the number of azomolecules per unit volume and solid angle contributing to the light-driven directional diffusion. In order to calculate the anisotropic diffusion, let us specify the other role that the molecular transition dipole moment $\hat{\boldsymbol{\mu}}$ plays in the model.

Accordingly to other diffusion models [18,19,56], the direction of the unit vector $\hat{\boldsymbol{\mu}}$ defines also the direction of the net molecular displacement arising from the light-triggered random-walk diffusion performed by the excited azomolecules. In this framework, the anisotropic molecular diffusion can be visualized as equivalent to a wormlike motion the azocromophore performs under irradiation (Figure 2.1(b)). The

one-dimensional mass current resulting from this anisotropic diffusion process can be expressed as:

$$J\left(\mathbf{r},\hat{\boldsymbol{\mu}}\right)=-D\left(z\right)\frac{dn_e}{dx_\mu}=-D\left(z\right)\hat{\boldsymbol{\mu}}\cdot\nabla n_e\left(\mathbf{r},\hat{\boldsymbol{\mu}}\right), \tag{2.10}$$

where $D(z)$ is the excited-molecule diffusion constant, whose ideal z dependence is assumed to be:

$$\begin{aligned} &D\left(0\right)=0 \\ &D\left(z\right)=D_B \quad \text{for} \quad 0<z<L \\ &D\left(L\right)=D_S \end{aligned} \tag{2.11}$$

In the relations (2.11), an explicit possible change in the diffusion constant is considered in correspondence of the free polymer surface (D_S) respect to its value in the bulk polymer (D_B). Because of the fact that the described diffusion cannot push the molecule out from the polymer film, there exists a force at the surface counteracting the every pressure force component originated by the z component of the current vector **J**. Without the need of the explicit form of such term, we can simply include this consideration by imposing a net resulting vanishing current along z axis at the free polymer surface $\boldsymbol{J}_z(L)=0$.

Inserting equations (2.9) and (2.11) into (2.10), we obtain the following expression for the mass current:

$$\boldsymbol{J}\left(\mathbf{r},\hat{\boldsymbol{\mu}}\right)=-\frac{\alpha\tau_e N_0}{4\pi}D\left(z\right)\left\{\begin{aligned}&\theta\left(z\right)\theta\left(L-z\right)\,\hat{\boldsymbol{\mu}}\cdot\nabla\left[\left|\hat{\boldsymbol{\mu}}\cdot\mathbf{E}\left(\mathbf{r}\right)\right|^2\right]\\&+\left[\delta\left(z-L\right)\left(\hat{\boldsymbol{\mu}}\cdot\hat{\mathbf{z}}\right)\left|\hat{\boldsymbol{\mu}}\cdot\mathbf{E}\left(\mathbf{r}\right)\right|^2\right]\end{aligned}\right\}, \tag{2.12}$$

where we have introduced the unit vector $\hat{\boldsymbol{z}}$ normal to the surface and the Dirac's delta function $\delta(z)$. The total current vector $\boldsymbol{J}$ is finally obtained by integrating equation (2.12) over the entire solid angle:

$$\begin{aligned}\boldsymbol{J}\left(\mathbf{r}\right)=\;&\int J\left(\hat{\boldsymbol{\mu}}\right)\hat{\boldsymbol{\mu}}\,d\Omega \\ &=-\frac{\alpha\tau_e N_0}{4\pi}D_B\,\theta\left(z\right)\theta\left(L-z\right)\int\hat{\boldsymbol{\mu}}\,\hat{\boldsymbol{\mu}}\cdot\nabla\left[\left|\hat{\boldsymbol{\mu}}\cdot\mathbf{E}\left(\mathbf{r}\right)\right|^2\right]d\Omega \\ &+\frac{\alpha\tau_e N_0}{4\pi}D_S\,\delta\left(z-L\right)\int\hat{\boldsymbol{\mu}}\,\hat{\boldsymbol{\mu}}\cdot\nabla\left[\left|\hat{\boldsymbol{\mu}}\cdot\mathbf{E}\left(\mathbf{r}\right)\right|^2\right]d\Omega\end{aligned} \tag{2.13}$$

The average of this current along z across the film thickness, while assuming z-independent optical fields, leads to the following expressions for the lateral mass current:

$$\bar{J}_k = \alpha\tau_e N_0\left(-D_B M_{klij}\partial_l\left(E_i^* E_j\right)+\frac{D_S}{L}M_{kzij}E_i^* E_j\right), \tag{2.14}$$

where $k,l=x,y$; $i,j=x,y,z$, and the result of the angular integrals is written as [46]:

$$M_{klij}=\frac{1}{4\pi}\int \hat{u}_k\hat{u}_l\hat{u}_i\hat{u}_j\,d\Omega=\frac{1}{15}\left(\delta_{kl}\delta_{ij}+\delta_{ki}\delta_{lj}+\delta_{kj}\delta_{li}\right), \tag{2.15}$$

δ_{ij} being the Kronecker symbol. Inserting equation (2.15) into equation (2.14), we finally obtain the explicit form of the transverse mass current as:

$$\begin{aligned}\bar{J}_k = {} & C_1\partial_k\left(E_l^* E_l\right)+C_2\partial_l\left(E_l^* E_k+E_k^* E_l\right)+C_3\partial_k\left|E_z\right|^2+\\ & +\frac{C_s}{L}\left(E_z^* E_k+E_z E_k^*\right),\end{aligned} \tag{2.16}$$

with $k,l=x,y$, and

$$\begin{aligned}C_1=C_2=C_3=-\frac{\alpha\tau_e N_0 D_B}{15}\\ C_S=\frac{\alpha\tau_e N_0 D_S}{15}.\end{aligned} \tag{2.17}$$

A close look at the form of the different terms appearing in the mass current relation (2.16) allows the attribution of the effects each of them produce respect to the overall material displacement in the x-y plane during the illumination process.

The term proportional to C_1 corresponds to a mass migration occurring along the gradient of the total transverse intensity. Indeed, such term is proportional to $\left(E_x^2+E_y^2\right)$, which drives the polymer out (in) of the bright regions once $C_1>0$ ($C_1<0$) is assumed. This is the only non-vanishing term in the mass current that can be responsible of the appearance of surface reliefs in the case of s-polarization.

The term in C_3 is proportional to the longitudinal field $|E_z|^2$. This is typically small in many illumination cases, but it can be not negligible in some illumination configurations (for example with highly focused beams).

The term in C_2 is the term causing the polarization-sensitive mass transport discussed in the section 1.2. This term leads to a polymer motion along the direction of

the electric field, and it is the relevant term in many standard illumination configurations (including the interference of p-p polarized beams, or the linearly polarized focused gaussian beams).

The last term, proportional to the surface diffusion constant C_S, is instead sensible to the light wavefront via the interference of the longitudinal and the transverse field components. In most of the standard illumination conditions this surface-mediated interference term vanishes identically. However, this term has been demonstrated to describe the spiral transport effect [8,46], meaning that it can be significant is some illumination conditions, as in the case of the focused vortex beams.

Using equation (2.1), the total lateral current $\bar{J}_k$ defined by the relation (2.16), gives the explicit dependence of the surface modulation on the components of the irradiating optical field:

$$\begin{aligned}\Delta h(x,y) = {} & c_1\partial_k\partial_k\left(E_l^* E_l\right) + c_2\partial_k\partial_l\left(E_l^* E_k\right) + c_3\partial_k\partial_k\left|E_z\right|^2 + \\ & + 2c_s\partial_k \operatorname{Re}\left(E_z^* E_k\right)\end{aligned}, \tag{2.18}$$

where

$$\begin{aligned} c_1 &= c_3 = -\frac{L\Delta t\, C_1}{\rho} = \frac{L\Delta t\,\alpha\tau_e N_0 D_B}{15\rho}, \\ c_2 &= 2c_1, \\ c_S &= -\frac{\Delta t\, C_s}{\rho} = -\frac{\Delta t\,\alpha\tau_e N_0 D_S}{15\rho}. \end{aligned} \tag{2.19}$$

Making the sum over the indices, equation (2.18) can be written in the explicit form, where the field components are expressed in Cartesian coordinates:

$$\begin{aligned}\Delta h(x,y) = {} & (c_1 + c_2)\left[\partial_x^2\left|E_x\right|^2 + \partial_y^2\left|E_y\right|^2\right] + \\ & + c_1\left(\partial_x^2\left|E_y\right|^2 + \partial_y^2\left|E_x\right|^2\right) + \\ & + 2c_2\partial_x\partial_y \operatorname{Re}\left(E_y^* E_x\right) + \\ & + c_3\left(\partial_x^2\left|E_z\right|^2 + \partial_y^2\left|E_z\right|^2\right) + \\ & + 2c_S\left[\partial_x \operatorname{Re}\left(E_z^* E_x\right) + \partial_y \operatorname{Re}\left(E_z^* E_y\right)\right].\end{aligned} \tag{2.20}$$

Relation (2.20) can be used to directly calculate the surface reliefs arising onto the azopolymer surface under irradiation with an optical field $\boldsymbol{E}(\boldsymbol{r}) = \left(E_x, E_y, E_z\right)(\boldsymbol{r})$.

2.1.1 Phenomenological choice of the mass current coefficients

The anisotropic molecular diffusion model presented here would allow to directly link the molecular diffusion parameters and the observed macroscopic mass movement. Indeed, the coefficients appearing in the constitutive relations (2.19) can be explicitly evaluated on the basis of the material properties. However, the use of reasonable values for the molecular parameters in (2.19) leads to an estimation of the multiplicative coefficients appearing in equation (2.20) not able to fit quantitatively the experimental results in simple illumination conditions [8,46]. Such discrepancy can be attributed to the drastic approximations made on the dynamics of the molecules under the light-driven photo-isomerization. For example, the orientational hole-burning effect is completely omitted, as well as any consequent saturation of the mass migration process. Furthermore, the influence of the viscoelastic forces inside the material is oversimplified by the simple incompressibility assumption. All these simplification should be relaxed step-by-step in a more sophisticated model in order to achieve more accurate quantitative predictions.

However, the real power of the model, even in this simplified form, emerges if the relation (2.20) is understood as the result of a phenomenological model, and the multiplicative coefficients appearing there are intended to be chosen empirically in order to match the experimental results. The discussion conducted in the previous paragraph about to the meaning of the different terms of the light-induced mass current in the relation (2.16), and the behavior of the mass material phenomenon in well-known situations (as the SRG inscription and the surface reliefs under focused gaussian beams) can help in this empirical choice of the parameters.

For example, the prediction $C_1 = C_2 = C_3$ in equation (2.17), leads to the relation $c_2 = 2c_1 = 2c_3$. Considering the case of the illumination with the pattern generated with two interfering beams in p-p or s-s configurations, equation (2.20) would predict an amplitude of the surface reliefs proportional to the term $(c_1 + c_2)$ in the case of p-p polarization, while the amplitude of s-s polarization is proportional to c_1. This would imply that, using the same exposure time in this two illumination configurations, the predicted amplitude ratio in the inscribed SRG is $c_1/(c_1 + c_2) = 1/3$, which is in disagreement with the most of the experiments reporting a very low efficient surface modulation in the case of s-s polarization (see also Figure 1.3).

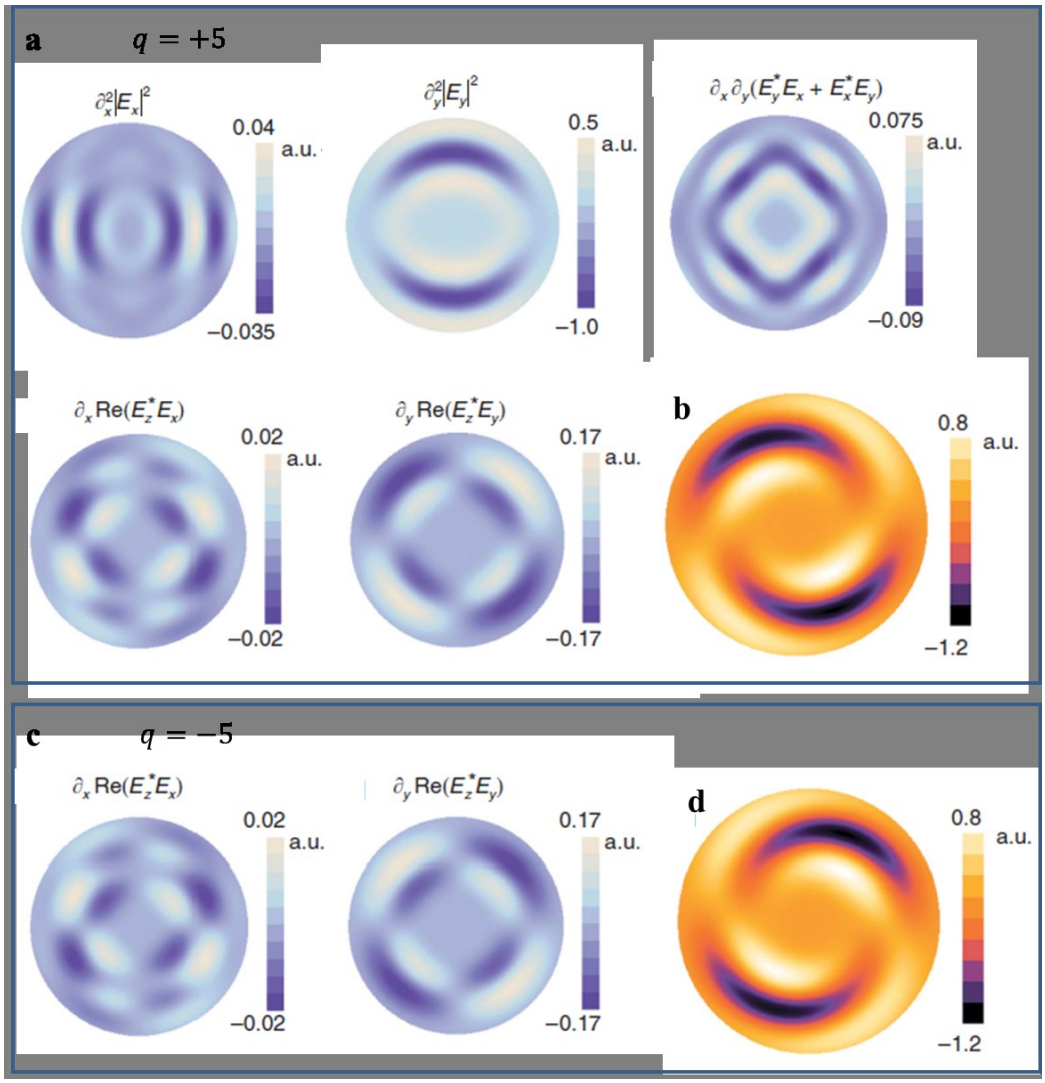

Figure 2.2| Spiral surface reliefs simulated by the phenomenological model. (a) Simulated terms appearing in equation (2.21) for a Laguerre-Gauss beam having a topological charge $q = +5$. (b) Total surface reliefs resulting from the coefficient choice $c_2 = 1$, $c_S = 8(c_2/\lambda)$. (c) and (d) same simulation made for $q = -5$. Only the terms including the interference between the longitudinal and transverse optical field component are changed by the opposite sign of the topological charge. The simulations are reproduced from reference [8].

From these considerations, a reasonable choice for the coefficient c_1 is $c_1 \ll c_2$, while relation (2.19) suggest also $c_3 \ll c_2$. In the limiting case, one can even choose $c_1 = c_3 = 0$. With this hypothesis, equation (2.20) can be rewritten as:

$$\begin{aligned}\Delta h(x,y) \approx\ & c_2\left[\partial_x^2\left|E_x\right|^2+\partial_y^2\left|E_y\right|^2\right]+\\ & +2c_2\partial_x\partial_y\,\mathrm{Re}\left(E_y^*E_x\right)+\\ & +2c_S\left[\partial_x\,\mathrm{Re}\left(E_z^*E_x\right)+\partial_y\,\mathrm{Re}\left(E_z^*E_y\right)\right].\end{aligned} \tag{2.21}$$

Now, the relative strength of the superficial coefficient c_S respect to the coefficient c_2 can be phenomenologically adjusted to correctly explain the spiral surface reliefs arising under the vortex beam irradiation. In Figure 2.2(a) are presented the simulated contributions (reproduced from reference [8]) of the optical field derivatives appearing in the relation (2.21), calculated for a linearly polarized (along the y direction) Laguerre-Gauss beam having a topological charge $q = +5$. Combining them together and weighting the different terms by the two coefficient factors c_2 and c_S, equation (2.21) reproduce correctly the spiral surface relief if the surface coefficient is set to the value $c_S = 8\ (c_2/\lambda)$. This particular value of the coefficient ratio corresponds to set a ratio in the diffusion constants of equation (2.11) at the value $D_S/D_B \approx 10$, meaning an enhanced diffusion of the molecules at the surface of about one order of magnitude respect to the bulk polymer, which is a reasonable result.

The simulated spiral surface relief obtained in this way is presented in Figure 2.2(b), where a clear qualitative agreement with the experimental spiral surface relief reported in Figure 1.6(c) is immediately recognizable. Beside the qualitative reproduction of the spiral surface relief, also the dependence on the beam topological charge is in complete agreement with the prediction of equation (2.21) and the actual phenomenological choice of the coefficient ratio. In Figure 1.6(d), the change in the handedness of the arms of the experimentally spiral surface relief under the change of the topological charge sign has been presented. Such inversion is observed also in the reliefs predicted by equation (2.21), as can be observed in Figure 2.2(d). The change in the sign of the topological charge affects only the surface mediated terms in equation (2.21) (Figure 2.2(c)), while all the other terms remain unchanged under the inversion from $q = +5$ to $q = -5$, in the specific example considered here. Furthermore, the model provides also the correct qualitative predictions about the dependence of the observed spiral surface reliefs on the absolute value of the q.

Figure 2.3 presents five spiral surface reliefs inscribed onto our azopolymer film with a linearly polarized Laguerre-Gauss beam at increasing values of the topological charge from +1 to +20. The experimental reliefs show an increase of the transverse extension of the spiral and an increasing rotation angle of the spiral arms with respect to the y-axis (vertical direction in the images). These observations are reconstructed also

in the spiral reliefs simulated through equation (2.21) (reproduced from references [8,46]), highlighting once again the qualitative agreement of the model and the relevance of the surface enhanced mass-migration term in this particular experimental situation.

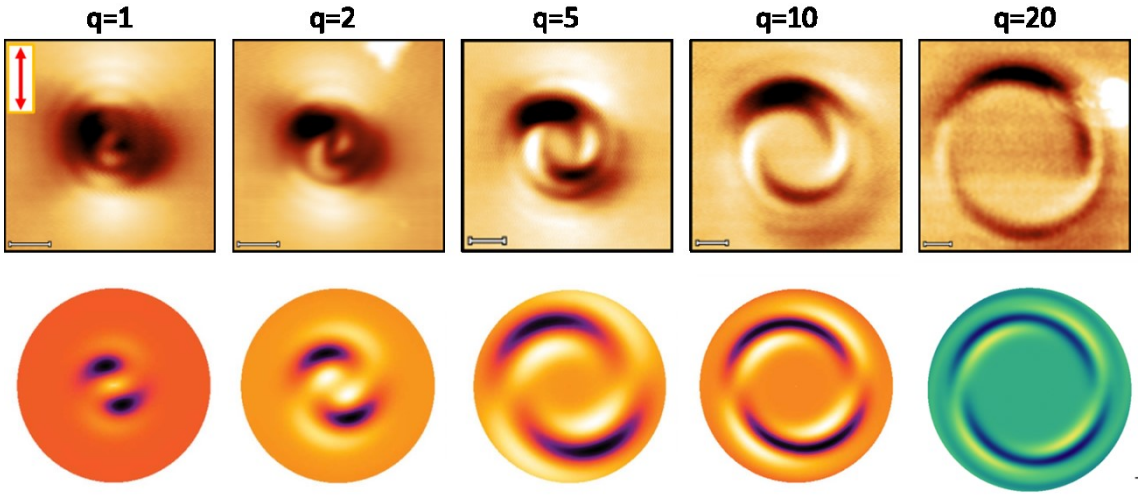

Figure 2.3| Comparison between the AFM experimental images and theoretical predicted spiral surface reliefs induced by the irradiation of a highly-focused Laguerre-Gauss beam at increasing values of the topological charge *q*. All the experimental reliefs are inscribed in our azopolymer by maintaining fixed the beam power (7 μW) and exposure time (40 s).The scale bar in the AFM images correspond to 500 nm. The simulated surface reliefs are reproduced from the references [8,46].

2.2 Surface reliefs recording the complex field distribution

From the discussion conducted so far, we can conclude that the spiral material transport observed by the irradiation of a focused beam endowed with a vortex beam can be univocally ascribed to the particular helical-shaped wavefront of these beams. The sensitivity to the wavefront of the light-driven mass migration adds another degree of freedom to the irradiation parameters, over the already well-known intensity and polarization dependences, one can use design more complex patterns onto the surface of this class of photo-responsive materials. The phenomenological model described here, even if it is approximated in some aspects and hence non able to perform quantitative predictions, gives moreover the possibility to directly link the spatial configuration of the optical field irradiating the material with the topographic modification of its surface.

However, in principle, one can even try to follow the theoretical model in the ideal inverse direction: use the encoded surface reliefs to characterize some specific parameter of the optical field used in the azopolymer irradiation. To give a concrete example, we have seen that the handedness and the lateral extension of the spiral arms induced during the spiral mass migration uniquely depend on the sign and the absolute value of the vortex beam topological charge. It becomes immediately reasonable to suppose that, whenever we observe a spiral mass migration having the mentioned phenomenology, we are in presence of an optical vortex in the illuminating beam. A similar study can be used to effectively characterize a device which is expected to generate optical vortices. Furthermore, this approach can sustain a given hypothesis on the actual complex distribution of the optical field in the space by comparing the experimental observed surface reliefs with the theoretically predicted ones. In the following two paragraphs, the optical fields generated by two optical modulator devices, namely a dielectric meta-surface able to generate optical vortices and a liquid-crystal device producing spatially varying polarized beams, are characterized by the comparison between the surface reliefs they produce onto the azopolymer and the topography predicted by relations (2.20) and (2.21).

2.2.1 Spiral surface relief for the characterization of a spin-to-orbital dielectric meta-surface converter

Until now, we have discussed about the use of the vortex beam to generate surface reliefs onto the azopolymer surface, but no details about how these beams can be generated have been given. As already mentioned, these beams are characterized by the dependence of the azimuthal phase evolution around the propagation axis of the type $\exp[iq\varphi]$ resulting in a singularity along the optical axis which gives rise to the optical vortex. There are different ways to impose such azimuthal phase dependence in the wavefront of a light beam. A commonly used method is the wavefront shaping operated by means of a spatial light modulator (SLM) programmed to visualize the so called pitch-fork holograms [21]. This is indeed the way all the vortex beams used in the experiments reported in the previous paragraphs (and in references [8,46]) are generated. The principle used to design such holograms is based on the calculation of the interference pattern produced in a plane transverse to the optical axis by a vortex beam and a slanted reference optical plane wave [57,58].

Another approach for vortex beam generation is instead based on the use of devices exploiting the geometrical phase (also known as Pancharatnam-Berry PB phase) to

create inhomogeneous gratings for the wavefront reshaping [50,59]. The devices maxing use of such principle are able to transform the spin angular momentum carried by a circularly polarized beams into the orbital angular momentum carried by a beam having an helical wavefront (Figure 2.4a). The most used spin-to-orbital (SOC) angular momentum converters is a liquid crystal device known as *q-plate* [53]. However, there is interest in developing spin-to-orbit angular momentum converters able to circumvent the limitations in terms of degradation and resolution of these liquid crystal devices. Recently, we proposed and characterized an efficient and versatile SOC [58] constituted by a dielectric meta-surface (Figure 2.4(b)). This device has the enhanced performances in terms of complex wavefront shaping, respect to the liquid crystal devices, allowing the generation of vortex beams having arbitrary integer and fractional topological charges.

Even if a complete characterization of the device can be made by interference studies between the beam modulated by the SOC with collinear and/or slanted reference plane waves (as is performed extensively in reference [60]), the presence of an optical vortex on the axis of the beam emerging from the SOC device can be uniquely demonstrated through an experimental verification of the spiral mass migration that this beam should induce onto the azopolymer film. As discussed above, the presence of spiral arms in the surface reliefs, flipping and/or rotating under a change in the sign of the vortex topological charge and under an eventual rotation of the direction of the linear beam polarization [8], can be used as a fingerprint of the presence of an effective optical vortex. In order to understand how the SOC device in able to generate vortices having opposed charge signs, a brief discussion about the working principle and the fabrication strategy of these converters can be useful [53,60].

The SOC dielectric meta-surface shown in Figure 2.4(b) is constituted by sub-wavelength TiO_2 optical resonators, termed as *nanofins*, (Figure 2.4(c-d)), whose spatial dimensions (height h, width W, length L) are properly chosen such that each of them induces a π-phase delay between the transverse components E_x and E_y of a propagating optical field. In the SOC design strategy, each of these nanofins has a variating orientation angle $\alpha(r, \varphi)$ in the device plane (Figure 2.4(d)), which induces a geometrical phase variation in the wavefront of a propagating beam.

Using the Jones formalism for the description of the light polarization state, the Jones matrix of a nanofin in the polar position (r, φ) of the device plane, is:

$$M(r,\varphi) = R\left[-\alpha(r,\varphi)\right]\begin{pmatrix}1 & 0\\ 0 & -1\end{pmatrix}R\left[-\alpha(r,\varphi)\right] = \\ = \begin{pmatrix}\cos\left[2\alpha(r,\varphi)\right] & \sin\left[2\alpha(r,\varphi)\right]\\ \sin\left[2\alpha(r,\varphi)\right] & -\cos\left[2\alpha(r,\varphi)\right]\end{pmatrix}, \tag{2.22}$$

where $R(\alpha)$ is the matrix for the rotation of an angle $\alpha(r,\varphi)$, and the matrix describing the π-phase delay has been used. If the incident field is right circularly polarized, its Jones vector is $E_{inc} = \begin{pmatrix}1\\ i\end{pmatrix}$ and the field emerging from the device is:

$$E_{out} = M(r,\varphi)E_{inc} = E_0 e^{i\,2\alpha(r,\varphi)}\begin{pmatrix}1\\ -i\end{pmatrix}. \tag{2.23}$$

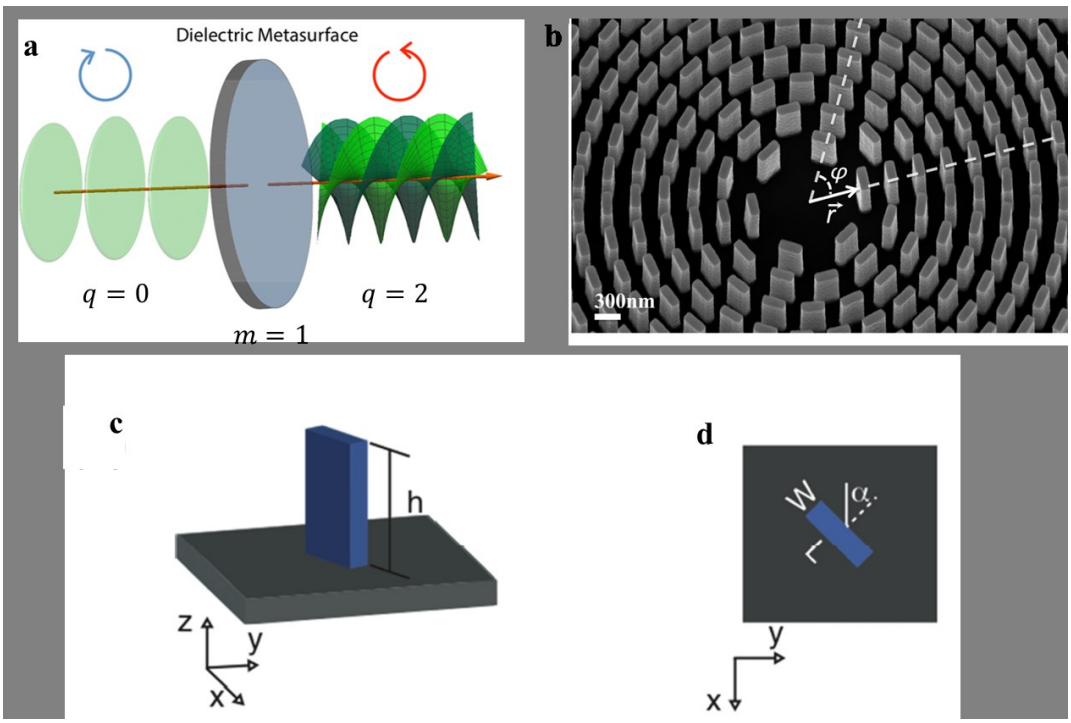

Figure 2.4| The dielectric metasurface used for spin-to-orbit angular momentum conversion (SOC). (a) Schematic representation of SOC principle. (b) SEM image of the dielectric metasurface fabricated by electron beam lithography and atomic layer deposition of TiO_2. (c) and (d) schematic representation of the nano-resonators, whose geometrical parameters and orientation angle are tuned to achieve an overall π-phase delay between the electric field transverse components and a geometrical phase $\alpha(r,\varphi) = q/2 + \alpha_0$.

In order to induce an optical vortex of charge q, the distribution of the nanofins orientation angles in the device plane should to be chosen as:

$$\alpha(r,\varphi)=\frac{q}{2}\varphi+\alpha_0\,. \tag{2.24}$$

Indeed, relation (2.24) would imply a geometrical phase term exp[$iq\varphi$], which is the helical wavefront of a vortex beam having a topological charge $+q$. Furthermore, from the relations (2.23) and (2.24), we have that an incoming right circularly polarized beam would be transformed in a helical mode with left circular polarization. Inverting the headedness of the incident circular polarization, the same device generates a vortex beam with the opposed topological charge sign ($-q$).

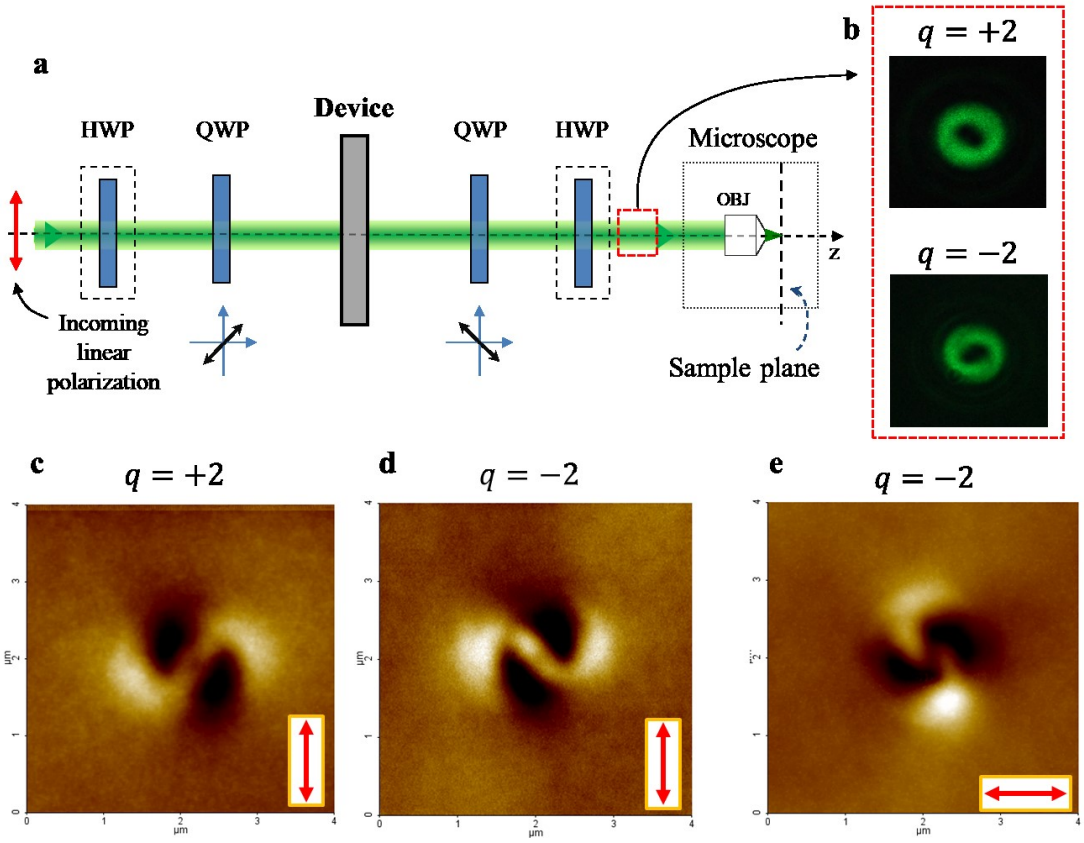

Figure 2.5| Spiral mass transport generated by a beam emerging from the meta-SOC. (a) Schematic representation of the setup. The two half-waveplates contained in the dashed rectangles are inserted along the optical path to change the sign of the topological charge and the polarization of the beam illuminating the azopolymer. (b) Cross section of the beam intensity profile before the microscope for both the charges $q = \pm 2$. (c) and (d) AFM images of the spiral surface reliefs obtained with vertical polarization and opposed vortex charges, respectively. (e) AFM image of the spiral relief obtained by rotating the light polarization direction by 90°. The laser irradiation conditions are: power 65 μW, exposure time 20s.

In Figure 2.5 is presented the characterization, by means of the surface reliefs a beam modulated through the devices, of one of these SOC metasurfaces, designed to produce optical vortices of charge ±2. A linearly polarized laser beam at $\lambda = 532\ nm$ is transformed in a right circular polarized beam by and half-waveplate before crossing the meta-SOC device in order to produce the q=+2 optical vortex. The polarization of the modulated beam is then reconverted to linear by a second half-waveplate before the beam is injected into the lateral port of an inverted microscope, equipped with an oil immersion 100X objective (NA=1.4), and focused onto the spin-coated azopolymer film (Appendix A).

The cross sections of the beam intensity profile before the microscope is presented in Figure 2.5(b-top). It is characterized by the expected typical doughnut-like intensity cross-section of a light beam endowed with an optical vortex. Furthermore, the actual helical-shaped wavefront of the modulated beam is clearly demonstrated by the spiral surface relief the beam induces onto the azopolymer surface, as presented in Figure 2.5(c). Also the inversion of the spiral mass transport handedness under the inversion in the sign of the topological charge is found. In this case, a half-waveplate is inserted along at the beginning of the optical path in order to achieve a left circular polarization for the beam traversing the SOC. The doughnut-shaped intensity profile is realized also in this case Figure 2.5(b-bottom), and it results indistinguishable from the previous case. However, the spiral arms of the surface relief onto the azopolymer are clearly characterized by an inverted handedness (Figure 2.5(d).

Furthermore, a rotation of 90° of the whole spiral relief is obtained by rotating by 90° the linear polarization direction of the beam carrying the topological charge q=-2 (Figure 2.5(e)), according to the results reported in [8]. These observations confirms all the predictions of the phenomenological mass migration model described in section 2.1 and unambiguously recognize the presence of the optical vortex on the axis of the beam modulated trough the dielectric metasurface, confirming, moreover, the success of all the device designing approaches, starting from the nano-resonator design till the actual inscription of the geometrical phase onto the wavefront of the modulated beam.

2.2.2 Field distributions generated from the *θ-cell*

Another situation where the surface reliefs induced onto the azopolymer film can be used as an experimental proof for the actual distribution of the optical field components in focal region of an high-numerical aperture microscope objective, concerns the

commercially avaliable liquid-cristal cell used to produce radial or azimutal polarized beams: the *θ-cell.*

The θ-cell consists of a liquid-crystal cell characterized by two different LCs alignment layers at the cell interfaces [61,62]. In particular, one layer is rubbed unidirectionally to achieve a linear alignment of the LCs in contact with it, while the other layer has a circular rubbing orientation (Figure 2.6(a)). The direction of the linear rubbing defines also the cell axis. The schematic representation of the liquid crystal orientations inside the cell as viewed from the top is presented in Figure 2.6(b). The twist angle for the liquid crystals at different positions in the cell is always smaller than π/2. This characteristic produces a defect line (dashed line in Figure 2.6(b)) in correspondence of the inversion in the sign of the liquid crystal twist angle. In this region, which has a width of few tens of microns, the liquid crystal alignment is not defined [62].

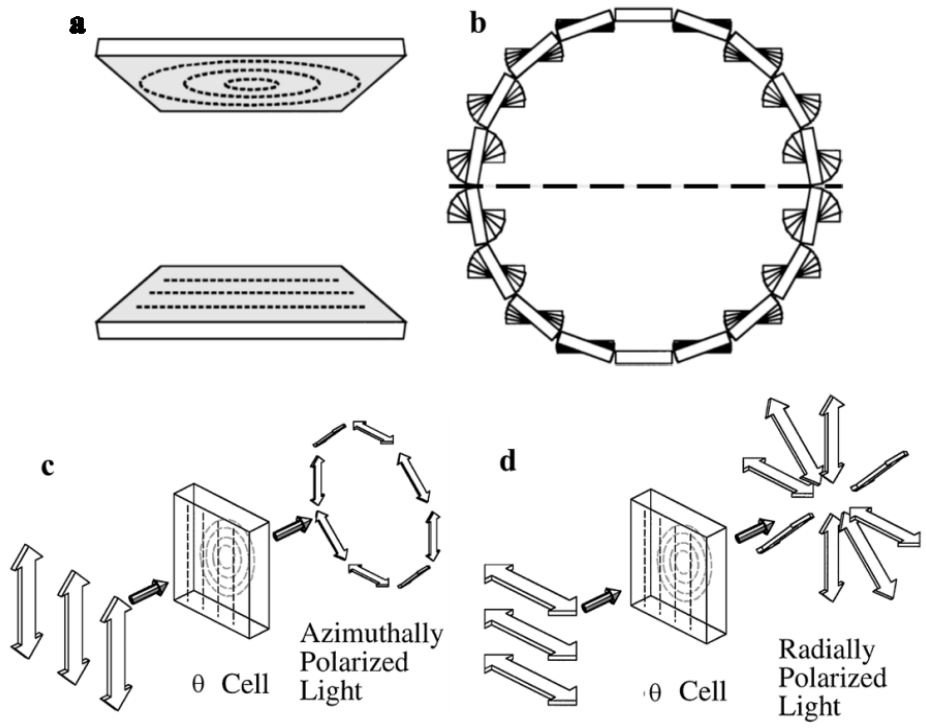

Figure 2.6| Working principle of the liquid crystal θ-cell. (a) Schematic representation of the alignment layers for the LC at the two faces of the cell. (b) Representation of the spatial dependent LC twist angle, producing the θ-cell defect line. Configuration producing Azimuthal (c) and Radial (b) polarized beams from a linearly polarized beam. Images reproduced from reference [62].

The spatial dependence of the twist angle of the birefringent liquid crystals over the θ-cell plane is able to convert a linearly polarized beam, incident onto the cell from the side of the linear rubbing, into azimuthally or radially polarized beams. In particular, if the incoming polarization direction is parallel to the cell axis, an azimuthally polarized beam (Figure 2.6(c)) is obtained after the cell. Otherwise, if the polarization of the incoming beam is orthogonal to the cell axis, a radially polarized beam emerges from the cell (Figure 2.6(d)).

However, besides the reorientation of the local linear polarization direction of an optical field travelling through the device, the θ-cell induces also a π-shift in the phase of the light passing through the two sides of the cell defect line [55]. While such phase-shift does not affect the actual polarization direction of the light emerging from the cell, and can be neglected in many experimental situations where only the directional polarization state is relevant (see for example section 5.4 of the present thesis), it has a direct influence on the optical field distributions in the case of highly focused radial and azimuthal beams, as reported in reference [55].

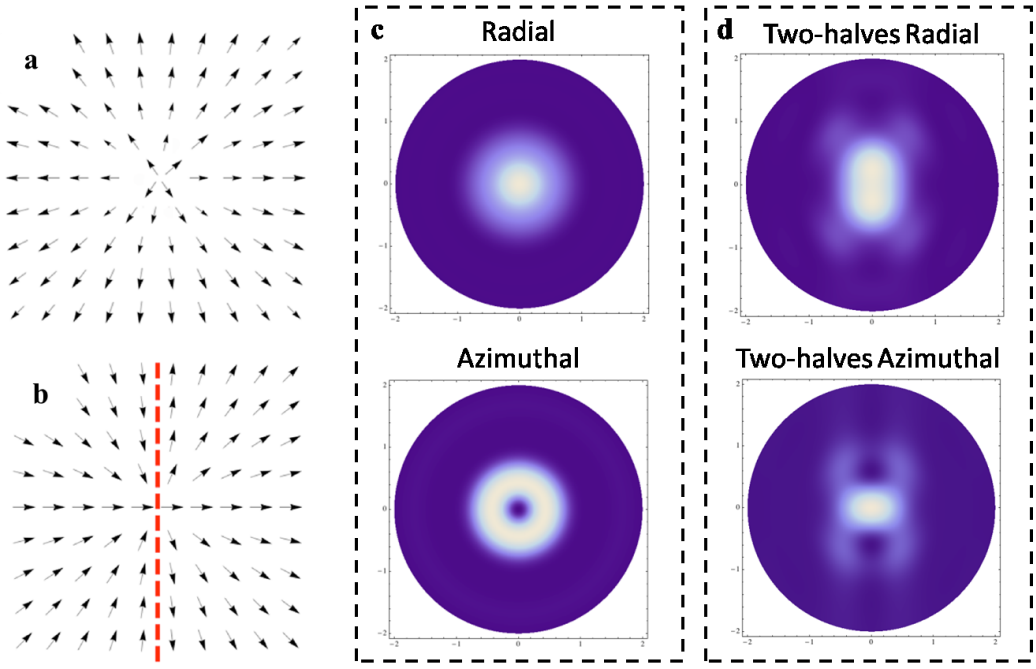

Figure 2.7| Effects of the π-phase shift induced by the two half of a θ-cell. schematic vectorial representation of the transverse electric field of a radial polarized beam (a) and the beam emerging from the cell (b) which is characterized by a π-shift between the two sides of the cell. The red dashed line in (b) indicates the cell defect line. (c) Simulated intensity distribution in focal plane of an objective lens with NA=1.4 in the case of actual radial and azimuthal polarization, and (d) for the two-halves radial and two-halves azimuthal beams.

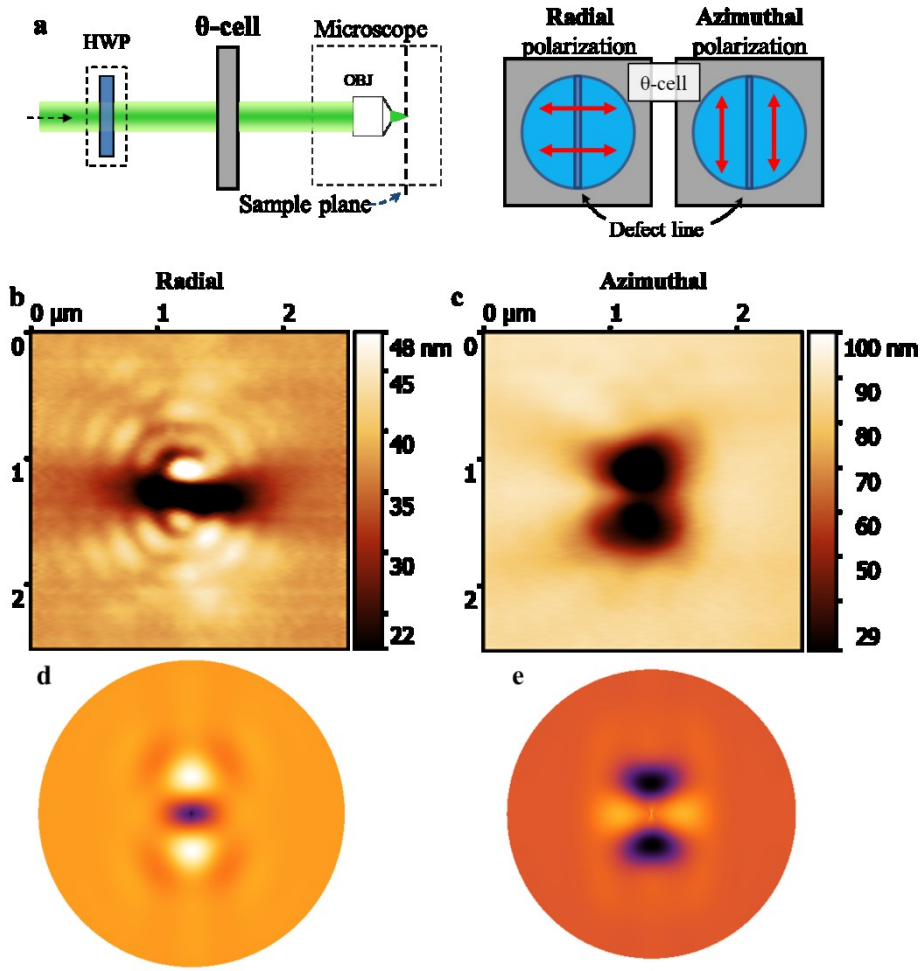

Figure 2.8| Surface reliefs inscribed by the two-halves radial and azimuthal focused beams. (a) Schematic representation of the illumination setup and θ-cell configuration for the surface relief inscription experiment. AFM images of the surface relief resulting from the radial polarized beam (b) and from the azimuthal polarized beam (c). Simulated surface reliefs from the relation (2.21) of the phenomenological model for the case of two-haves radial (d) and two-halves azimuthal (e).

Following the nomenclature presented in that study, the optical fields produced by the θ-cell are named as *two-halves radial* and *two-halves azimuthal* in order to highlight the phase shift in the two half sides of the cell. In Figure 2.7(a) and Figure 2.7(b) this situation is described visually by the comparison between the vectorial representation of a radial polarized field and the two-halves polarized field obtained from the θ-cell. Simulating [8,55] the intensity distribution of the focal region of a high numerical aperture objective (NA=1.4) we can observe a significant difference between the intensity pattern predicted for the actual radial and azimuthal polarized beams (Figure

2.7(c)) and the two-halves polarized beams (Figure 2.7(d)). A complete characterization of the different components of the optical field has been performed both theoretically and experimentally in reference [55], confirming the effect of the cell defect line as simulated in Figure 2.7(d), however once again we can use the surface reliefs produced by the actual beams modulated by the θ-cell onto the azopolymer to further characterize the device and the optical field distributions it produces.

In Figure 2.8(a) the simple experimental configuration is presented in which the linear polarized light of the laser beam at $\lambda = 532\ nm$ passes through the θ-cell device, whose axis (and its defect line) is oriented in the vertical direction. The two-halves radial or the two-halves azimuthal polarization are chosen by placing at need an half-waveplate before the device to rotate the input polarization direction. The light emerging from the liquid crystal device is then focused onto an azopolymer thin film by means of the 100X (NA=1.4) immersion oil microscope objective. The AFM images of the surface reliefs arising by irradiating the polymer with a light power of 7μW for 40s, in the two polarization conditions are shown in Figure 2.8(b) and Figure 2.8(c), respectively.

The surface reliefs presented here are characterized by a very good agreement between the experimental surface reliefs and the reliefs simulated through the relation (2.21) of the phenomenological model. As discussed in reference [55], the π-phase shift of the two-halves polarized beams affects mainly the longitudinal field component of the two-halves radial polarized beam. Indeed, an actual focused radial beam possesses a significant field component along the light propagation direction, where most of the overall field amplitude is concentrated. For this reason these beams can be used for spectral high resolution imaging [63,64]. However, the longitudinal component in the case of the two-halves radial polarized beam generated by the θ-cell has a different spatial distribution respect to the ideal radial one, limiting its use for the application where this aspect is of interest. The very good qualitative agreement between the experimental surface reliefs and the surface modulation predicted by the mass migration theoretical model in the hypothesis of the two-halves radial beam illumination indirectly confirms the actual distribution of the components of the optical fields generated by the θ-cell, and represent a very elegant experimental characterization of the device.

3 Surface Reliefs from holographic structured illumination

Holography is an optical technique able to reconstruct a desired light field in a specified plane of the optical path by properly modulating a light beam through a light-modulating device. Using a holographic method, a specific intensity pattern can be reconstructed. This is even more true for the computer-generated holograms, which use a digital representation of the desired intensity pattern, allowing the reproduction of almost arbitrary complex light distributions. In the field of the light-induced mass migration phenomenon this high degree of control in the illumination configuration can have a two-fold relevance. First, it can be used to study the phenomenon at the fundamental level. In particular, as the intensity distribution and the polarization state of the irradiated light can be controlled independently, the disentangled effects that each of them produces in terms of surface modulations can be investigated separately. This is not the case, for example, of the interference illumination patterns used for SRG inscription, where the polarization of each beam affects directly the intensity distribution of the light over the sample. Second, as the surface structuration is induced only in the illuminated areas of the azopolymer film, the fine tuning of the irradiating light intensity pattern through a holographic technique opens immediately to applications of the complex superficial textures produced with this method in the micro/nano photo-lithography. In the present chapter, the implementation of an optical setup able to reconstruct complex intensity distributions in the focal plane of a high numerical aperture objective is described. The principles underlying the calculation of the computer-generated holograms in the framework of the phase-only optical modulation are also presented. The series of complex surface reliefs obtained here in different illumination conditions and the peculiar disentangled intensity/polarization dependence clearly highlight the possibilities offered by this holographic illumination configuration of enlarging the range of both fundamental studies of the phenomenon and the possible application in the framework of the complex textured surfaces.

3.1 Computer-Generated Holograms

In 1948, Denis Gabor [65] proposed an imaging technique able to record both the amplitude and the phase of an optical field emerging from a diffracting or scattering object. Because of the difference existing in such an imaging process respect to the standard photography, able to reproduce only the amplitude of the incident optical field, he named the total encoded field information as a *hologram*, meaning "total recoding", throwing the basis of the method we now call *holography*. In Gabor's holography, the field is recorded as an interference pattern produced in the coherent superposition of a reference wave with the light diffracted by an object. Using such interference pattern as modulating mask for a light beam at the same wavelength of the one used for the hologram recording, an image of the object can be reconstructed resulting in an optical field which retrieves the original diffracted light field from the object [21]. Gabor's holography has received an increased interest over the years, and it is now the base for many scientific and technologic applications. In particular, with the development of powerful digital calculators in the last decades, many studies have been devoted to the development of new methods able to create holograms by means of a proper digital calculation process. The result is that today Computer-Generated Holograms (CGH) are able to create images of objects that in fact never existed in the real physical world, but which were simply drawn in digital form on a computer.

Analogously to Gabor's holography, once that a computer-generated hologram is calculated on the basis of some proper algorithm, then it has to be transferred to some physical optical modulator for the image reconstruction. To accomplish this task one can use, for example, a photographic films or transmission masks (printed or fabricated by lithography) [21]. However, the real advantage of the CGH imaging technique is mainly due to the possibility of direct transfer of the digitally-calculated holograms to a computer-controlled diffractive optical element. The most commonly used device is the Spatial Light Modulator (SLM). This is a liquid crystal device whose transmittance or reflectance is controlled by electric input signals.

Recent SLMs are essentially assimilable to the liquid crystal displays commonly used in technologic devices (TVs, smartphones and so on), where the electric signal driving the liquid crystal reorientation in each pixel can be independently controlled in order to reconstruct an image. In principle, for CGH implementation, the display should be programmed in such a way that its transmittance (or reflectance) results proportional to the digitally-calculated hologram. As the transmittance is a complex function of the spatial coordinates, a simultaneous and independent modulation of both the amplitude and the phase of the hologram reconstructing light beam would be needed in general.

This situation cannot be accomplished with a single SLM device. Moreover, it is not efficient in terms of light throughput. Indeed, due the diffractive nature of the display, the light emerging from the SLM is divided among many diffraction orders, which contain each a small fraction of the total incident power. An amplitude spatial modulator would further lower the light power in each of the modulated diffraction order by the selective absorption of the light necessary for the modulation. This feature makes the amplitude modulation approach unusable in many practical situations where the light power is a control parameter for the phenomenon of interest. One example is represented by optical tweezes, where the majority of the advantages related to the use of the SLMs and CGH are typically highlighted [66,67].

A suitable approach for many practical applications is represented by the *phase-only* CGH design, where the amplitude modulation is completely excluded and the reconstruction of the holographic image is accomplished by modulating only the wavefront of the light beam. This hologram (often named as *kinoform*), has to be accurately calculated in order to approximately enclose the total hologram information (amplitude + phase) in a pure phase profile. Over the years, many algorithms have been proposed for the kinoform calculation, each having advantages related to specific applications [67]. In particular, the Gerchberg-Saxton (G-S) algorithm [68], is one of the most used algorithm for kinoform calculation in situations where the reconstruction of bidimensional structured intensity patterns is of interest. This algorithm constitutes the basis of the calculation design for the spatially structured holographic intensity patterns used here to illuminate the surfaces of the azopolymer films. The G-S algorithm is described in detail in the next paragraph.

3.1.1 The Gerchberg-Saxton algorithm for phase-only CGH

Many algorithm schemes used for kinoform calculation in the phase-only CGH are based on the relationship existing between the complex optical fields in the two focal planes of a lens. As established by the theory of the scalar Fourier optics [21,51,69], the propagation through the free space of the optical field from a given plane of the optical axis (source plane) to the far-field, produces an optical field which can be described as the Fourier transformation of the field in the considered source plane [38,42,43]. The same Fourier relation exists also between the optical fields in the focal planes of a lens, which is regarded as realizing the so-called *2f-geometry* (Figure 3.1(a)). Explicitly, the optical field $U_{II}(x_{II}, y_{II})$ in the second lens focal plane (plane II) is written in terms of the optical field $U_I(x_I, y_I)$ in the first lens focal plane (plan I) as:

$$U_{II}\left(x_{II}, y_{II}\right) = FFT\left[U_I\left(x_I, y_I\right)\right]. \tag{3.1}$$

Equation (3.1) represents an operative definition for the calculation process one has to follow to build a computer generated hologram. Once the intensity pattern to be reconstructed is specified as a target intensity image $I_t(x, y)$, the 2f-geometry permits to identify the plane II as the image reconstruction plane, and the plane I as the hologram plane, where the modulation of the optical field is achieved (for example through the spatial light modulator placed in that plane, as shown in Figure 3.1(b)).

In the framework of the phase-only CGH, the hologram calculation problem can be reduced to the calculation of a phase profile $\phi_I(x_I, y_I)$ (kinoform), to be imposed onto the beam wavefront in correspondence of the first lens focal plane, such that the following relation is verified:

$$I_t\left(x_{II} y_{II}\right) = \left(FFT\left\{\exp\left[i\phi_I\left(x_I, y_I\right)\right]\right\}\right)^2. \tag{3.2}$$

In phase-only CGH, the amplitude information of the complex optical fields is not used for effective light modulation, and the phase profile $\phi_I(x_I, y_I)$, solution of equation (3.2), can be found only in approximated form by an iterative calculation process. The basic idea of the G-S algorithm, whose flow chart is shown in Figure 3.1(c), is to operate a series of propagations of the optical fields between the lens focal planes with the task of encoding the shape of the target intensity profile into a pure phase hologram. This is practically accomplished by a series of Fourier transformations (because of the 2f-geometry configuration) in which, at each propagation step, only the phase information emerging from the Fourier transformation of the field is preserved, while the field complex amplitude is manipulated in order to account for the actual phase-only modulation scheme.

More in detail, the algorithm is initialized (at the algorithm iteration n=1) assuming a randomly distributed phase profile ϕ_r and unitary amplitude for the optical field in the plane I:

$$U_{input,1} = \exp\left(i\phi_r\right). \tag{3.3}$$

This field is then propagated in the image reconstruction plane (plane II) by taking its Fourier transform. This operation is repeated at each iteration step, where the input field $U_{input,1}$ is substituted, in the n-th iteration by $U_{input,n}$ as resulting from the algorithm calculation at the (n-1)-th step. From equation (3.1), the field in the image plane at n-th iteration is given by:

$$U_{II,n} = FFT\left[U_{input,n}\right] = a_{II,n}\exp\left(i\phi_{II,n}\right). \tag{3.4}$$

This field is manipulated in order to artificially build the field $U^*_{II,n}$ in the image plane by keeping the phase of the field $U_{II,n}$ and substituting its original amplitude $a_{II,n}$ with the amplitude of the target intensity pattern I_t:

$$U^*_{II,n} = \sqrt{I_t}\exp\left(i\phi_{II,n}\right). \tag{3.5}$$

The inverse Fourier transformation of (3.5) propagates the field back in the hologram plane:

$$U_{I,n} = FFT^{-1}\left[U^*_{II,n}\right] = a_{I,n}\exp\left(i\phi_{I,n}\right) \tag{3.6}$$

Here, a new artificial field $U^*_{I,n}$ is built from $U_{I,n}$ by maintaining the original phase profile, but substituting the amplitude $a_{I,n}$ with the unitary amplitude $a^*_{I,n} = 1$:

$$U^*_{I,n} = a^*_{I,n}\exp\left(i\phi^*_{I,n}\right) = \exp\left(i\phi_{I,n}\right). \tag{3.7}$$

The operation described in equation (3.7) is where the actually phase-only modulation scheme is effectively taken into account. The field $U^*_{I,n}$ constitutes the input field for the (n+1)-th algorithm iteration, or alternatively, it constitutes the algorithm output at the final (N-th) iteration

$$U_{out} = U^*_{I,N} = \exp\left(i\phi_{I,N}\right). \tag{3.8}$$

The searched solution for the kinoform then is the phase profile of the field U_{out} :

$$Kinoform = \arg\left(U^*_{I,N}\right). \tag{3.9}$$

The Gerchberg-Saxton algorithm converges after the few iterations (in the order of N=10 [70]. However, even if the kinoform resulting from the calculation process is able to reconstruct very complex light intensity patterns, it suffers (as described in the next paragraph) of *speckle* noise [71] originating from the algorithm initializing random phase profile described by equation (3.3). As the speckle noise affects the contrast and the resolution of the reconstructed holographic image, a technique suited to its reduction is necessary for the effective use of such digital holography technique in applications where the homogeneity of the illumination pattern is a demanding point [72].

In the next paragraph, the effective implementation of the CGH setup and the characterization of its performances in terms of generation of structured intensity patterns are discussed.

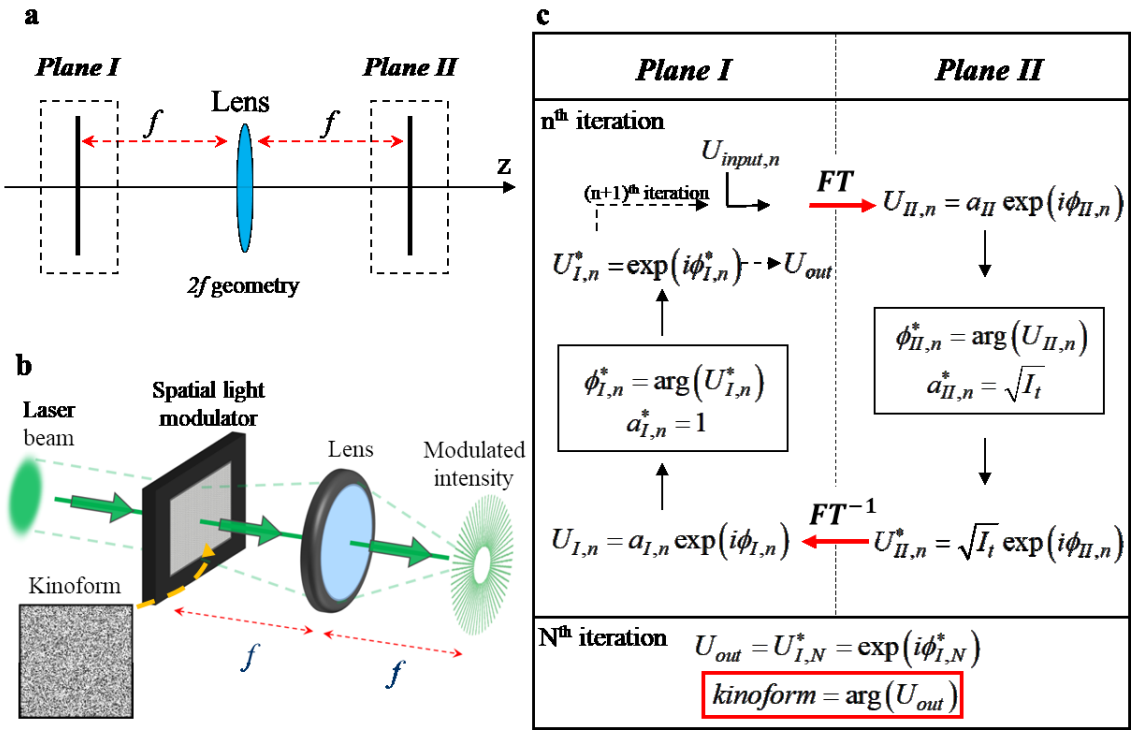

Figure 3.1| Optical configuration for computer generated holograms. (a) Scheme of the *2f geometry* and specification of the planes whose optical fields are related by the Fourier transform relation. (b) Scheme of the optical configuration for the effective implementation of CGH by the use of a SLM placed in the hologram plane. (c) Flow chart of the Gerchenberg-Saxton algorithm.

3.1.2 Optical setup

The schematic representation of the setup used for the illumination of azopolymer films with the holographic computer-generated intensity patterns generated is shown in Figure 3.2(a). The laser beam at λ=532 nm (from Nd:YVO4 continuous-wave frequency-doubled laser), after a beam expander (lenses L_1 and L_2), is reflected onto the computer controlled phase-only SLM (Holoeye Pluto) programmed to visualize the desired kinoform, and placed in the first focal plane of the lens L_3. This lens realizes the 2f-geometry for the propagating beam with an iris placed in its second focal plane. The beam, diffracted and modulated by the SLM (working in reflection mode), is then transmitted through the lens L_3, and focused in the iris plane, where a first reconstruction of the holographic image is obtained. The iris in this particular plane allows the spatial filtering of the beam, rejecting all the undesired light diffraction orders and the un-modulated light emerging from SLM. After the iris, the beam is re-

collimated by the lens L_4 and finally focused onto the sample located in the microscope (the inverted microscope Axio-Oberver from Zeiss) sample-holder by means of the external lens L_5 and the microscope internal lens systems (including tube lens L_T and the microscope 100X oil-immersion objective, NA=1.4). When needed, a CCD connected to the microscope (not shown in the scheme of Figure 3.2) is able to collect either the bright-field image of the sample illuminated by a halogen lamp or the image of the reflected/back-scattered light in the epi-illumination configuration with the laser beam as illuminating source.

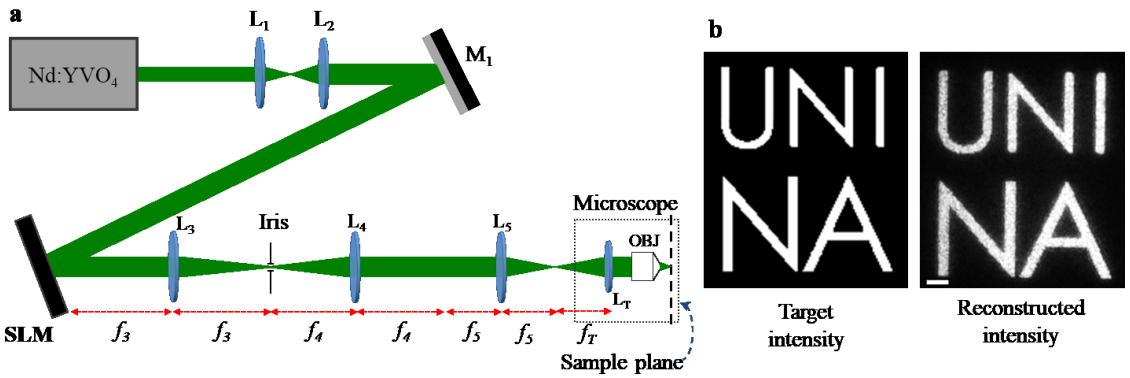

Figure 3.2| Optical scheme of the CGH setup and its ability in reconstructing time-averaged complex intensity patterns. (a) Schematic sketch of the optical setup built on the basis of the 2f geometry for CGH. Segments f_i denote the focal lengths of the corresponding lenses L_i (focal lengths: f_3 = 400 mm, f_4 = 400 mm, f_5 = 200 mm). (b) Comparison between a digital target intensity pattern and the time-averaged intensity pattern reflected by a silver mirror placed in the sample plane. Scalebar of the reconstructed intensity image 2 µm.

The ability of the described optical system in the generation of complex intensity patterns is shown in Figure 3.2(b). Here, the comparison between the intensity pattern used as target intensity for the kinoform calculation and the actual intensity profile reconstructed in microscope sample plane is presented. The target intensity is specified as a grayscale digital image, built and manipulated with generic graphic software. In the particular case of Figure 3.2(b), the target intensity is a simple sequence of bright text characters over a dark background. This image is processed for kinoform calculation using the Gerchberg-Saxton algorithm implemented by a custom Matlab routine, based on the discrete-FFT calculation. The number of algorithm iterations is set typically at 50, but not visible differences have been found in the quality of the reconstructed intensity images even for 5 iterations.

The SLM is controlled by a LabVIEW routine which allows the sequential display of a fixed number of different kinoforms at given framerate (until the maximum framerate of 60 Hz). This feature, as discussed below, is necessary for the reduction of intensity fluctuations normally generated in the reconstructed holographic images, and it is fundamental for the effective use of the CGH for light-driven superficial structuration azopolymer films.

3.1.3 Speckle noise reduction

As discussed in section 3.1.1, the G-S algorithm is initialized by a random phase profile, necessary to guarantee the convergence [70] of the approximate solution of equation (3.2). This random phase profile is not completely eliminated in the algorithm steps, even for large numbers of iterations, and results in a granular intensity pattern (the *speckle pattern*) superimposed to the reconstructed holographic image.

A speckle pattern [73] is typically observed in coherent light beams reflected by a rough surface. In this case, the superficial roughness in the scale of wavelength produces a random modulation in the amplitude and in the phase of the incoming beam. Interpreted as the convolution of secondary wavelets, the coherent superposition of such dephased and modulated waves produces a mutual interference which results in a granular intensity pattern in the far-field. This pattern has bright spots in the random positions where the interference is constructive and dark regions where the interference is randomly destructive.

In the case of CGH, the random phase profile of the G-S initialization step acts as a source of randomly distributed dephasing for the beam wavefront at the SLM pixel scale. The result of such random dephasing is that the holographic reconstructed image has a superimposed speckle intensity pattern. This granular pattern limits the homogeneity of the reconstructed holographic image and represents a source of un-desiderated noise. As this noise depends on the random initializing phase of the calculation algorithm, different kinoforms calculated from the same target intensity profile are characterized by different speckle patterns. The random nature of this holographic speckle noise, however, allows a very simple approach for its reduction, suitable in all the applications where the light-induced physical process of interest occurs on a time scale relatively longer (few seconds) respect to the SLM refreshing rate (60 Hz). This is indeed the case of the light-driven mass transport in azomaterials.

The speckle noise reduction strategy is simply based on time average of the random speckle noise. This temporal mean is practically realized by the sequential display of

several independent kinoforms calculated from the same target intensity profile [71,72,74,75]. The result is an homogenous mean holographic intensity pattern in which the granularity of the speckle noise affecting each reconstructed image individually is drastically reduced [72,75].

In order to characterize the speckle noise reduction achievable by the kinoform temporal averaging method, the reconstructed images obtained by varying the number of time-averaged independent kinoforms have been characterized through the measurement of speckle dependent quantities. The main results of this characterization are reported in Figure 3.3. The parameter commonly used to characterize the granularity in the images affected by the speckle noise is the *speckle severity S* [76,77], defined as:

$$S = \frac{\sigma}{\langle I \rangle}, \tag{3.10}$$

where $\langle I \rangle$ is the mean intensity, and σ is the intensity standard deviation measured in the image:

$$\langle I \rangle = \frac{1}{M} \sum_{i=1}^{M} I_i \quad , \tag{3.11}$$

$$\sigma = \frac{1}{M-1} \sum_{i=1}^{M} \left(I_i - \langle I \rangle \right)^2 \quad . \tag{3.12}$$

From the definition in equation (3.10) it follows that the more the intensity distribution in the image is granular (higher values of σ), higher is the value of the parameter *S*.

In order to actually measure the speckle severity of our holographic scheme, a series of 200 images of the holographic intensity light pattern reflected by a silver mirror, placed in the microscope sample plane, is collected by the CCD connected to the microscope. The number N of different kinoforms displayed cyclically (with a refresh time of 200 ms) onto the SLM is variated from N=1 to N=50. For each N, a single image (the *summed image*) is reconstructed by summing together all the 200 frames in the stack. In Figure 3.3(a) are presented some of the summed images of the reconstructed holographic patterns obtained for different values of displayed kinoforms N.

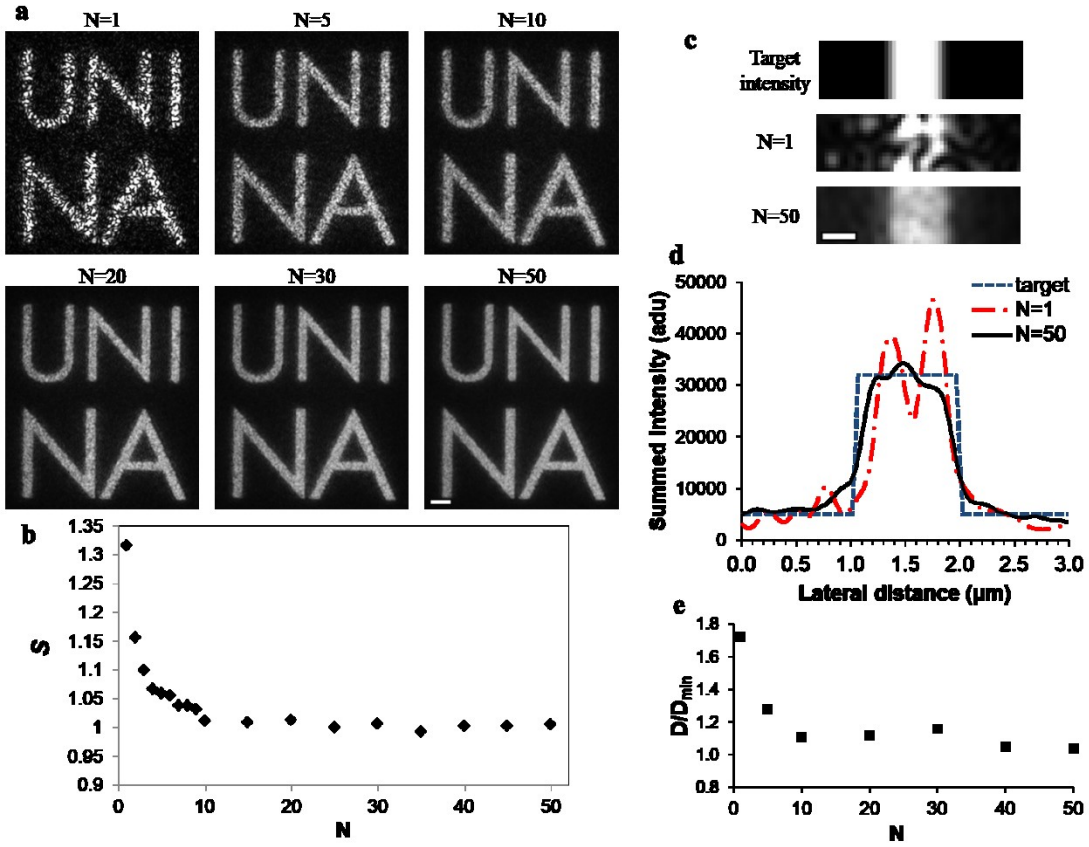

Figure 3.3|Speckle noise characterization and its reduction. (a) Summed images of the CCD acquired stacks (200 frames each) reconstructed for different number N of independent kinoforms cyclically displayed onto the SLM. The scalebar in the images (specified in the panel N=50) is 2μm. (b) Speckle severity measured in the images for different N. (c) Comparison of a zoomed feature of the holographic reconstructed images and (d) their relative intensity profiles (scalebar in (c) 500nm). Normalized discrepancy parameter D evaluated on the profiles of type (d) for different number of independent kinoforms.

A significant reduction in the intensity granularity is evident for increasing numbers of averaged kinoforms. This is also confirmed by the decreasing behavior of the speckle severity with the increasing of N (Figure 3.3(b)). However, even if the parameter S saturates at the value of about S=1 starting from N=10, the visual comparison of the reconstructed images for larger values of N shows a slight improvement trend in terms of homogeneity in the bright regions and the summed image for N=50 appears less noisy than the others. Indeed, the restriction of the speckle severity analysis to a small number of pixels corresponding to an illuminated region of the image (not shown here for brevity), shows a slower saturating trend for the parameter S and an appreciable

difference at large values of N (40-50) respect to analysis conducted on the entire image.

Beside the image homogeneity, the speckle noise affects also the sharpness of the time-averaged intensity pattern. This effect is described in Figure 3.3(c) through the comparison between a zoomed view of a region of the intensity target profile and the reconstructed holographic image of the same region obtained for N=1. As can be seen from the images, the granular intensity fluctuations on the scale of the optical resolution limit (250 nm) induce a significant degradation of the sharpness in the intensity profile. However, the situation is improved significantly by the temporal average operation, as can be observed in the image in Figure 3.3(c) obtained for N=50 and from the comparison of the intensity plot profiles measured in the images (Figure 3.3(d)).

In order to qualitatively characterize the sharpness of the reconstructed averaged intensity and the deviation of its profile from the target, a discrepancy parameter D can be used. This parameter is defined as the mean square deviation between the target and the measured intensity profiles and it is intended as an estimator of the intensity fluctuations of the holographic images around the target pattern:

$$D = \frac{1}{K}\sum_{i=1}^{K}\left(I_{i,meas} - I_{i.\text{target}}\right)^2 . \tag{3.13}$$

In Figure 3.3(e), the values of the parameter D (normalized to the minimum observed one D_m) estimated for different number N of averaged kinoforms are presented. A decreasing trend in the discrepancy as N increases if found also in this case, confirming that the averaging kinoforms noise reduction is effective for both image total homogeneity and resolution of the holographic reconstructed intensity patterns.

However, it should be further stressed that similar noise suppression is effective only if the process of interests is insensitive to the instantaneous intensity pattern. Indeed, dealing with a physical process depending on the total energy deposited in the illuminated sample, as for the light-driven mass migration in azopolymers, the average of light modulation over different kinoforms (affected each of independent random speckle noise) on the temporal scale of few seconds[2] becomes a powerful noise-suppression technique which allows the effective use of CGH for complex surface structuration of the azopolymer films.

[2] Using the SLM at its maximum refresh rate of 60Hz, the sequential display of N=50 different kinoforms implies an exposure time for each cycle of 0.84s. Even the use of a refresh rate of 5 Hz requires a total exposure time of 25 s, which is typically shorter than the exposure time needed to inscribe the surface reliefs onto the azopolymer film.

3.2 Holographic Surface Reliefs: Experimental configuration

Once the ability of the CGH setup for the generation of complex and time-averaged homogenous intensity patterns has been established, the attention is now moved to the surface reliefs that these complex illumination patterns are able to induce onto the surface of our azopolymer films. In the experiments, the samples are prepared in form of thin films as described in Appendix A.

In all the experiments, the time-average for speckle noise reduction is achieved by using 50 independent kinoforms, cyclically displayed onto the SLM at the refreshing rate of 5 Hz during the whole polymer exposure time. The polarization of the beam is controlled by waveplates (half-wave or quarter-wave plates) placed along the optical beam path. The power of the laser beam during the experiments, measured in correspondence of the microscope entrance port, is in the range of 10-100 μW, depending on the actual distribution and lateral extension of the particular holographic illuminating intensity pattern under consideration. However, the light intensity at the sample plane is estimated to not exceed 1 kW/cm^2 in all the experiments.

3.3 Characterization of Holographic Surface Reliefs

The first aspect to be discussed in the framework of the present experimental situation is related to the dependence of the surface modulation on the polarization state of the spatially structured illuminating beam. As largely discussed in the previous chapters, one of the well-established key features of the light-induced mass migration in azopolymers is the dependence of the material displacement direction on the polarization state of the illuminating light. The great majority of the reported studies emphasize the role of the light polarization as a parameter for the determination of the material migration direction and efficiency, concluding that an efficient mass transport requires a light electric field component parallel to the intensity gradient direction. In typical mass migration experiments, the intensity pattern is simple and has a defined gradient profile, maintained fixed or spatially confined over the illuminated sample area. This is the case, for example, of the sinusoidal interference patterns used for SRG inscription, or the case of focused gaussian beams inducing focused SR.

In these situations a fixed or symmetric relation exists between the direction of the gradient in the illuminating intensity pattern and the light polarization state (linear or circular). However, if the illuminating intensity pattern is more complex than

sinusoidal, or extended to larger areas than the focal spot of a single gaussian beam, the reciprocal direction of the actual electric field and the intensity gradient direction of the light pattern can vary in different areas of the exposed film, with a position dependence of the inscribing efficiency or even of the mass migration direction [40,41].

Having in mind the holographic complex surface structuring as final goal, it is important to investigate and characterize the surface reliefs arising onto the azopolymer surface under different reciprocal local orientations of the illuminating intensity gradient direction and the direction of the light polarization. As this two degrees of freedom are independently controlled in our CGH illumination setup, eventual non-trivial independent contributions to the mass migration of these parameters could be easily highlighted. This can lead to potential applications not only in the superficial photo-lithography, but can give an unprecedented versatility in the study of the mass migration phenomenon at the fundamental levels [40,41].

3.3.1 Dependence of surface reliefs on linear polarization direction

An appropriate experimental configuration, suitable for the study of the dependence of the surface relief inscription process on the local reciprocal direction of the intensity gradient and light polarization direction, is realized by irradiating the azopolymer film with a linearly polarized beam whose intensity profile has been modulated to achieve light patterns with circular or radial symmetry. In this situation, indeed, all the possible reciprocal angles between the polarization direction and the intensity gradient can be explored in a single step irradiation over a confined region of the sample. Two examples of such radial and circular light patterns are the array of radially distributed lines, and multiple concentric circles. These patterns can be easily constructed as grayscale images by any computer-graphic program (Figure 3.4(a) and Figure 3.4(d)) and can be turned in effective modulated intensity patterns by the CGH technique described above.

Figure 3.4(b-c) and Figure 3.4(e-f) present the AFM images of the surface reliefs produced by the irradiation of the azopolymer film with the holographic intensity patterns presented in Figure 3.4(a) and Figure 3.4(d), respectively. The light polarization direction of the illuminating beam is represented by the red arrows, and is vertical in the images. As can be immediately noted from the topographic color-scale, there is an inversion in the sign, more than a simple reduction in mass migration efficiency, for the surface reliefs generated in different positions of the illumination patterns, i.e. for different relative direction of polarization-intensity gradient. In particular, for the lines in Figure 3.4(b) having the intensity gradient perpendicular to the polarization (vertically oriented lines in the image), the surface relief is an above-

ground groove, resulting from the polymer accumulation in the regions of maximum intensity. On the contrary, for lines presenting the intensity gradient in the direction of the polarization (horizontal lines in the image), the surface relief is a valley produced by the material displacement far from the maximum intensity points along the line.

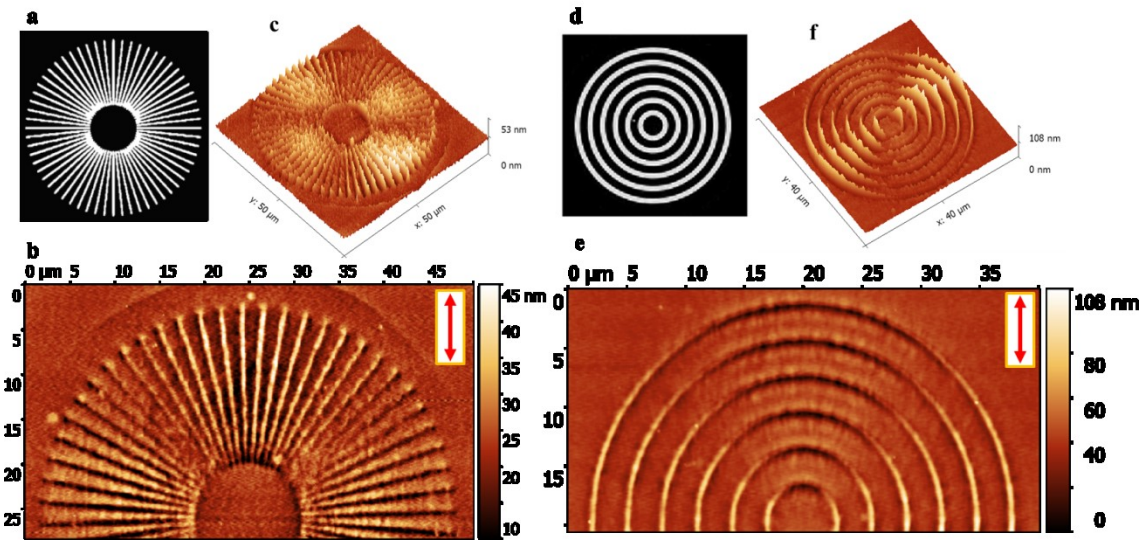

Figure 3.4| Surface reliefs induced onto the azopolymer film with radial and circular intensity patterns. (a) Target intensity image constituted by and array of radial bright lines. (b) Bidimensional and (c) tridimensional AFM images obtained from the film illumination with the pattern (a) by a linearly polarized beam, whose direction is specified by the red arrow. (d)-(e)-(f) same image sequence for the intensity pattern constituted by concentric bright circles.

The lines of the array oriented in intermediate directions are characterized by topographies continuously going from the groove to the valley as the line direction changes from vertical to horizontal. Furthermore, there are also particular directions characterized by almost zero surface modulation occurring at about 40° respect to the light polarization direction. A similar behavior is observed also for surface reliefs obtained with the concentric intensity circles (Figure 3.4(e)), where even a continuous variation in the material displacement direction is observed as the angle between the intensity gradient and the light polarization varies over the irradiated areas. In order to exclude the eventuality that this particular behavior observed in the reliefs might be due to some aberration of the optical setup in the used specific polarization direction, the same experiment was repeated for the radial array of lines with a linear polarization rotated by 90 degrees respect to the previous experiment.

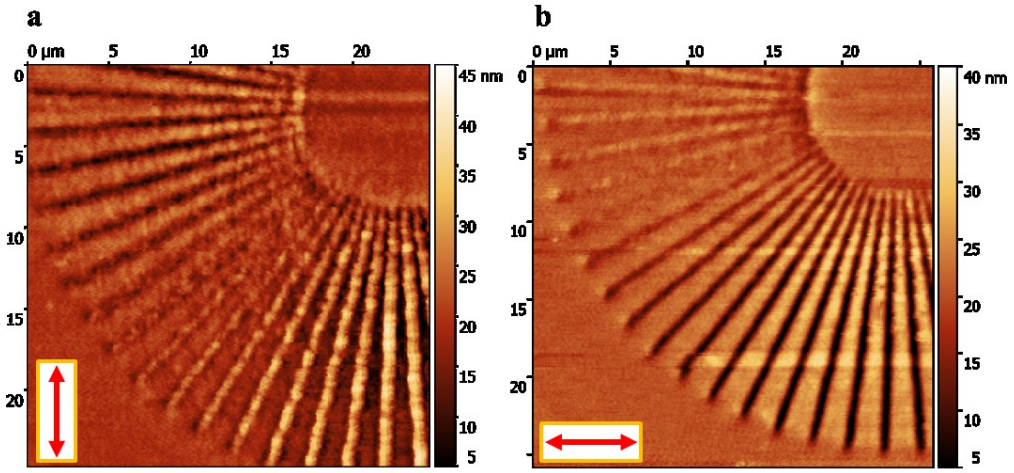

Figure 3.5| Comparison of the surface reliefs resulting from the illumination of the azopolymer film with the radial array of lines for (a) vertical and (b) horizontal linear polarization direction.

In Figure 3.5 the AFM images of the radial array of lines obtained for the two orthogonal linear light polarizations are compared. From the images, a complete inversion of the sign of the surface reliefs is observed as consequence of rotation of the light polarization. This effect reasonably excludes optical aberrations as causes of the observed phenomenon and suggests a real inversion of the mass migration direction as the reciprocal orientation of the intensity-gradient and linear polarization varies along the sample.

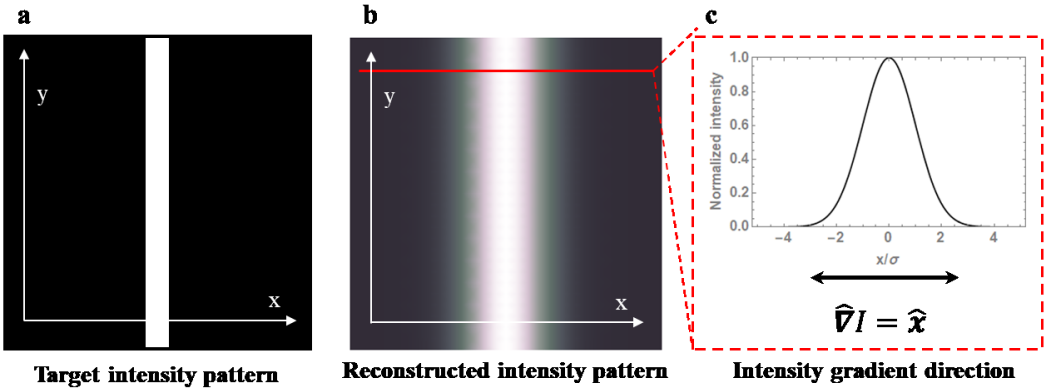

Figure 3.6| Schematic definition of the target intensity pattern and the intensity gradient direction in the experiment with a single bright light as illumination pattern. (a) target intensity, (b) simulated unidimensional Gaussian profile approximating the diffraction limited intensity pattern in objective focal plane. (c) direction of the intensity gradient.

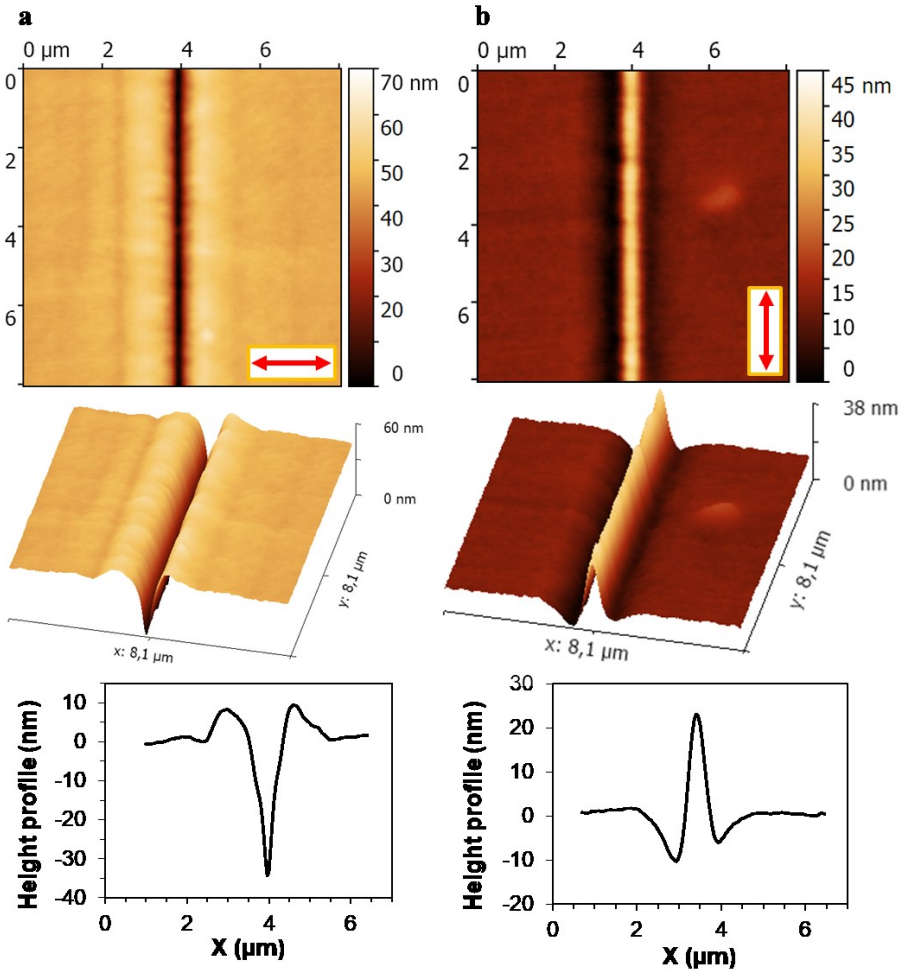

Figure 3.7|Comparison of AFM images and topographic profile of the surface reliefs obtained for (a) linear polarization direction parallel to the intensity gradient direction; (b) for linear polarization orthogonal to the intensity gradient direction.

In order to investigate more accurately the phenomenon in a simpler illumination condition, the surface reliefs arising from the azopolymer illumination with a single unidimensional intensity pattern having a fixed intensity gradient direction, are analyzed more in detail. In this experiment, the intensity pattern used as target for kinoform calculation is the single bright line shown in Figure 3.6(a). Because of the light diffraction, the actual light distribution at the objective focal plane can be approximated to a one dimensional gaussian (Figure 3.6(b)) having an intensity gradient in the x direction of the images (Figure 3.6(c)). Figure 3.7 reports the AFM images, and the relative topographic profiles, of the surface reliefs obtained from the unidimensional intensity pattern for the illuminating beam linearly polarized in the direction *parallel* (Figure 3.7(a)) and *perpendicular* (Figure 3.7(b)) to the intensity gradient.

In the experiments, the beam intensity is maintained fixed at the value of about 1kW/cm^2 and the exposure time is 150s. Accordingly to the observations of the previous experiments, the surface reliefs resulting from the same illumination condition but perpendicular polarization directions in the inscribing beam are characterized by inverted topographies as consequence of opposed directions of the polymer mass migration in the illuminated areas.

The surface relief obtained with light polarized in the horizontal direction has a depth of 34 ± 2 nm (Figure 3.7), while the groove resulting from vertical polarization has a height of 21 ± 2 nm. The amplitude in the case of horizontal direction is about 1.4 times larger than the amplitude of other case, meaning a more efficiency of the mass migration phenomenon when the light polarization direction coincides with the intensity gradient direction. However, a more accurate study of the efficiency of the material movement in the two polarization cases can be conducted by monitoring the surface relief growth as the fluence of the illumination light is variated.

3.3.2 Surface relief growth dynamics under linear polarization

To characterize the growing dynamics of the surface relief formation in the two intensity gradient-polarization conditions, the surface relief inscription with the unidimensional illumination patterns is repeated for different exposure times from 10s to 150 at the fixed intensity of 1kW/cm^2. During these experiments, once the polarization state is chosen, the sample position in the objective focal plane is controlled by a piezoelectric scanner, programmed to translate the sample of a fixed spatial step at each different exposure time. The result of this sample movement is an array of parallel surface reliefs inscribed onto the azopolymer film, each corresponding to a particular value of the exposure time (Figure 3.8). The translation step (8 μm) of the piezo scanner is set to a value large enough to guarantee that each surface relief is not influenced by the successive illumination step. From the topographic profile, measured by the AFM, it is possible to estimate the amplitude and the width (specified as the FWHM of the profile) of the different surface reliefs produced onto the surface as the exposure time is increased. The measurement results, for the two polarization states, are shown in the graphs of Figure 3.8. While the FWHM[3] does not show a particular trend as the exposure time increases, being fixed to values in the range of 350-400 nm, the analysis of the amplitude growth at low exposure times shows a linear behavior in both the

[3] Note that the width of the unidimensional intensity line, imposed by the laser wavelength and objective diffraction limit, is $d = 1.22\frac{\lambda}{2NA} \approx 250\ nm$.

cases. This is highlighted in the graph of Figure 3.9, where a direct comparison of the measured surface relief amplitude is presented.

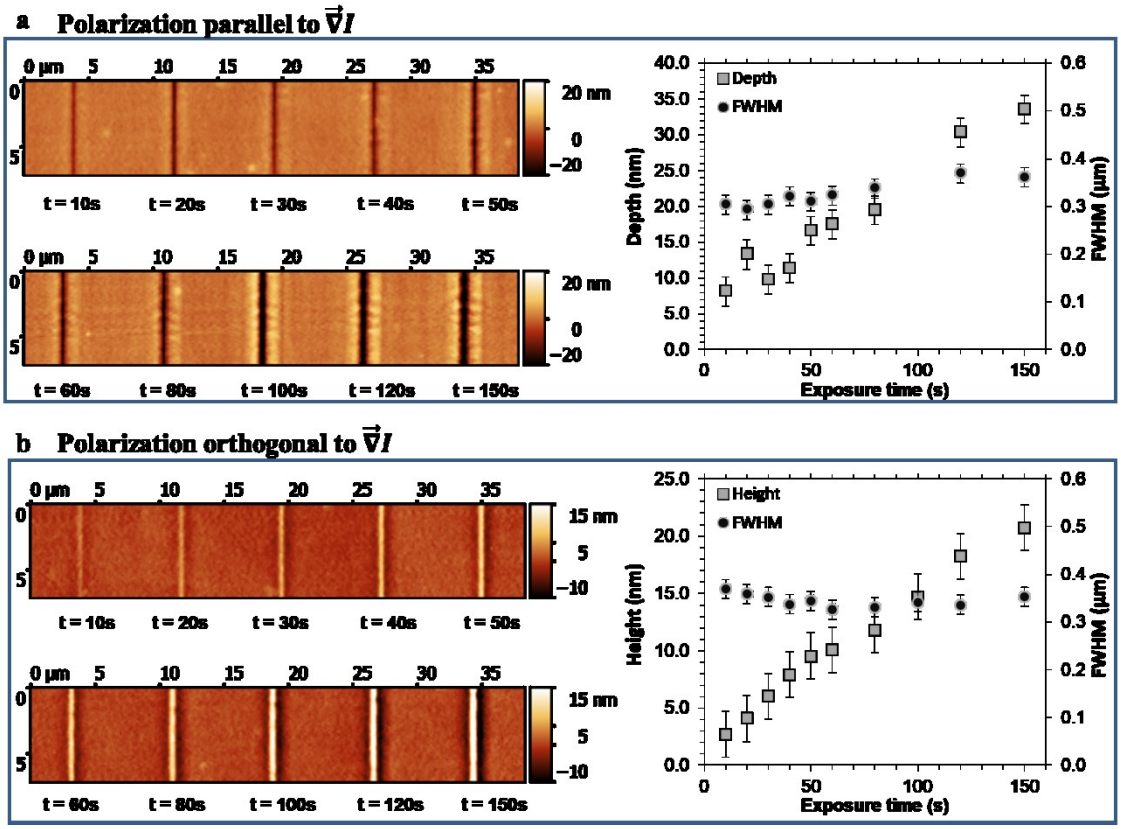

Figure 3.8| Comparison of surface relief growth dynamics for different exposure times at fixed laser intensity for the two investigated polarization states. Each panel shows the AFM images of the array of single lines inscribed with the exposure specified below each structure. The graphs present the plot of the amplitude and the width of the surface reliefs measured from AFM profiles.

The linear fit of the data can be used to characterize the growth velocity. This resulted in the values of (-0.17 ± 0.01) nm/s for the parallel linear polarization direction and (0.16 ± 0.01) nm/s for orthogonal polarization. From this analysis, it emerges that the growing velocities in the two polarization states are comparable in the range of the investigated exposure times. However, in the case of the polarization parallel to the intensity gradient, the surface reliefs at the early stages of the inscription process have significant modulation amplitudes (depth) which translates into an intercept of (-7 ± 2) nm of the linear fit, differently from the case of perpendicular polarization where the estimated intercept is compatible with zero modulation. Such difference implies a better

efficiency of the mass migration process for the parallel polarization configuration in the early irradiation stages, which can justify the lower modulation in terms of absolute amplitude of the groove surface relief respect to the valley shown in Figure 3.7.

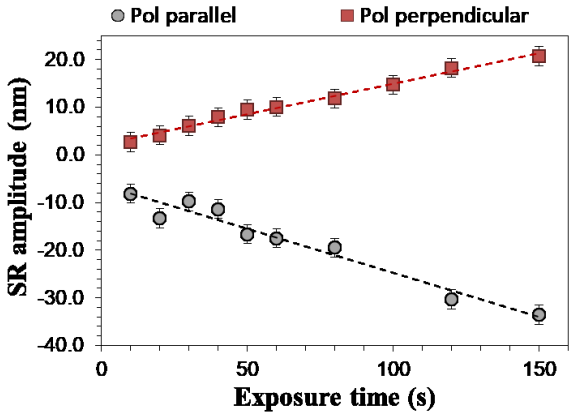

Polarization state	Growth rate (nm/s)
Parallel	-0.17 ± 0.01
Perpendicular	0.16 ± 0.01

Figure 3.9| Comparison of the growing rates of the surface reliefs for the different polarization states. The dashed lines are the linear best fit for the data.

3.3.3 Characterization of surface reliefs with circular polarization

The topographic characterization and the growth dynamics of the surface reliefs arising from the focused unidimensional gaussian intensity pattern under circular polarized light are presented in Figure 3.10. The analysis is conducted in the same experimental conditions as the previous study performed for linear polarizations; namely beam intensity of 1kW/cm^2 and exposure time ranging from 10s to 150s. The AFM image of the unidimensional surface relief at exposure time of 150s and its topographic profile are presented in Figure 3.10(a) and Figure 3.10(b), respectively. These describe the surface relief as characterized by the valley height profile, with a geometry similar to the one obtained with the linear polarization direction parallel to the intensity gradient in Figure 3.7(a).

The amplitude and the width of structures resulting from different exposure times are estimated from the AFM of the line array reported in Figure 3.10(c) and are presented in the graph in Figure 3.10(d). The SR amplitude shows a linear increase at the initial states of the process, with an estimated growth velocity of 0.04 ± 0.01 nm for the relief depth. Compared with the case of linear polarization described in Figure 3.9, the initial growing rate is slower by a factor of about 4. However, the growth behavior becomes non-linear for longer exposure times (more than 60s), as highlighted by the displacement of the measured data from the best linear fit of the initial growing phases

of the process (red dashed line in Figure 3.10(d)), and produces a depth of (26 ± 2) nm at the exposure time of 150s. The width of the structures appears slightly larger than the case of linear polarization, showing a fluctuation around the value FWHM=400nm.

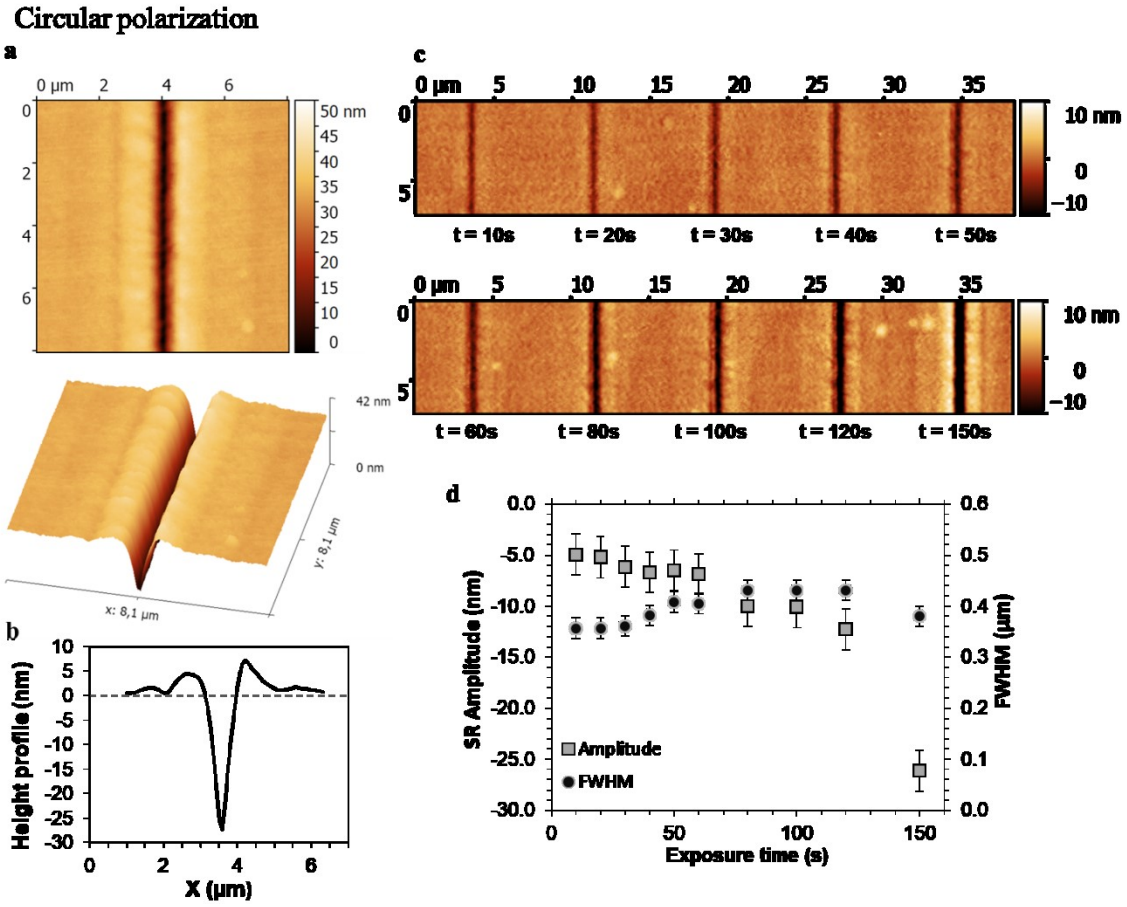

Figure 3.10| Characterization of the holographic unidimensional surface reliefs under circular light polarization. (a) and (b) AFM images and topographic profile of the typical SR obtained in this configuration. (c) AFM images and (d) measured SR amplitude and width of the sequence of SR inscribed onto the azopolymer at different exposure time (exposure intensity 1.0 kW/cm^2).

3.3.4 CGH for fundamental studies about the light-induced mass migration phenomenon

On the basis of the experiments reported many times in literature, one could easily expect, that for illumination situations where the intensity gradient is orthogonal to the

polarization, the mass migration is very inefficient, analogously to the s-s polarization states for the interfering beams in the case of SRGs (see also Figure 1.3).

However, in few recent works, not only SRGs are obtained with the s-s polarization of the interfering beams, but they are also associated to the competition of two distinct mass migration phenomena, driven independently by the intensity gradient and/or by the light polarization, producing each a mass transport in opposite directions [40,41]. While the relative strength of the two proposed driving mechanisms is described to depend on the chemical nature of the host material and on the light intensity, all these studies have been performed by analyzing only the surface relief formation under sinusoidal interference patterns. However, such illumination configuration does not allow the disentanglement of eventual independent polarization/intensity contributions to the mass migration [40], and requires the introduction of more complex illumination configuration, as the use of an assisting-beam [41], in order to extract decoupled information. Furthermore, the possible combinations of light intensity patterns and polarization distributions with the interfering beams configurations are limited and necessarily interlaced [42].

On the other hand, the holographic generated intensity pattern demonstrated here allows a complete disentanglement of the intensity gradient direction and the light polarization state, the latter being tuned by usual waveplates independently from the holographic structured intensity. This has permitted to clearly observe two distinct regimes for the induced mass migration direction [Figure 3.4; Figure 3.5; Figure 3.7], depending on the relative orientation of the polarization and the local direction in the intensity gradient. Furthermore, the comparable growing rate [Figure 3.8; Figure 3.9] observed in the two sets of surface reliefs, inscribed in exactly the same exposure conditions (intensity and exposure time), suggests that the two processes in our highly focused illumination configuration have almost comparable efficiency.

Regarding the circular polarization as superposition of linear combination of the two linear polarizations in the direction of the intensity gradient and its orthogonal direction, the surface reliefs arising under the circular polarized light can be interpreted as the result of the two competitive phenomena leading to the formation of structures shown in Figure 3.7. The observed valley profile obtained in polarization configuration, however, imply a more efficient mass migration when the polarization direction is mainly oriented in the direction of the intensity gradient.

A tentative to rationalize this mass migration inversion phenomenon can be made, following the result obtained by Yang et al. in reference [49], where a more accurate version of the optical gradient force model described in section 1.3 is given. In that theoretical framework, the full electromagnetic force determining the material

displacement is the result of two contributions: a z component (independent on the polarization) pushing down the material and a lateral component whose sign (but not strength) depends on polarization. However, in that experiment, the inversion in the mass migration direction was observed only in the presence of a uniform assisting beam, simultaneously illuminating the film during the inscription process with a unidimensional Gaussian intensity distribution. This assisting beam, according to the author's comments, would only have the role of enhance the photoisomerization of the azochomophores. On the contrary, they observed only a valley surface relief without the presence of an assisting beam regardless the actual polarization direction.

In our focused situation, the light power density is certainly higher respect to the experiments reported there, so that we can assume a more efficient photoisomerization is taking place, without the need of any assisting beam. However, the application of this full optical gradient force model for the description of our experimental situation is not a simple task, because of the complex three-dimensional distribution of the focused optical fields (and hence of the eventual optical forces acting onto the azopolymer film) in the focal plane of the microscope objective and of the necessity to include them in a complex description of the material dynamics through the solution of the Navier-Stokes equations.

Also in this case, however, the phenomenological model exposed in the previous chapter [8,10,46] seems to be the most promising theoretical framework able to explain the polarization-dependent mass migration inversion. Indeed, by phenomenologically choosing the signs of the coefficients in the mass current in equation (2.20), two directions for the light-induced surface modulation are possible. Furthermore, the model involves also the non-trivial coupling of the optical field components with the azopolymer surfaces, which could play a non-negligible role in our experimental situation. This eventuality, is not taken into account in any other model, included the full optical gradient force model. It should be noted, however, that the material chemistry is expected to play a role in determining the inversion behavior [40,41], so that a more accurate investigation should involve the investigation of this behavior in different azomaterials.

The considerations exposed here show the potentialities that this illumination approach can have in the future studies on the mass migration phenomenon at the fundamental level. Furthermore, in the remaining sections of the present chapter the ability of the CGH illumination to induce complex superficial textures is also presented. The results obtained make our illumination configurations suitable in micro-nano photo-lithography applications.

3.4 Holographic nano-lithography in azopolymers

In the light of the analysis conducted in the previous section about the polarization dependence of the focused holographic SRs, one immediately recognizes that the use of linearly polarized light is not suitable to inscribe uniform surface modulations from illumination patterns more complex than simple lines having fixed directions over the azopolymer surface. This can be already understood from the surface reliefs reported in Figure 3.4, but it becomes even more evident for the holographic intensity pattern reported in Figure 3.11. Despite the reconstructed holographic intensity (not shown here) in the polymer plane is very similar to the target intensity pattern, the resulting surface relief is deformed as consequence of the differences in the local mass migration behavior resulting from the reciprocal direction of the local intensity gradient and the polarization direction.

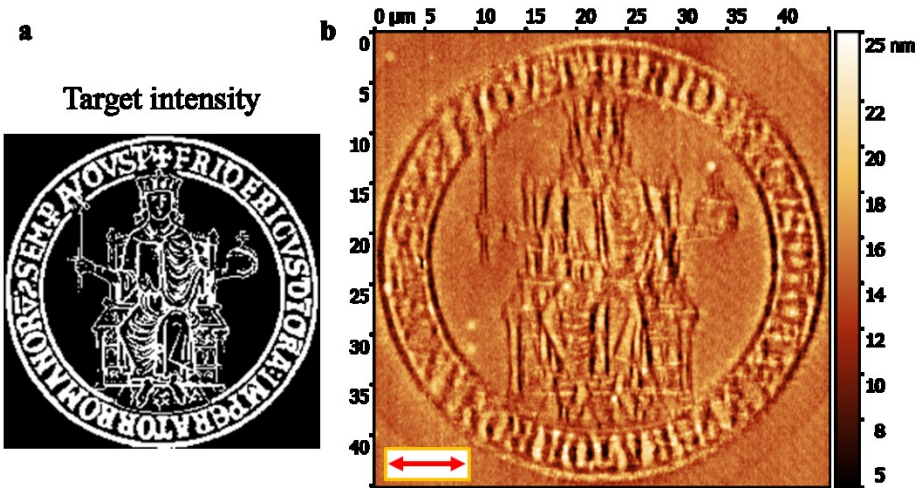

Figure 3.11| Complex surface relief arising under linear light polarization. (a) Target intensity pattern constituted by the logo of University Federico II. (b) AFM image of the inscribed surface relief. The red arrow indicates the polarization direction of the beam during the experiment.

However, the use of circular polarization allows to solve this directional dependence, leading surface reliefs of the type described in Figure 3.10(a), homogeneously inscribed in the illuminated regions of azopolymer film, regardless to actual intensity distribution of the holographic light pattern. This behavior is clearly demonstrated by the surface reliefs obtained from circular and radial symmetric intensity profiles under circular polarized light show in Figure 3.12.

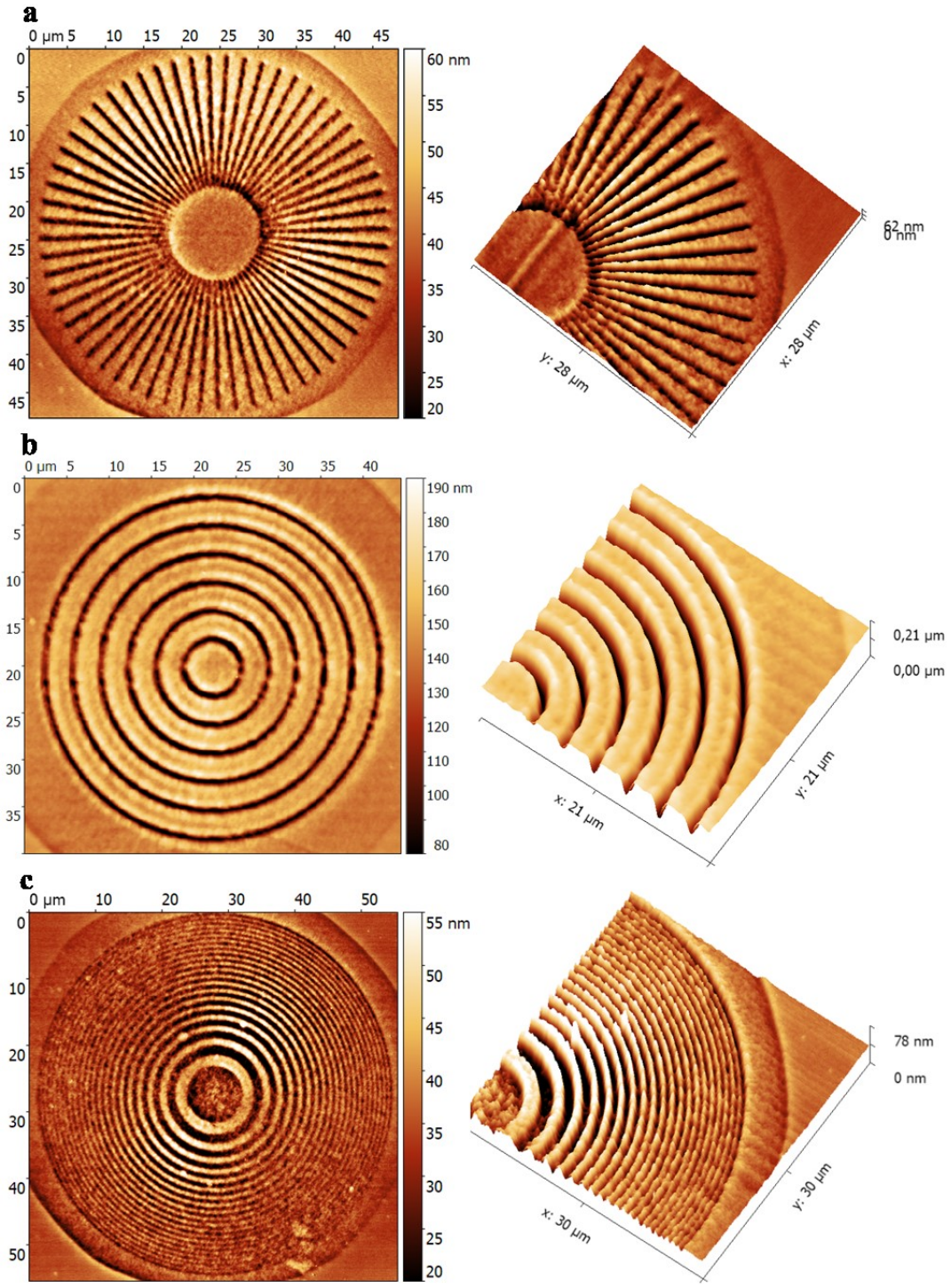

Figure 3.12| AFM images (and 3D zoomed view of sample regions) of circular and radial symmetric surface reliefs obtained from holographic intensity patterns and circular light polarization. (a) Array of radial lines. (b) Array of concentric circles. (d) Surface modulations reproducing the transmittance of a Fresnel lens.

The array of radial lines in Figure 3.12(a) and the concentric circles in Figure 3.12(b) can be directly compared with the surface reliefs in Figure 3.4, obtained from the same holographic intensity pattern but with linear light polarization. In this latter case, there was an alternation of the groove and the valley profiles, depending on the particular angular position of the line in the array of radial lines, or on the direction of the local tangent to the circles in the array of concentric circles. This anisotropy, instead, disappears completely in the case circular polarization, which is characterized by the valley profile independently of the angular position or the direction of the tangent in the intensity patterns. A closer look at the surface reliefs shows the presence of a particular direction where the mass migration resulted less efficient respect to the surrounding. This can be ascribed to a slight residual ellipticity in the polarization due to the not perfect conversion of the linear polarized light into the circular by means of the quarter-waveplate. Furthermore, this effect highlights again the very high sensitivity of the surface reliefs inscription efficiency in the present experimental configuration, suggesting the use of this phenomenon as a topographic method of recording the vectorial configuration in the optical field, as proposed many times in the literature over the years [4]

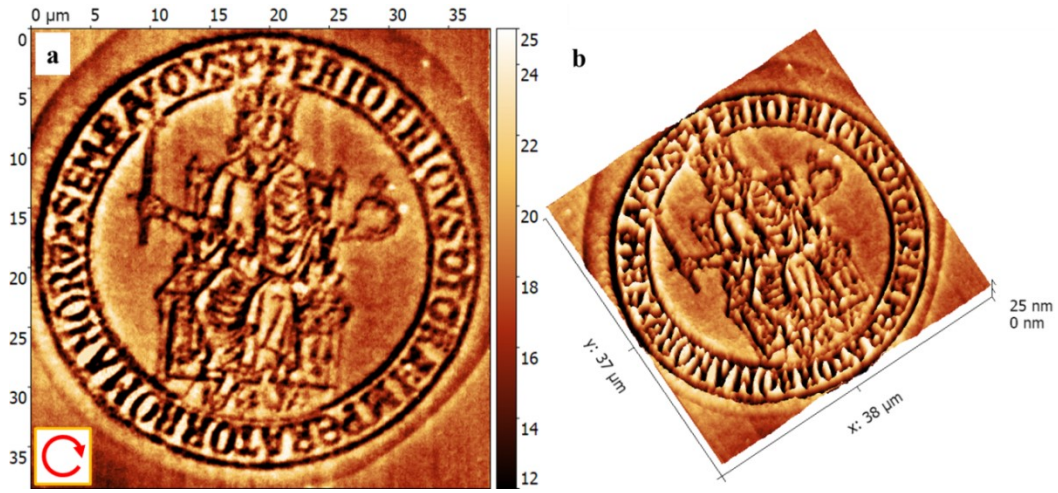

Figure 3.13| AFM image of the surface relief figuring the University logo. The surface modulation is obtained in the same intensity and exposure conditions of Figure 3.11, but with circular polarized light.

Besides the demonstration of the isotropic mass migration, the reliefs in Figure 3.12, are also the first demonstration to my knowledge, of good quality circular surface reliefs [4], even if restricted onto a small sample area ($50 \times 50\ \mu m^2$). For this circular

surface relief geometry, the holographic setup allows the inscription of even more complex circular surface profiles, as the one of a Fresnel lens shown as an example in Figure 3.12(c), which could be employed in some photonic applications.

Even the complex intensity pattern figuring the logo of University Federico II (Figure 3.11(a)) is transferred in a homogenous surface relief by the use of circular polarized light(Figure 3.13).

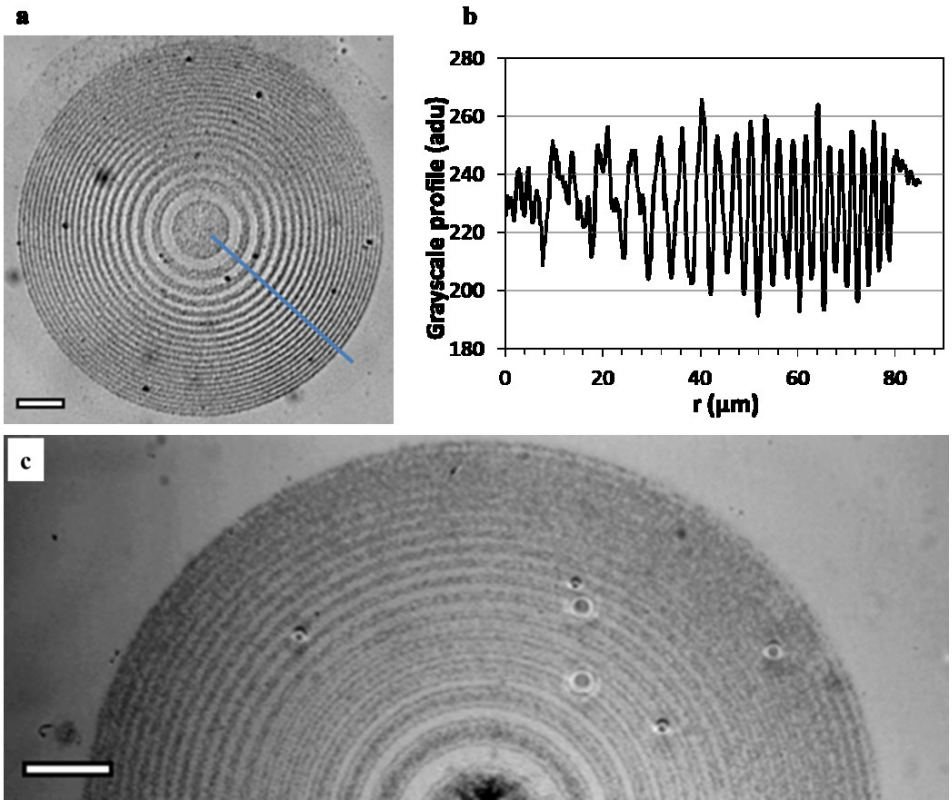

Figure 3.14| Scalability of the holographic surface reliefs.(a) Optical image of the Fresnel lens surface reliefs inscribed with a 40x objective (scalebar 5um). (b) Grayscale profile traced along the blue line in panel (a). (c) Optical image of the Fresnel pattern inscribed onto the azopolymer with a 10X objective (scalebar 200um).

The superficial structures presented in this paragraph represent a clear demonstration of the potentialities of the holographic controlled illumination of the azopolymer films for the inscription of nanometric superficial features (amplitude modulation in the range from few nanometers to about 100 nm) with a sub-micron (400 µm) spatial resolution onto an area delimitated by the objective lens field of view. This last aspect can be tuned in order to scale the inscribed structures over different lateral

dimensions. A qualitative example is show by the optical images of the surface reliefs in Figure 3.14, where the holographic Fresnel intensity profile is projected onto the azopolymer film at different optical magnification. In particular the surface relief in Figure 3.14(a) is obtained with a 40X objective (NA=0.65) and extents over an area of more than $170 \times 170\ um^2$, while the surface relief in presented in Figure 3.14(c), obtained with a 10X objective (NA=0.25) is even extended in the millimeter scale.

3.4.1 Surface reliefs from multistep illumination

Another typical peculiar effect observed in the light-induced mass migration phenomenon in azomaterials is the material response to different sequential illumination steps. This phenomenon has been demonstrated to allow the cyclical inscription/erasure of light-induce surface reliefs (see for example section 4.2.7 and [5,11]), and the inscription of complex or hierarchical superficial textures [78].

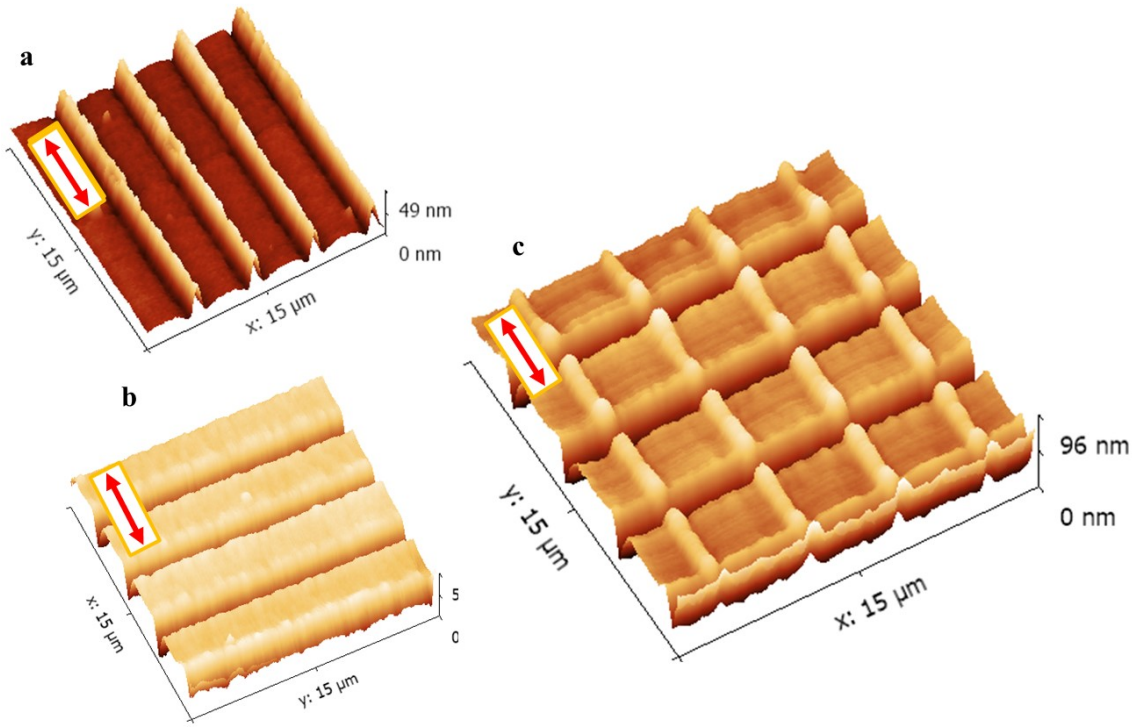

Figure 3.15| Sequential inscription of parallel lines oriented in perpendicular directions for a linear polarization state. (a) and (b) AFM images of the surface relief obtained after one step of illumination. (c) AFM of the composite surface relief resulting from the sequential illumination with the two arrays of orthogonal lines.

Such multistep illumination process can be used is analogous way also in the holographic polymer structuration presented here, adding a further degree of control of the resulting surface reliefs. The proof of the effectiveness in the multistep surface structuration is presented in Figure 3.15 and Figure 3.16, where a simple array of parallel lines is used as a prototype of structured illumination intensity pattern. The sample exposure consisted of two distinct illumination steps, in which the polarization direction is maintained fixed (linear in the case of Figure 3.15 and circular in the case of Figure 3.16), while the intensity pattern is rotated by 90° by using the same rotation for the holographic target intensity pattern in the CGH calculation.

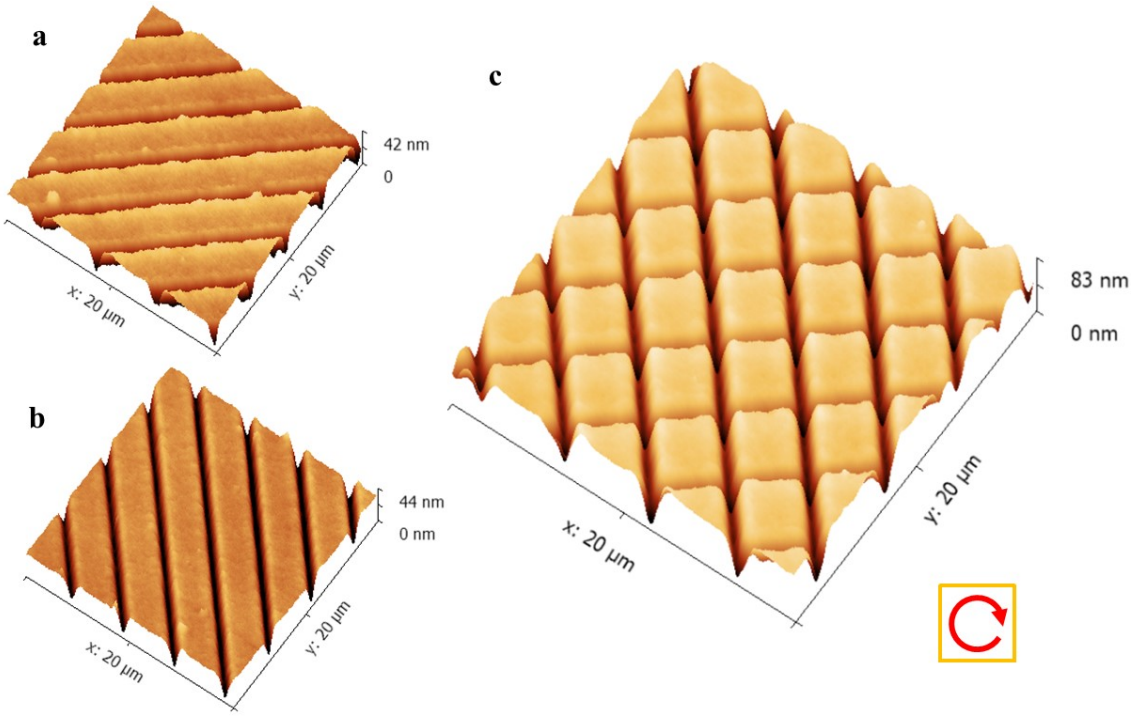

Figure 3.16| Sequential inscription of parallel lines oriented in perpendicular directions for a circular polarization. (a) and (b) AFM images of the surface relief obtained after one step of illumination. (c) AFM of the composite surface relief resulting from the sequential illumination with the two arrays of orthogonal lines.

While each individual illumination step produces surface reliefs having topographic features already discussed above is this chapter (Figure 3.15(a-b) and Figure 3.16(c)), the sequential two-step produce hierarchical surface reliefs, where each of the illumination step contributes with its own topographic characteristics, and the results are a grid of valley and grooves in the case of linear polarization or an array of nano-pillars

in the case of circular polarization. Furthermore, in these simple experiments no particular dependence on the order of the actual illumination steps has been found to affect the final structures.

It is worth noting that the presented illumination schemes are very simple and the final surface reliefs can be obtained easily in a single step illumination by a proper calculated hologram, however it is possible to imagine situations where this one-step structuration is not possible. The presented simple experiments demonstrate, however, the possibility to use successfully such sequential structuration method, which adds another dowel in the potential applications of the holographic structured azopolymer surfaces in micro/nano-lithography.

4 Large-scale single-beam photo-patterning of azopolymer surfaces

In the previous chapter we have exploited a novel holographic illumination approach able to inscribe complex nanometric modulation onto the surface of the azomaterials. Even if the scalability of the process to large areas has been qualitatively demonstrated as possible, the holographic setup reaches its best performances in terms of quality of inscribed structures in a focused illumination scheme. This requires in general a quite sophisticated and relatively expensive optical setup if compared, for example, with the simple interfering light beam configuration needed to inscribe the SRG on a large area. Many applications, especially in the field of photonics, necessitate both complexity in the superficial texture and large scale patterning [3,4]. In the best light-driven fabrication technique one can imagine, both these tasks should be achievable with a simple optical configuration and even in a single step illumination step. Using the azomaterial as lithographic platform, the simplest large-scale illumination condition conceivable is the irradiation of an azomaterial film with a simple single beam. On the basis of the discussions about the light-induced mass migration phenomenon conducted in the previous chapter it is difficult to imagine how this extremely simple illumination condition can give rise to some superficial modulation. However, surprisingly, this actually happens and the surfaces develops spontaneous periodic modulations, similar to the SRG in the case of linearly polarized light, extended over the whole illuminated area [22]. Despite the attractiveness of such single step large-scale photo-patterning, the possible superficial textures obtainable with this approach are limited to unidimensional or hexagonal periodic patterns. Furthermore, analogously to the standard SRG, their amplitude modulation is always restricted to few hundred of nanometers, which means that they can be considered as bidimensional in many situations.

In the last few years, a new approach making use of the light-induced mass migration phenomenon in azomaterials is acquiring more and more relevance for the fabrication of complex three-dimensional superficial architectures. This is based on the light-driven reconfiguration of micro-volumes of azomaterials pre-patterned onto the

surface [3,23,79]. There are many advantages of using such fabrication technique, mainly related to the versatility of the possible obtainable textures and the dramatic reduction of the costs compared to standard lithographic techniques. In this chapter are described the both the superficial textures obtainable onto the azomaterial surfaces single illumination beam. In particular it is first briefly described the spontaneous self-patterning phenomenon of a plane surface of an azomaterial film and then a more detailed presentation of both the fabrication steps necessary to pre-pattern the azopolymer surfaces and the range of possible three-dimensional architectures produced by the light-driven reconfiguration process is given. Furthermore, the deterministic nature of the resultant light-reconfigured micro-structures is highlighted by the agreement between the experimentally observed textures and the ones predicted by the phenomenological model described in chapter 2 [10]. As we will see in the next chapter, the three-dimensional micro-structures fabricated here can be used to tailor with great precision the wetting state of these pre-patterned surfaces [12].

4.1 Spontaneous Surface Relief Gratings

In 2002 Huber et. al found a surprisingly spontaneous appearance of superficial modulations onto the free surface of an azomaterial illuminated by a coherent laser beam having a wavelength in the azomolecule absorption band at normal incidence [22]. In that study, the authors recognized that the light-induced superficial structures, constituted by a two-dimensional array of nanometric protrusions ordered in a hexagonal array, develops directionally following the light polarization direction, suggesting this *superficial spontaneous patterning* being related to the light induced mass migration phenomenon. Then, many studies have been oriented toward the rationalization of the phenomenon because of the great interest in the fabrication opportunities offered by this simple one-step illumination process [9,20,80–85].

In order to describe the main features of the self-structuring phenomenon and to give an insight in the commonly accepted optical feedback mechanism explaining the rising of this spontaneous structuration, the surface modulations obtained onto our azopolymer (see Appendix A) under irradiation with a single polarized beam are shown in Figure 4.1. In the experiment, the direction of the linear polarized laser beam at $\lambda = 488\,nm$ is chosen alternatively in two orthogonal directions by a half-waveplate, positioned right before a cylindrical lens of focal length 75 mm. This lens projects the beam onto the azopolymer film, which is positioned in its focal plane. The spot in the sample plane has an elliptic profile, with minimum width of 100 μm and length of about

2 mm (Figure 4.1(a)). The AFM images of the spontaneous surface reliefs, obtained upon 1h irradiation time with a laser power of 0.870 mW for the two orthogonal polarization directions, are shown in Figure 4.1(b) and Figure 4.1(e), respectively. A zoomed view of the structures is also presented in Figure 4.1(d) and Figure 4.1(g).

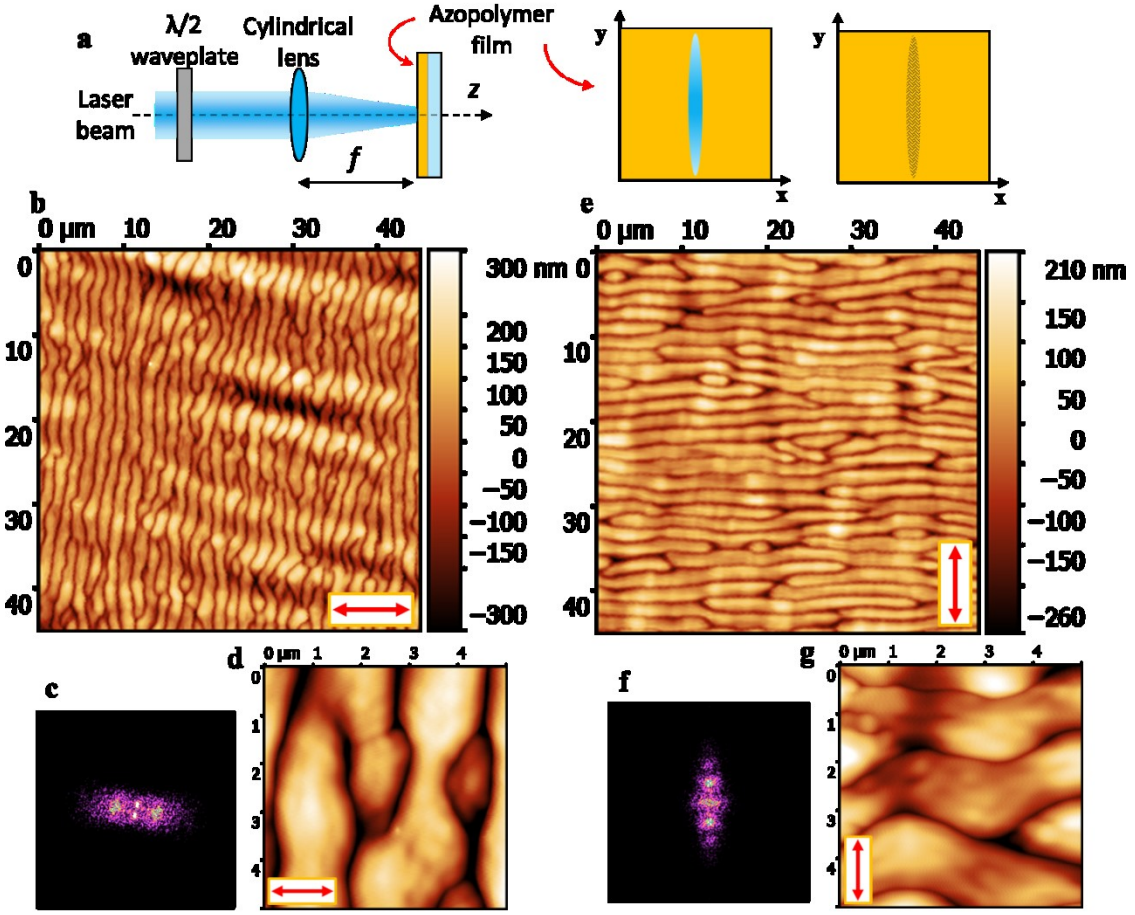

Figure 4.1| Spontaneous surface relief grating induced by the illumination with a single beam. (a) Schematic representation of the experimental configuration for the illumination and the elliptic spot generated by the cylindrical lens onto the sample. (b)-(c) AFM image and its Fourier transform for the structures obtained for horizontal polarization. (e)-(f) Same images for vertical polarization. (d) and (g) zoomed views of regions of the images (b) and (e) respectively.

From these images it results evident that the surface develops a grating-like modulation with amplitude of several hundreds of nanometers. Moreover, the grating vector is oriented in the light polarization direction. The directionality of the structures is also highlighted by the wave-vector components appearing in the Fourier transform images calculated from the AFM images (Figure 4.1(c) and Figure 4.1(f)). Here we can

observe Fourier components restricted to a small unidirectional region of the Fourier space meaning approximate unidirectional alignment of the features present in the AFM images. Obviously, the direction of the Fourier wave-vectors is rotated by 90° degrees in the two images, following the rotation of the polarization of the irradiating beam.

The grating-like structures manifest a great similarity with the standard surface relief gratings inscribed onto the azomaterial films under the two-beam interference irradiation. However, in the single beam experiment investigated here, no interference is present in the illumination pattern and the structures arise from some self-organizing material mechanism fueled by the light irradiation. For this reason, the superficial structures obtained by this spontaneous structuring process are commonly referred as *Spontaneous Surface Relief Gratings* (SSRG).

Since the first observations, the SSRG have been paragoned to another spontaneous periodic structure formation process, commonly observed at the surface of most kind of solids illuminated by a continuous or a pulsed laser beams [86,87]. This phenomenon is referred as laser-induced surface structuring (LIPSS). It is observed when a material surface is irradiated at non-normal incidence. Over the surface, an interference pattern is generated during the irradiation between the incident beam and the light scattered by the surface roughness or defects. This interference causes a spatially varying interference intensity pattern and a related spatially distribution of absorbed light energy from the sample which leads to the surface melting in specific regions. However, many of the predictions of a model based onto the LIPSS mechanism are not in agreement with many aspects the experimentally observed SSRG [82]. Furthermore, the high light power needed to induce LIPSS is incompatible with the very low intensity at which the SSRG inscription process occurs, ruling out this thermal process as cause of the SSRG formation in azopolymers.

On the contrary, the self-structuring process seems to be ascribable to the same light-induced mass migration process, typically observable when the illumination light pattern has a spatially modulated field distribution over the azomaterial film (as in the case of SRG). The commonly accepted formation mechanism for the SSRG is related to a feedback effect induced by the interference of the primary illumination beam with secondary waves of scattered light coming from the surface roughness [82,83]. At the very beginning of the illumination process, the light scattered by some defects onto the surface induces a local interference with the primary beam which causes the increase of the superficial roughness around the defect (this effect is sometimes named as nucleation) [9,84,85,88]. As the illumination proceeds, a significant amount of the incident light can be coupled inside the polymer film, which acts as a slab waveguide. This coupling gives rise to two counter-propagating light modes which interfere and

sustain the spatially varying field distribution necessary for the SSRG growth [83] in a spontaneous feedback mechanism.

While the spontaneous feedback mechanism is able to take into account for the spontaneous formation of the surface modulation onto the azomaterial free surface, analogously to the great part of the phenomenological mass migration models, it does not relate the observed macroscopic phenomenon to specific mechanism at microscopic scale. Based on the study of the SSRG formation mechanism, an interesting new idea has been developed recently which could shine some light onto the microscopic mechanism of the SSRG formation and, in principle, onto the whole phenomenon of the light induced mass migration in azomaterial.

In reference [19], the spontaneous pattern formation is ascribed entirely to a phase separation of two immiscible phases in the polymer during the irradiation. These two phases are the two distinct molecular states represented by the cis and trans isomers, which tend to aggregate giving rise to a mass migration. The results predicted by this model are in good agreement with the experimental observations, especially in the case of polymer irradiation with a coherent un-polarized light beam, which gives rise to isolated nanometric protrusions (instead of the grooved pattern shown in Figure 4.1 for the case of linear polarized light) disposed in an hexagonal arrangement. However, a fundamental study about the experimental verification of the phase-separation process supposed to be at the basis of the molecular material rearrangement under irradiation is needed. Such investigation could be performed, for example, using some scanning probe spectroscopic technique able to test, with nanometric resolution, the chemical composition of material in correspondence of the different positions over the sample. A good candidate for such study could be the recently developed Photo-induced Force Microscopy (PiFM) by A. Ambrosio et al [89], which is sensitive to the local differences in the refraction index.

However, besides the understanding of the actual molecular formation mechanism, the spontaneous self-patterning of the azomaterials under the irradiation of single coherent light beam represents a very attractive surface structuring approach for applications where a large scale periodic patterning is required. Typical examples can be the use of this periodic structures in photonics [4] as diffraction gratings or in biology as scaffolds for cell network [14,90]. Even if the SSRG loose some of the structuring control characterizing the SRG obtained with interfering beams, they retain a good degree of interest also because of the very simple illumination configuration, constituted by a single beam configuration. This is accompanied by advantages related to the stability in the inscription process and the easiness of the whole structuring process. As we will see in the next section, the advantages related to the use of a single

beam illumination are retained also in the light-induced reconfiguration of arrays of isolated azopolymer microstructures. In that case, moreover, the range of possible superficial geometries and related applications are even much wider.

4.2 Reconfiguration of pre-patterned azopolymer surfaces

4.2.1 From 1D-2D textures to light-controlled 3D architectures

Until now we have presented several experimental situations in which the light-induced mass migration is used to modulate the surface of azomaterials in form of thin films. However, leaving out the complex surface reliefs produced by the CGH illumination approach presented in chapter 0, demonstrated in all its possibilities for the first time in this present thesis, all the reported superficial textures rely on periodic 1D (SRG and SSRG) or highly confined structures (focused SR). Over the years many approaches have been proposed in order to enlarge the range of superficial textures achievable by the photo-driven mass migration in azomaterials. Just to give some examples, even remaining in the framework of the mentioned simple illumination schemes, two-dimensional patterned surfaces having more complex textures can be easily obtained by multi-beam interference, multi-step illumination and sample/beam scanning approaches.

An example of multi-beam superficial structuring is shown in Figure 4.2, where the surface reliefs obtained onto our azopolymer film by the irradiation of the intensity pattern produced in the interference of three coplanar beams are presented [3,91–93]. The representation of the optical configuration scheme used in the experiment is shown in Figure 4.2(a). The primary laser beam at $\lambda = 488$ nm is divided in three different beams (indicated with the numbers 1-2-3 in Figure 4.2(a)) by two subsequent beam splitters. The mirrors M_1 and M_3 deflect the beams 1 and 3, at the angles θ_1 and θ_2 in such way the rejoin the un-deflected beam 2 in the azopolymer film plane, where they interfere and give rise to the surface relief grating inscription (Figure 4.2(a)). In the specific experiment reported here, the p-polarized beams have a diameter of approximately 3 mm, the incident angles are $\theta_{12} \approx 9°$ and $\theta_{23} \approx 16°$, while the light powers of the beams are P_1=0.81 mW, P_2=0.93 mW, P_3=0.78 mW.

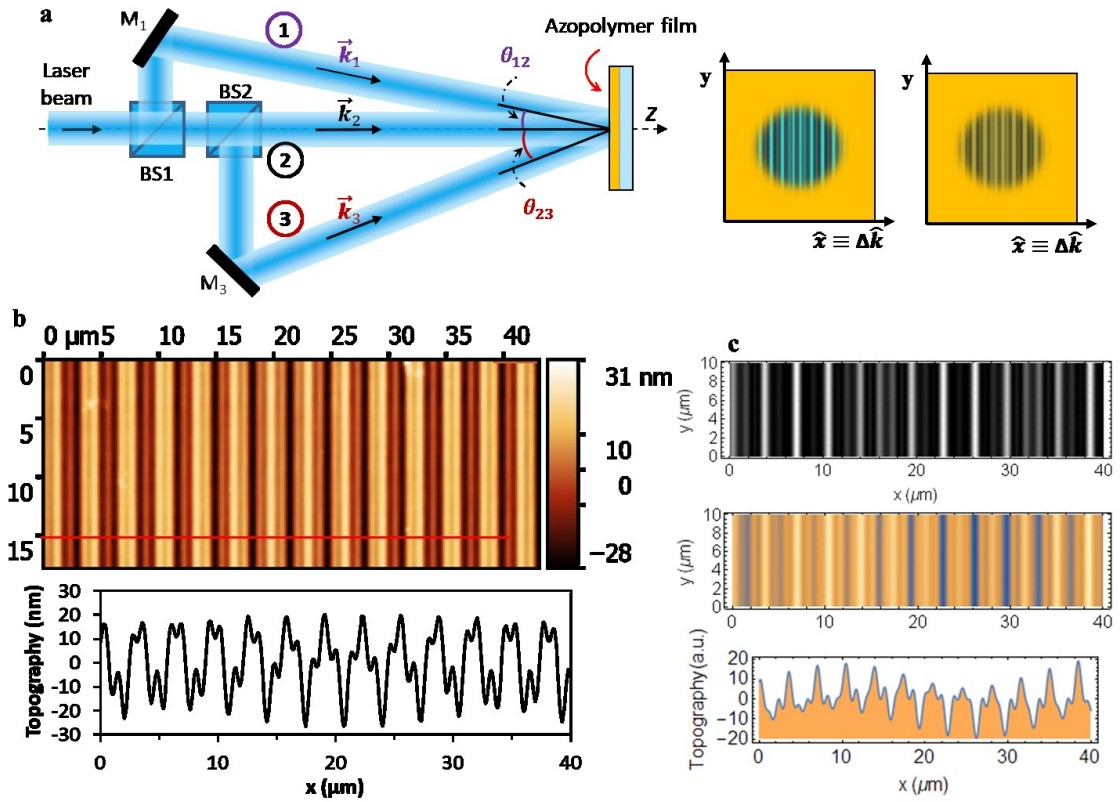

Figure 4.2| Three-beams interference illumination for surface relief inscription. (a) Schematic representation of the optical setup used for generation of the interference intensity pattern. (b) AFM image and topographic profile (traced along the red line) of the obtained surface reliefs. (c) Simulated intensity interference pattern (top) calculated for the actual experimental beam configuration ,;(middle) surface reliefs predicted by the optical gradient force model with the simulate intensity pattern; (bottom) height profile of the simulated surface reliefs.

The AFM image and the topographic profile of the surface reliefs obtained under the azopolymer exposure time of 30 min in these conditions are presented in Figure 4.2(b). Clearly the surface reliefs produced here are still characterized by 1D periodic surface modulations as in the case of standard SRG, however their profile is much more complicated. Changing the incidence angle and the power balance between the three-beams can also produce different periodicities, relative height variations and also bidimensional patterns if the three wavectors are not coplanar. Naturally, the interference pattern can be exactly calculated and the resulting surface reliefs can be qualitatively predicted also by simple mass migration models. In Figure 4.2(c) are shown the calculated interference pattern for the actual experimental three-beam configuration and the surface relief grating predicted by the simple optical force

gradient model (described in section 1.3) which qualitatively agrees with the observed structures of Figure 4.2(b).

The same experimental configuration in the three-beams illumination can be used also to give a simple example of superficial structures obtained from the sequential illumination of the azopolymer film with different interference patterns. Indeed, by blocking alternatively one of the three beams, we can easily obtain three sinusoidal interference patterns having different periodicities. Figure 4.3(a) shows the AFM images and topographic profile of the surface reliefs obtained by a three step illumination process with the sequential irradiation produced by the interference of beams 1+2 (step 1), beams 2+3(step 2) and beams 1+3 (step 3). The irradiation time is 1 h at the beam powers described above for each of the three illumination steps. The images in Figure 4.3(b) are instead the results of the interference illumination sequence with the beams 1+3 (first step), 2+3 (second step) 1+2 (step 3), at the exposure time of 30 min for each step. Besides a slightly different height in the surface reliefs obtained in the two sequences due to a different total exposure time, we can easily observe different profiles of the periodic structures inscribed onto the polymer. These structures cannot be explained easily with simple mass migration models because the successive illumination steps involve an already patterned surface which can induce a non-trivial coupling of the light in the wave-guiding film.

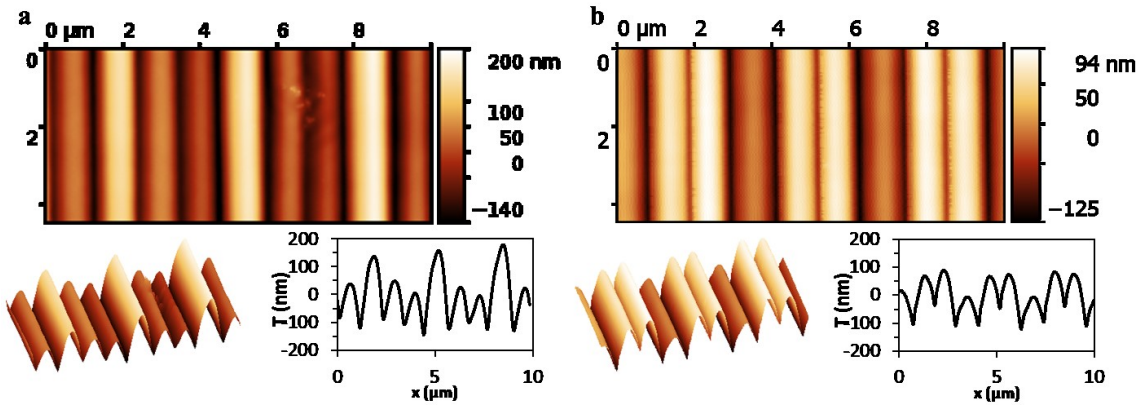

Figure 4.3| Surface reliefs from sequential interference pattern irradiation. The surface reliefs are obtained in a three illumination steps, where only two of the three beams described in Figure 4.2(a) interfere in the azopolymer plane. (b) Surface reliefs obtained for the interference sequence: beams 1+2 (step 1), beams 2+3(step 2) and beams 1+3 (step 3). (b) Surface reliefs obtained for the interference sequence: beams 1+3 (first step), beams 2+3 (second step) and beams 1+2 (step 3).

The experiment described here is just an exemplifying situation where the multi-step illumination can be used to photo-induce more complex textures onto the azopolymer surfaces, however using this approach more complex bidimensional periodic texture can be easily obtained [3,91,94]. However, with this approach more complex is the texture one would obtain, more complex becomes the illumination process needed for it. This complexity affects the ability in the deterministic prediction on the superficial texture obtained at the end of the inscription process, which moreover remain restricted to a two-dimensional pattern characterized by a submicron surface modulation.

A complete different approach for the induction of complex superficial textures onto the azomaterial surfaces is instead based onto the light-reconfiguration of controlled pre-structured surfaces. This method allows drastic simplification of the illumination configuration, with can be essentially constituted by a simple single homogenous beam, and the simultaneous enlargement of the range of the achievable surface geometries, even in three dimensions.

The basic principle of this approach is schematized in Figure 4.4. It consists in the preparation of simple pre-structured micro-volumes of the azomaterial which can be then reconfigured by the mass migration phenomenon occurring under light irradiation. All the peculiar photo-responses of the mass migration observed in the azomaterials in form of thin films are obviously preserved also in this case, so that the material motion is dependent on the light intensity and polarization. Figure 4.4(a) presents schematically the reconfiguration process of a material micro-volume having an initial rectangular section induced by a light beam linearly polarized in the direction orthogonal to structure (red arrow in the image). As the irradiation proceeds, the material starts to move in the polarization direction as result of the azobenzene-driven photo-response. This causes a structural reconfiguration of the pre-patterned architecture as the mass migration gradually involves different layers of the micro-volume, which finally become elongated in the direction of the light polarization. Such phenomenon resembles the thermally induces photofluidic motion used in *Self-Perfection by Liquefaction* (SPEL) [95] lithographic techniques to smooth the edges and the imperfections of micro and nano structures. Because of this phenomenological similarity, the light-induced reconfiguration of the isolated azomaterial microstructures is also commonly referred as *directional light-induced photo-fluidization* [3]. However the directional nature of the mass migration in azomaterials is drastically different from SPEL, which, being a thermal effect, gives rise always to isotropic material motion.

If the azomaterial pre-pattered texture is constituted by a two dimensional array of microstructures (as schematized in Figure 4.4(b)), then the material displacement can be

oriented in all the directions of the sample plane simply by rotating the polarization direction. This, together with the possibility of choosing the actual shape of the pre-patterned structure, gives a very high degree of control on the shapes and orientation of superficial textures, where a controlled anisotropic can be induced by simply tuning the illumination parameters. In the very last years, many experimental situations where the light-induced micro-volume reconfiguration is used to produce complex three-dimensional structures have been proposed. These include the reconfiguration of well-defined geometrical structures (cylindrical, cubic, parallelepiped) [10,11,23,78,79,96], colloidal agglomerates [97,98], or also more complex two dimensional patterns [99,100].

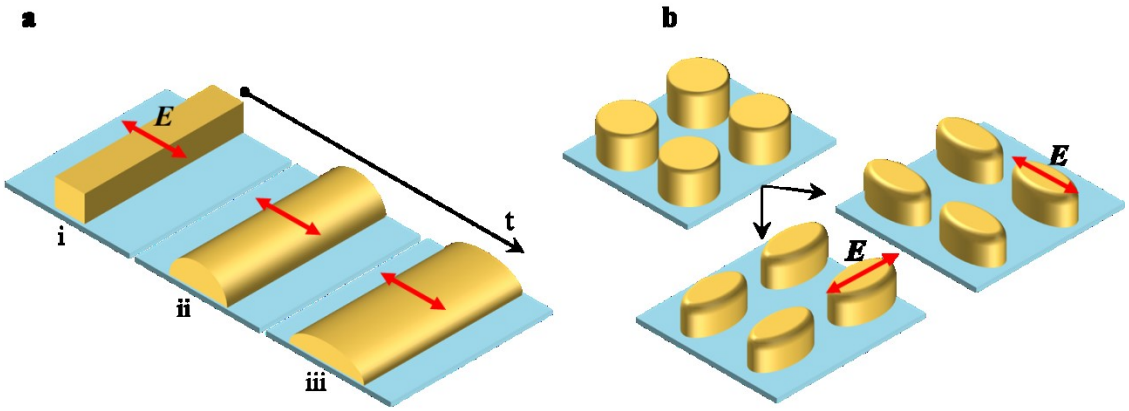

Figure 4.4| Principle of the mass-migration and surface pre-patterning coupling. (a) Schematic representation of the light-driven reconfiguration of an azopolymer micro-volume pre patterned in one dimension. (b) Schematic representation of the dependence of the reconfiguration process in 2D pre-patterned volumes on the polarization state of the illuminating light.

With the aim of producing complex anisotropic three-dimensional textures onto the surface of the azopolymer, we directed our studies concerning this aspect of the mass migration toward the characterization of the three-dimensional architectures obtained by the light-driven reconfiguration of an array of pristine cylindrical micro-pillars. In the next section of the present chapter are described many of the aspects related to the surface pre-patterning processes, the typical micro-architectures obtained in different illumination conditions. Furthermore, the description of the reconfiguration process in terms of the phenomenological mass migration model diffusely discussed in chapter 2 is also given, highlighting the deterministic control achievable on the final superficial texture.

4.2.2 Fabrication of the micropillar array by soft imprinting

The fabrication of the pre-patterned textures onto the polymer surfaces is typically accomplished by the replica molding process belonging to the soft imprinting lithographic techniques [3,101].

The fabrication steps, needed for the fabrication of cylindrical pristine pillar arrays made of our azopolymer, are described in Figure 4.5. A single commercially available silicon wafer (i) is used as master template for the fabrication of several PDMS stamps. Once the master is treated with an anti-sticking agent, the PDMS (Sylgard 184, Dow Corning) mixture (precursor and the curing agent in a 10:1 weight ratio) is gently poured onto the silicon master (ii) and placed onto a hot-plate until the complete curing is achieved. Then the PDMS mold is carefully released from the silicon wafer (iii) and stored in a clean box. For the texture transfer onto the azopolymer surfaces, few droplets of the azopolymer in NMP solution (10% by weight) are casted onto a clean glass slide (iv) and placed onto a horizontally leveled hot plate. Then the PDMS stamp is carefully leant onto the substrate, tacking care that no air is trapped in the liquid solution (v). The mold is maintained at 45°C overnight and finally the PDMS mold is carefully released from the polymer surface which presents the replica of the pillar-like texture (vi).

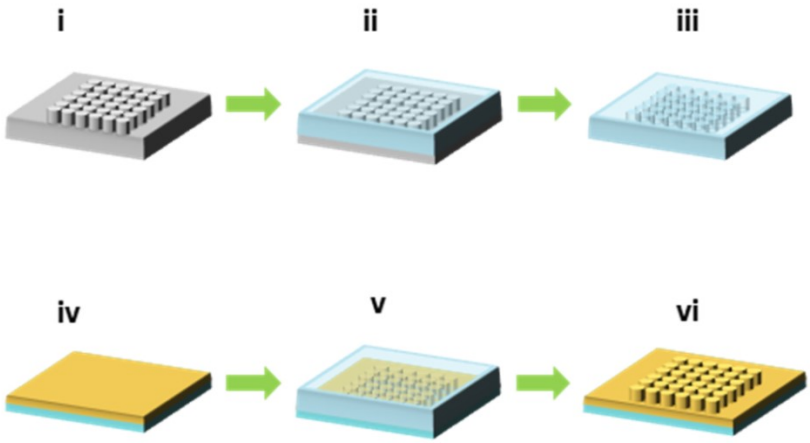

Figure 4.5| Schematic representation of the fabrication steps for the replica molding of the pristine azopolymer micro-posts from a silicon master.

SEM images of the typical as-prepared textured polymer surface are presented in Figure 4.6. Cylindrical posts, arranged in a square array of pitch $p = 10.0\ \mu m$, diameter $d = 4.6\ \mu m$ and height $h = 2.0\ \mu m$, are homogeneously fabricated on an $1\ cm \times 1\ cm$ area with good quality.

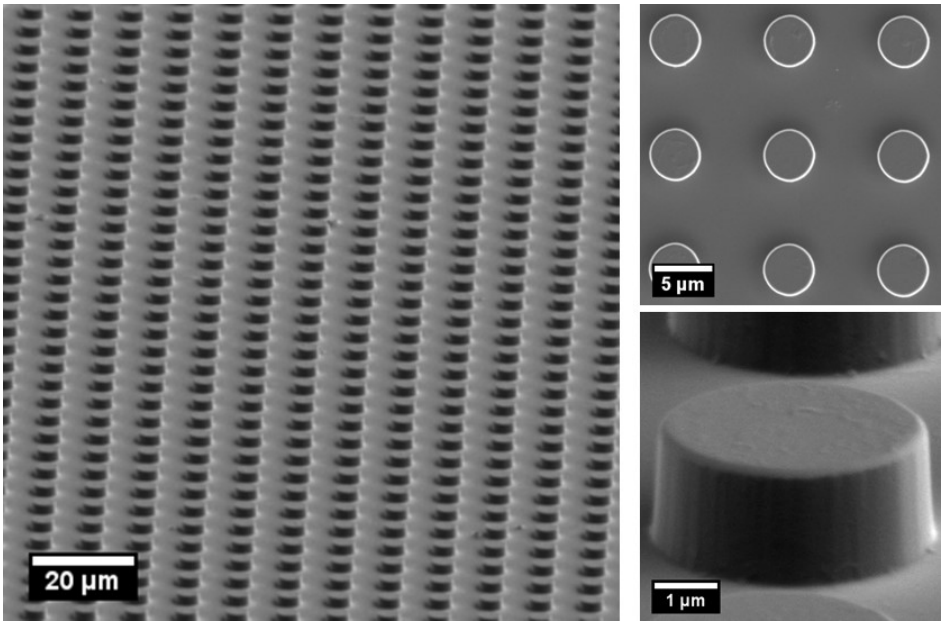

Figure 4.6| SEM images of the as-prepared array of cylindrical pillars fabricated by soft imprinting from the PDMS stamp.

4.2.3 Light-induced micro-pillar reconfiguration

The schematic representation of the optical setup used for light-driven reconfiguration of the azopolymer micro-pillars is presented in Figure 4.7(a). The illumination source is a solid state diode laser (L) (Coherent OBIS 488 LS) at wavelength of 488 nm. The polarization state of the laser beam is properly controlled by introducing an half or, alternatively, a quarter waveplate along the optical path (Polarization Plates, PP, in the scheme of Figure 4.7). The beam is expanded by means of a beam expander (BE) to a diameter of about 3 cm and then adjusted via a circular iris or a rectangular slit (I/S) before the sample in order to minimize the effect of the intensity gradient of the gaussian laser beam. The sample holder (SH) is placed on a xyz translational stage equipped with a rotational stage (RS) in order to control the light incidence angle.

As mentioned before, the light-driven reconfiguration turns the simple cylindrical or cubic pillars into three-dimensional geometries having more complex architectures, whose geometry depends on the polarization state of the illuminating beam [10,11,13,78,102]. The polymer motion starts at the top surface of the structures and, without any external constraint, gradually involves the whole volume of the micro-posts as the reconfiguration process goes on. However, as described in reference [10],

the azopolymer flow can be spatially constrained at the top surface of the structures by illuminating the pristine pillar array through a transparent flat PDMS capping layer placed in tight contact with the top surface of the posts. In this configuration, illustrated in Figure 4.7, the adhesion forces arising between the polymer and the capping layer prevent the polymer flow from heading toward the bottom surface of the film, and the light-driven material motion occurs mainly in contact with the flat PDMS layer, producing top-flat three-dimensional reconfigured architectures.

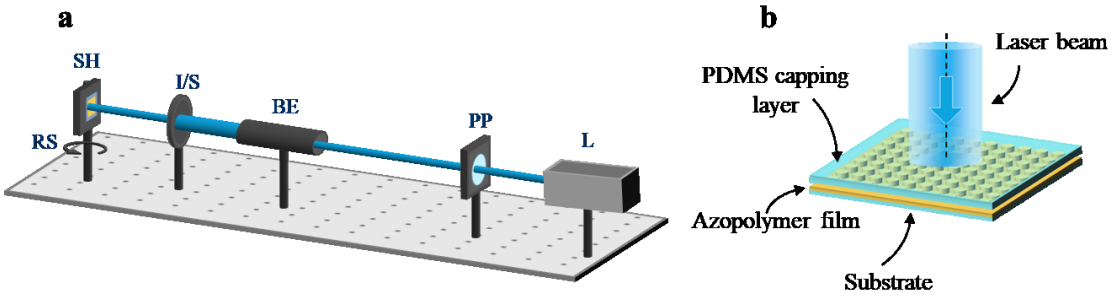

Figure 4.7| (a) Schematization of the optical setup used for the azopolymer micro-pillars reconfiguration. (b) Schematic representation of pillar reconfiguration condition with the flat PDMS capping layer attached to the top surfaces of the structures during the light-reconfiguration process.

Figure 4.8 shows the SEM images of the posts obtained from the exposure of the pristine cylindrical pillar array (of the type described in Figure 4.6) with the laser beam in different illumination conditions. In particular, the laser beam illuminates the pillar array at normal incidence through the transparent PDMS capping layer, while the beam polarization state is conveniently varied in each experiment. Figure 4.8(a) and (b) report the structures resulting from the illumination with the beam linearly polarized in two orthogonal directions. As expected, the linear polarization produces a symmetric displacement of the material at the top surface of the posts in the preferential direction of the light polarization, and the reconfigured architectures can be described as having a flat top 'pseudo-elliptic' section, with the major axis oriented in the light polarization direction. A break of the original circular symmetry was obtained also for the posts reconfigured with elliptically-polarized light, which become mostly elongated in the direction of the long-axis of the polarization ellipse (Figure 4.8(c)). Circularly polarized light produces, instead, structures still having the original circular symmetry (Figure 4.8(d)) because of the lack of a preferential direction for the polymer mass transport in this illumination condition.

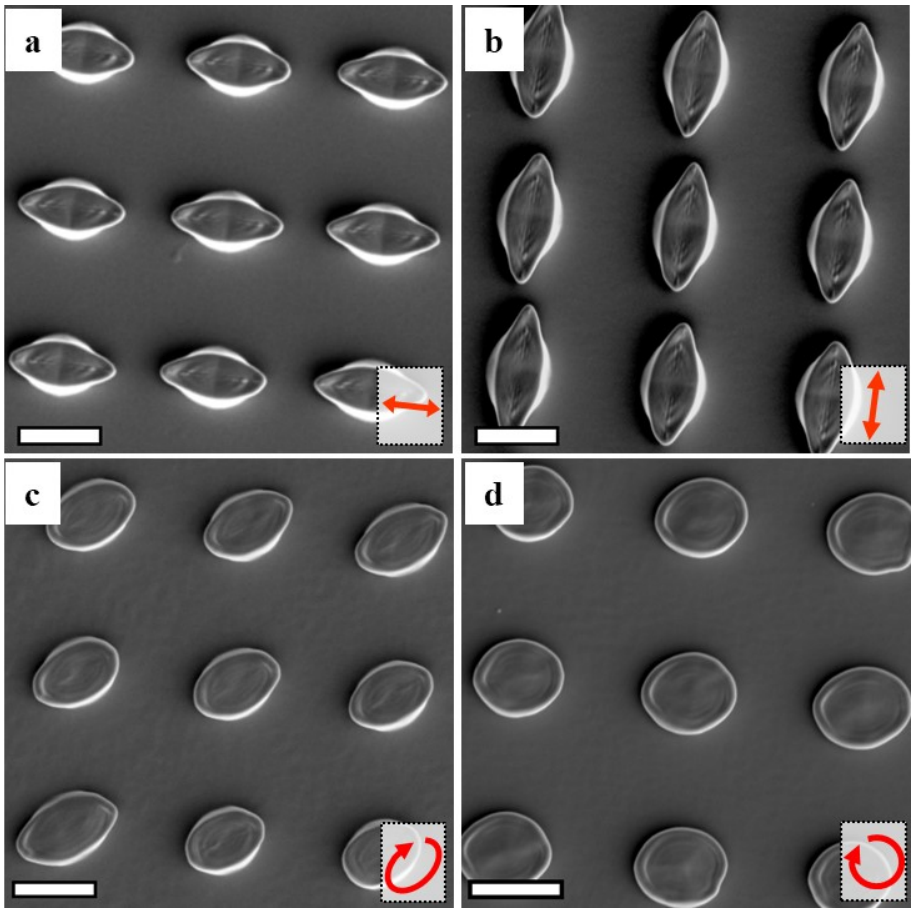

Figure 4.8| Dependence of the pillar reconfigured geometry on the illuminating light polarization. (a) and (b) SEM images of the azopolymer micro-posts reconfigured by a laser beam linearly polarized in two orthogonal directions (specified by the direction of the red arrows). (c) and (d) SEM images of the structures resulting from the reconfiguration with elliptical and circular light polarization, respectively. Scale bars 5 um.

4.2.4 Superficial asymmetry

The degree of induced asymmetry in the reconfigured posts depends on the laser fluence during the illumination. In a simple experimental situation, textured surfaces with different directional asymmetries on the micro-scale can be obtained by tuning only the film exposure time at fixed illumination intensity. As far as the light-driven pillar reconfiguration is realized through the PDMS capping layer, the geometrical description of the three-dimensional architectures can be properly approximated by only considering the contour of the posts top-surface, while the height can be assumed

unchanged with respect to the pristine pillars (the shorter the exposure time, more valid is this approximation). Therefore, the degree of induced asymmetry of the azopolymer pillars after the light driven reconfiguration can be described by the asymmetry parameter A, defined as the ratio of the long axis l (indicated by the red arrow in Figure 4.9(a)) to the short axis s (green arrow) of the flat-top reshaped pillar surface.

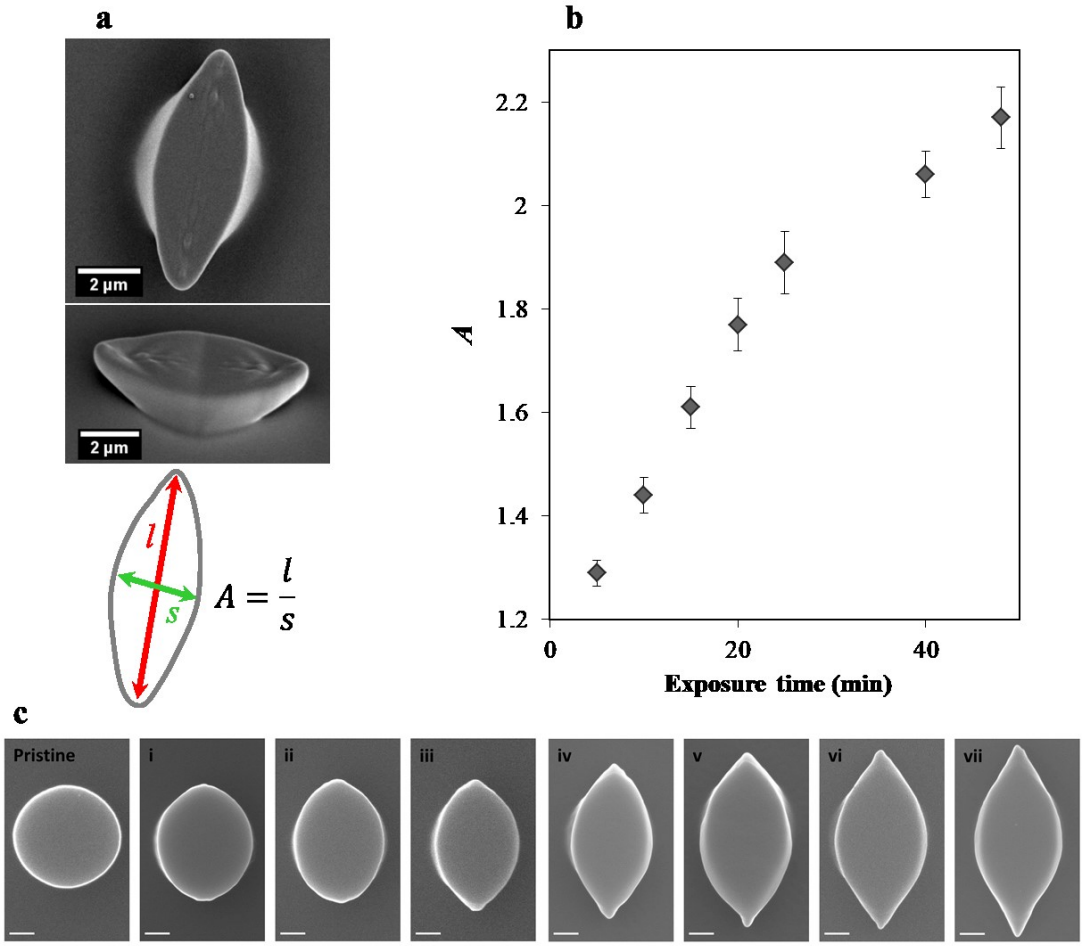

Figure 4.9| Light-induced azopolymer micro-post asymmetry. (a) Top and side views of a typical reconfigured micro-structure, together with the definition of the post asymmetry parameter A after the light-driven reconfiguration process. (b) Measured asymmetry as function of the exposure time at fixed illumination intensity of 75 mW/cm^2. (c) SEM images of a reconfigured pillar belonging to the array of reconfigured structures at different exposure time. Scale bar 1 µm.

The value of the measured asymmetry resulting from the illumination of different pristine arrays with increasing exposure time at fixed laser intensity of 75mW/cm^2 is reported in Table 4.1 and plotted in Figure 4.9(b). The parameter A for each sample is

determined from SEM images as the mean of at least 100 asymmetry measurements of individual pillars in the reconfigured array, while its uncertainty is calculated as the standard deviation of the measured asymmetry distribution in each sample. For clarity, Figure 4.9(c) shows the SEM images of one exemplifying reconfigured pillar for each illuminated sample. The asymmetry *A* showed a non-linear increasing trend as the exposure time increased. However, the asymmetry increase is mainly related to the elongation of the structures in the long axis direction (65% maximum elongation) rather than to the contraction in the short axis (15% maximum contraction) (Figure 4.9(c)).

Table 4.1| Data of the micro-post structural asymmetry for azopolymer pillars reconfigured at increasing exposure laser fluence. The illumination intensity for all the reconfiguration experiment is kept fixed at 75 mW/cm^2. The different reconfigured arrays are labeled with increasing roman numbers and match the SEM image sequence in Figure 4.9(c).

Sample	Exposure time	Pillar asymmetry
i	5 min	1.29 ± 0.05
ii	10 min	1.44 ± 0.07
iii	15 min	1.61 ± 0.08
iv	20 min	1.8 ± 0.1
v	25 min	1.9 ± 0.1
vi	40 min	2.0 ± 0.1
vii	48 min	2.2 ± 0.1

4.2.5 Phenomenological model

The observed light-induced reconfiguration of the azopolymer micropillars can be qualitatively described in the framework of the phenomenological light-induced mass migration model presented in chapter 2. There, we have largely commented how the differences in the anisotropic diffusion efficiency of the azomolecules at the free surface with respect to the bulk polymer give rise to an enhanced superficial mass current term which explains, for example, the spiral surface reliefs under vortex-beam irradiation. This surface current term, moreover, is also the one able to qualitatively predict the material displacement in the case of light-induced reconfiguration of isolated azomaterial micro-volumes.

In this case, indeed, the mass migration occurs under homogeneous irradiated light patterns, implying a driving effect no longer related to the intensity gradients of the illumination pattern, which are identically vanishing. The resulting non-vanishing mass

migration observed experimentally is not easily explained by most of the mass migration models, which otherwise always require the coupling of the flat azomaterial surface with a "non-flat" illumination pattern (non- vanishing intensity gradient). As we will see below, the superficial mass current term of the phenomenological anisotropic model, on the contrary, describes the light-induced reconfiguration of the pre-patterned azomaterial structures as the result of a peculiar coupling of the flat illumination pattern with a non-flat curvature of the pristine architectures.

The detailed description of the phenomenological mass migration model is given in the recent work reported in the reference [10]. Here, however, the main points of the calculations are described in a simplified situation with the aim to highlight the correct predictions of the model also in this case, with the consequent possibilities in terms of deterministic control on the final obtained structures which follows from such theoretical success.

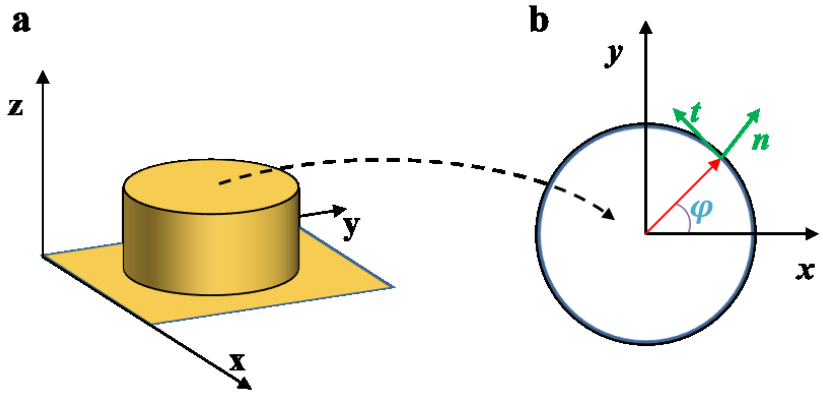

Figure 4.10| Phenomenological model for micro-pillars light-induced reconfiguration. (a) Definition of the geometry of the initial experimental situation described in the model. (b) Definition of the coordinate system. The blue curve represents the initial contour curve of the cylinder top surface.

Let us to consider a single cylinder of photo-responsive azomaterial positioned onto a rigid and plane substrate (Figure 4.10). The coordinate system is chosen such that the x-y plane coincides with the substrate surface and the z axis is oriented along the cylinder axis. Under linearly polarized beam irradiation, the light-reshaped structure can be approximately described by the reconfiguration of the contour of the top surface of the micro-cylinder, which passes from a symmetric circle to an asymmetric pseudo-elliptic curve (see Figure 4.7). It is convenient to adopt the parametric representation of this curve in the x-y plane, so that the pillar contour is described by two functions *x(s)*

and *y(s)*, with *s* being a continuous parameter in the fixed range [0,1]. Under illumination, this curve is deformed by the light-induced mass migration and the parametric functions acquire an explicit dependence on the time: *x(s,t)* and *y(s,t)*. As the contour is a closed curve, the parametric functions verify the relations *x(0)=x(1)* and *y(0)=y(1)* for any t.

Before the illumination starts, the pillar top surface contour is a circle of radius *r* (Figure 4.10(a)) described by the parametric functions:

$$\begin{cases} x(s,t=0) = r\cos\left[2\pi s\right] \\ y(s,t=0) = r\sin\left[2\pi s\right]. \end{cases} \tag{4.1}$$

To model the reconfiguration process, it is convenient to introduce the tangential and the normal unit vectors to the contour curve, as described in Figure 4.10(b).

$$\hat{\boldsymbol{n}} = \frac{1}{\sqrt{\left(\frac{\partial x}{\partial s}\right)^2 + \left(\frac{\partial y}{\partial s}\right)^2}} \begin{pmatrix} \frac{\partial y}{\partial s} \\ -\frac{\partial x}{\partial s} \end{pmatrix} \tag{4.2}$$

$$\hat{\boldsymbol{t}} = \frac{1}{\sqrt{\left(\frac{\partial x}{\partial s}\right)^2 + \left(\frac{\partial y}{\partial s}\right)^2}} \begin{pmatrix} \frac{\partial x}{\partial s} \\ \frac{\partial y}{\partial s} \end{pmatrix} \tag{4.3}$$

The optical field of the illuminating homogenous and linearly polarized beam in a generic direction of the x-y plane, is described by the:

$$\boldsymbol{E} = E_0 \begin{pmatrix} E_x \\ E_y \end{pmatrix}. \tag{4.4}$$

Using the relations (4.2) and (4.3), the normal and tangential components of the electric field at any point of the curve are given by:

$$E_n = \boldsymbol{E} \cdot \hat{\boldsymbol{n}} = \frac{E_0}{\sqrt{\left(\frac{\partial x}{\partial s}\right)^2 + \left(\frac{\partial y}{\partial s}\right)^2}} \left(E_x \frac{\partial y}{\partial s} - E_y \frac{\partial x}{\partial s} \right) \tag{4.5}$$

$$E_t = \boldsymbol{E}\cdot\hat{\boldsymbol{t}} = \frac{E_0}{\sqrt{\left(\frac{\partial x}{\partial s}\right)^2+\left(\frac{\partial y}{\partial s}\right)^2}}\left(E_x\frac{\partial x}{\partial s}+E_y\frac{\partial y}{\partial s}\right) \tag{4.6}$$

Following the anisotropic diffusion model for the light induced mass migration presented in section 2.1 [8,10,46], the optical field of the illuminating light, induces a azopolymer mass current described in the general form by (see relation 2.16):

$$\begin{aligned}\bar{J}_k = {} & C_1\partial_k\left(E_l^*E_l\right)+C_2\partial_l\left(E_l^*E_k+E_k^*E_l\right)+C_3\partial_k\left|E_z\right|^2+\\ & +\frac{C_s}{L}\left(E_z^*E_k+E_zE_k^*\right).\end{aligned} \tag{4.7}$$

As discussed before, as the optical electric field illuminating the cylinder is uniform in the considered situation, all the terms explicitly depending on the filed gradients in (4.7) vanish identically and the only non-zero term is the surface current which depends on the field and not on its gradients. For the electric field form given by (4.5) and (4.6), the mass current writes as:

$$\bar{J}_t = \frac{C_s}{L}\left(E_n^*E_t+c.c.\right), \tag{4.8}$$

where $\bar{J}_t$ is the tangential component of the mass current averaged along the effective penetration length into the azopolymer L, C_s is the surface coefficient characteristic of the azomaterial (see section 2.1) and *c.c.* stands for complex conjugated of the first term appearing in the bracket. By inserting relations (4.5) and (4.6) in (4.8) we can obtain the explicit form of this mass current term for any polarization direction of the optical field. Even if the calculation can be conducted easily for any polarization direction and also for a non-normal incidence angle of the illuminating beam (see supporting information of reference [10]), here, in order to maintain the calculation as simple as possible, we assume a specific polarization direction in the y direction and a normal incidence. With this assumption, equation (4.8) explicitly becomes:

$$\bar{J}_t = -\frac{2C_S}{L}\frac{E_0}{\sqrt{\left(\frac{\partial x}{\partial s}\right)^2+\left(\frac{\partial y}{\partial s}\right)^2}}\left[\left(\frac{\partial x}{\partial s}\right)\left(\frac{\partial y}{\partial s}\right)\right]. \tag{4.9}$$

The surface reshaping can be calculated as a displacement $\hat{\boldsymbol{n}}\,\Delta h(s)$ of the contour curve along the normal direction, as resulting from tangential mass current $\bar{J}_t$ which drives the

material inflow or outflow at any curve position. Assuming the polymer incompressibility as in the case of the surface reliefs induced onto flat azopolymer films, the normal material displacement $\hat{\boldsymbol{n}}\,\Delta h(s)$ can be related to the mass current by the continuity relation, giving:

$$\frac{\partial h}{\partial t}(s)\hat{\boldsymbol{n}} = -\left(\frac{L}{\rho}\right)\frac{\partial \bar{J}_t}{\partial l_t}\hat{\boldsymbol{n}} = -\left(\frac{L}{\rho}\right)\frac{1}{\sqrt{\left(\frac{\partial x}{\partial s}\right)^2+\left(\frac{\partial y}{\partial s}\right)^2}}\frac{\partial \bar{J}_t}{\partial s}\hat{\boldsymbol{n}}\,, \tag{4.10}$$

where l_t is the local curve length along the tangential direction. This height variation is translated into the contour reshaping as described by the velocities:

$$\frac{\partial x}{\partial t}(s) = n_x\frac{\partial h}{\partial t}(s) = \left(\frac{L}{\rho}\right)\frac{1}{\left(\frac{\partial x}{\partial s}\right)^2+\left(\frac{\partial y}{\partial s}\right)^2}\left(\frac{\partial y}{\partial s}\right)\left(\frac{\partial \bar{J}_t}{\partial s}\right) \tag{4.11}$$

$$\frac{\partial y}{\partial t}(s) = n_y\frac{\partial h}{\partial t}(s) = -\left(\frac{L}{\rho}\right)\frac{1}{\left(\frac{\partial x}{\partial s}\right)^2+\left(\frac{\partial y}{\partial s}\right)^2}\left(\frac{\partial x}{\partial s}\right)\left(\frac{\partial \bar{J}_t}{\partial s}\right). \tag{4.12}$$

In order to make this expression explicit, we need to evaluate the derivative of the mass current expressed by relation (4.9) respect to the parameter s. The direct calculation gives:

$$\begin{aligned}\frac{\partial \bar{J}_t}{\partial s} = &-\frac{2C_S}{L}\frac{|E_0|^2}{\left(\frac{\partial x}{\partial s}\right)^2+\left(\frac{\partial y}{\partial s}\right)^2}\left[\left(\frac{\partial^2 x}{\partial s^2}\right)\left(\frac{\partial y}{\partial s}\right)+\left(\frac{\partial^2 y}{\partial s^2}\right)\left(\frac{\partial x}{\partial s}\right)\right]+\\ &+\frac{2C_S}{L}\frac{|E_0|^2}{\left(\frac{\partial x}{\partial s}\right)^2+\left(\frac{\partial y}{\partial s}\right)^2}2\left\{\left[\left(\frac{\partial x}{\partial s}\right)\left(\frac{\partial y}{\partial s}\right)\right]\left[\left(\frac{\partial^2 x}{\partial s^2}\right)\left(\frac{\partial x}{\partial s}\right)+\left(\frac{\partial^2 y}{\partial s^2}\right)\left(\frac{\partial y}{\partial s}\right)\right]\right\}\end{aligned} \tag{4.13}$$

The main result of this calculation is that the relation (4.13) predicts a non-zero surface deformation only in the regions where the surface is not flat, as described by the direct dependence of the deformation on the local curvature of the contour curve through the second derivative of the parametric curve functions. A similar condition is clearly verified for the contour curve of any isolated micro-volume of azomaterial, and is the

fundamental reason why the model predicts correctly a non-vanishing mass current also for uniform illumination patterns.

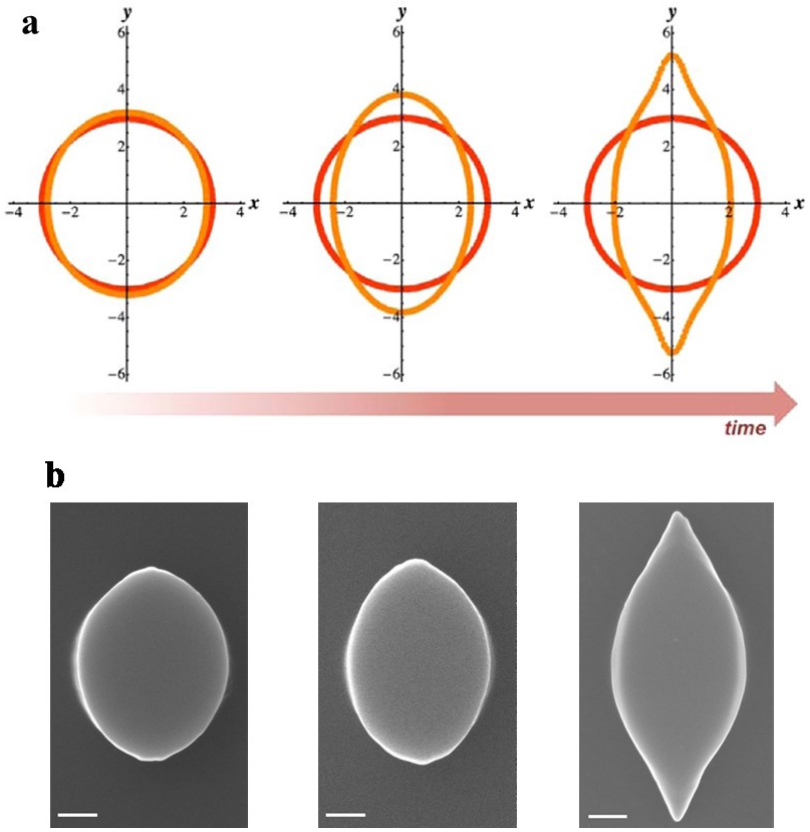

Figure 4.11| Comparison between the predictions of the model and experimental structures. (a) Simulated contour curves of the top pillar surface at increasing exposure times as predicted from the model. Reproduced from reference [9]. (b) SEM images of the experimental reconfigured azopolymer micro-pillars for different exposure times as described in the previous section. Scale bar in SEM images 1 μm.

The simulated[4] pillar contour deformation, reproduced from reference [10], for three different exposure times as predicted from relations (4.11), (4.12) and (4.13), are shown in Figure 4.11(a). The simulated contours are compared with the experimental SEM images of the reconfigured pillars described in previous section. As can be immediately recognized, the simulated contour shapes are fully consistent with the deformation observed experimentally. These theoretical and experimental complete

[4] In reference [10] an additional term taking into account the surface tension has been added to the longitudinal mass current in order to make the equation stable respect to the appearence of surface roughness.

agreements have a two-fold importance here: first the demonstration of the ability of phenomenological model based on the light-induced anisotropic molecular diffusion of the azomoieties in describing another set of experiments where the other mass migration models lack, strengthen the fundamental basis of that theoretical model; second, the reconfiguration process is demonstrated to be fully deterministic and predictable, allowing in principle an a-priori control on the light-engineered micro-structures.

4.2.6 Slanted pillar reconfiguration

In the analyzed light-driven superficial reconfiguration situation, the control of another straightforward degree of freedom of the illumination configuration allows even a unidirectional deformation of the structures. Such experimental parameter is the incidence angle of the polarized beam used for the light-driven array reconfiguration [10]. Figure 4.12(b) and (c) show the SEM images of the azopolymer pillar array reconfigured using the illumination configuration schematized in Figure 4.12(a). The linearly polarized laser beam (the polarization direction is indicated by the red arrow) illuminates the sample through the PDMS flat capping layer at the incidence angle φ=45°. In particular, the sample is rotated respect to the laser beam around an axis contained in the sample plane, passing through the center of the patterned pillar texture and orthogonal to the linear polarization direction of the illuminating beam. Due the non-uniform illumination of the pillars and shadow effects [10], the light-driven polymer mass-migration results asymmetrical in the light polarization direction and gives rise to tilted structural reconfigurations. More specifically, the reshaped pillars are more elongated in the polarization direction toward the side of the incoming illumination beam (Figure 4.12(a)).

The asymmetric unidirectional structures obtained in this simple one-step fabrication process are of great interest for many practical applications. One of these will be discussed in detail in chapter 5 and relates with the control of the wettability properties that these kinds of light-reconfigurable surfaces permit. Typically, unidirectional asymmetric structures, are obtained either with expensive dedicated lithographic approaches [103,104], or with multi-step complex procedures [105,106]. Furthermore, such structures are not reconfigurable after fabricated so that they require a specific fabrication process for any specific desired final geometry. On the contrary, the asymmetric light-driven reconfigurable structures reported here have the tremendous advantage, with respect to the other fabrication technique, of their very simple and cost-effective fabrication steps. Starting from a single photo-lithographic mask necessary for

the fabrication of the pristine pillar array, the actual degree of unidirectional asymmetry is established by controlling the light incidence angle, while the overall amount of structural asymmetry is determined by the light irradiation time and/or intensity. Furthermore, the reconfiguration process is even reversible, as described in the next section.

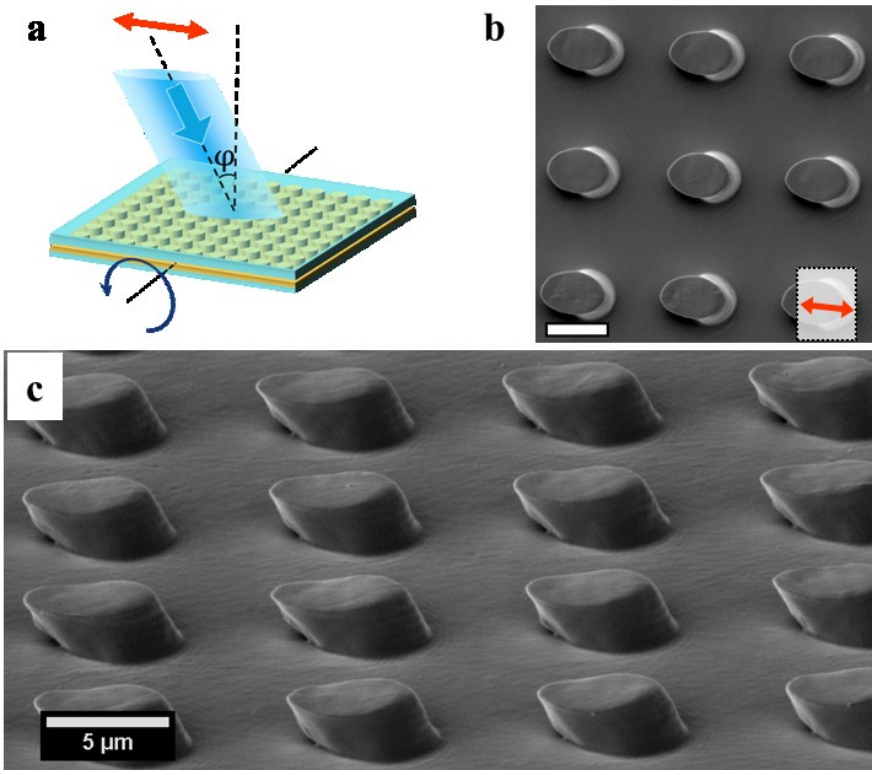

Figure 4.12| (a) Schematic presentation of the illumination configuration for slanted pillars reshaping. (b) SEM top-view image (scale bar 5um) and (c) side-view image of the tilted pillars.

4.2.7 Multi-step reversible light-driven reconfiguration

The reversibility of the azomaterial light-induced superficial structures is one of the distinguishing key points of the mass migration phenomenon which has attracted great interest since the first SRG demonstrations. The possibility of having reversible light-reconfigurable surfaces did so that these materials became good candidates for applications in high density holographic data storage, real-time superficial photo-manipulation etc. Despite the process at the basis of the light-driven reconfiguration of isolated micro-volumes of the azomaterial is exactly the same of the reversible process which gives rise to the light-erasable SRG, it is quite surprising to observe how this

phenomenon is able to completely restore the initial symmetric structure of the micro-pillars illuminated in multi-step sequential process [11,23]. Indeed, if the structural deformation of the light-reconfigured azopolymer pillars is not so large to involve significantly the entire volume of the microstructures, the reconfiguration process can be reversible and the initial circular symmetry of the pillars can be restored by a two-step illumination process. This can be achieved by the subsequent irradiation of the array in the exactly same illumination configuration but with polarization direction rotated by 90° degrees with respect to the first reconfiguration step [11,23].

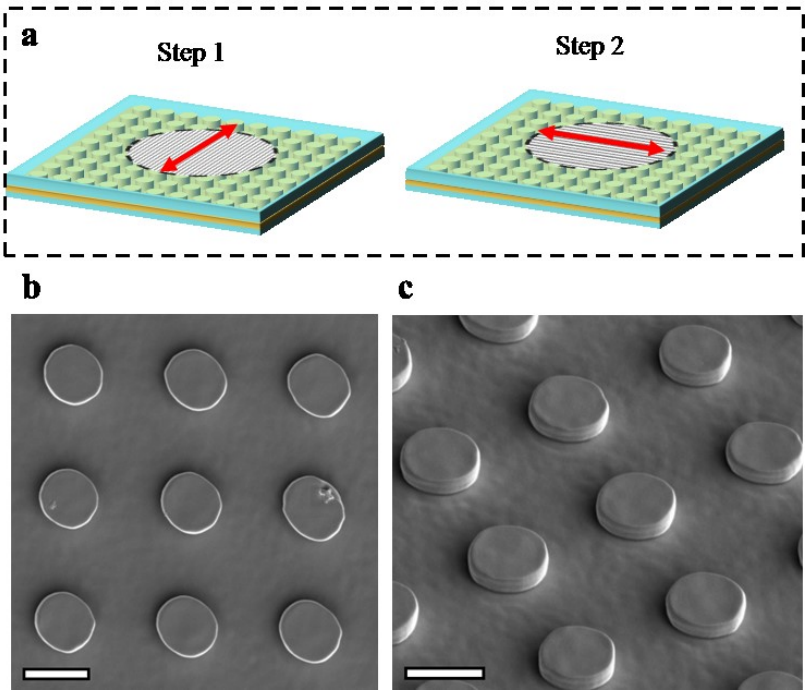

Figure 4.13| Reversibility of the micro-pillar light-induced reconfiguration process. (a) Schematic representation of the two-step illumination configuration of the experiment. The two steps are identical in all the irradiation parameters (beam intensity and incidence angle) but have a polarization direction rotated by 90° (indicated by the red arrows). (b) and (c) SEM images of the top and side views, respectively, of the pillar structures resulting by the two step illumination process. In the experiments the illumination intensity is fixed at 20W/cm^2, and the exposure time in each step is 1 hour. Scale bars correspond to 5 μm.

This situation is schematized in Figure 4.13(a), where the two subsequent illumination steps are identical in terms of exposure intensity and light incident angle, but the linear polarization direction is rotated by 90° in the illumination step 2 respect to the step 1. The SEM images of the structures resulting from this two-step illumination process onto our azopolymer micro-pillars are presented in Figure 4.13(b) (top view)

and Figure 4.13(c) (side view). Even if after the illumination step 1 the structures acquire the typical asymmetric geometry described above (Figure 4.8(a)-(b)), the subsequent illumination with a beam polarization rotated by 90° degrees produces a complete restoring of the original pristine geometry (Figure 4.13).

A similar behavior can be understood only if the material displacement at the pillar top surface is governed by a light-surface coupling whose strength depends on the local curvature of the pillar contour. Even if a direct observation of the material dynamics during the light-reshaping process would be needed to clarify the exact dynamics, we can phenomenologically describe the restoring process phenomenon as follow. The situation is schematically presented in Figure 4.14.

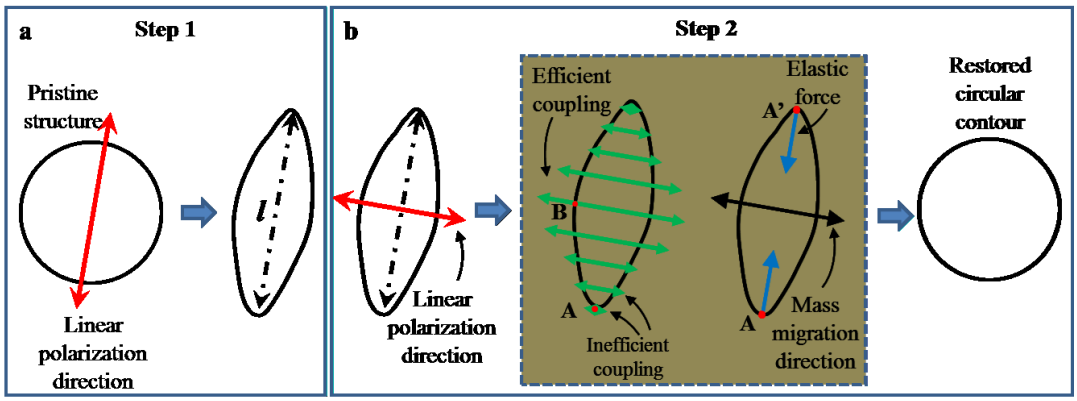

Figure 4.14| Scheme of circular symmetry recovery of azopolymer pillar reconfigured in two steps illumination. (a) First illumination step with linearly polarized in the direction of the red arrow, which results in structural elongation. (b) Second illumination step with light polarization direction with respect to the first step. The process leading to the circular shape restoring is supposed to involve the asymmetric structure with anisotropic efficiency, depending on the local curvature of the contour of the top pillar surface (schemes in the dashed rectangle).

In order to achieve a restoring of the initial circular contour transformed in a pseudo-ellipse during the first illumination step Figure 4.14(a), the efficiency of the mass migration movement at the point A of the top-contour should be very low, while the movement of the point B is certainly the most efficient. The net result is that a mass migration in the direction of the light polarization starts only in correspondence of the short axis of the already asymmetric structure, instead of involving the whole contour curve with the same efficiency. In this case, indeed, an overall enlargement of the structure should be obtained instead of the experimental observation of the initial configuration. Because of the visco-elastic forces inside the polymer, the points A and A' are hence subjected to effective forces pointing toward the center of the pillar which

cause the restoring of the circular symmetry. We believe that a similar behavior should be predicted by the phenomenological model described in section 4.2.5, so that this restoring mechanism represents the next set of experiments further validating the model.

It is worth nothing that disequilibrium in the energy transferred to the polymer during the two subsequent illumination steps (for example using a longer exposure time in one of the two steps) produces a not completely compensated irradiation dose. In this situation, the structures would be more elongated in the direction coincident with the polarization direction of the most energetic illumination step. This effect can be efficiently used for a sequential and reversible light-induced reconfiguration of the superficial azopolymer microstructures, as effectively demonstrated in the recent works reported in references deformation [11,96], which adds a great degree of versatility toward the effective use of these materials for practical applications.

5 Tailoring the wettability of azopolymer pre-patterned surfaces

The study of wettability refers to the investigation of the behavior of a liquid deposited onto a solid substrate. Wetting phenomena rule many aspects in Nature and play a role in several peculiar natural functionalities found in the plant and animals kingdoms [107]. Inspired by some of these abilities, like the self-cleaning properties of the lotus leaves, the directional scrolling of the butterfly wings, or the force provided by the water strider's leg, many efforts have been made to understand and control the wetting behavior of the surfaces. Now, wetting phenomena are commonly used in many scientific and technologic fields ([108–110]), making this field of research one of the most active in the scientific world.

Great attention is devoted in particular to the effects produced by the roughness at micro and nanoscale on the macroscopic wettability behavior of the solid surface. It is known, indeed that, together with the chemical nature of the liquid and the solid involved, the behavior of a liquid drop onto a solid surface mainly depends on superficial texture of the surface at different length scales. This dependence is what just determine the self-cleaning and the directional roll of abilities of the lotus leaves and butterfly wings, for example. As a consequence, the control and the engineering of the superficial roughness represent a fundamental tool in order to tailor the wetting state of solids. Furthermore, a deterministic control on the final wetting behavior requires some theoretical model able to relate the geometrical parameters of the superficial textures to the shape of a liquid drop deposited on it.

The commonly theoretical models used at this task are the Wenzel [111] and Cassie-Baxter models [112]. These models, indeed, are able to explain the great majority of the observed experimental situations. However, some roughness-induced wetting phenomena do not fall in the scenario of these simple thermodynamic models, and need a discussion beyond the standard framework. These situations include, for example, the wetting anisotropy induced by asymmetric textures, the pinning effect at

sharp superficial edges, or the omniphobicity produced by superficial architectures having re-entrant edges.

Besides the proper theoretical environment necessary for the geometry-driven wettability, also the actual ability in the effective fabrication of controlled three-dimensional superficial features has a remarkable importance. Textured solid surfaces for wettability studies and applications are typically fabricated by standard lithographic techniques, including photolithography, electron beam and focused ion beam lithography, self-assembly, and soft lithography [101,106,113–115]. However, as already demonstrated in the previous chapter, the directional light-induced mass migration phenomenon occurring in azomaterials suggests a new promising fabrication approach for the realization complex three-dimensional and deterministic superficial textures. Using the light-driven reconfiguration of pre-patterned micro-structures, a controlled superficial asymmetry and its directional extension over the surface have been largely demonstrated. These, can be transferred naturally into final directional wetting anisotropies, which can be further finely tuned by variating the irradiation conditions [11,12,116].

In this chapter, the ability of these light-reconfigured structures in tailoring the anisotropic wetting behavior of the azopolymer surface is discussed in detail. Before this, a brief description of the standard roughness-base wettability models is given, together with an overview on the non-standard wetting effects, like the omniphobicity and the wetting anisotropy, which arise from peculiar geometries in the superficial textures of the substrates. Also the wetting state of our pre-patterned array of cylindrical azopolymer micro-pillars, is not explainable with the standard thermodynamic wetting models. Our case is indeed governed by the pinning of the liquid drop at the edge of the sharp pillar microstructures. This effect has been rationalized only very recently by a theoretical model, which is discussed and explicitly specified to our situation in section 5.2.2. Finally, the tailoring in two dimensions of both the wetting anisotropy and the directional liquid spreading is demonstrated onto the light-reconfigured pillar array irradiation with spatially structured polarization and/or intensity patterns.

5.1 The wettability of rough surfaces

5.1.1 Wenzel an Cassie-Baxter models

When a drop of a certain liquid is placed in contact with a solid substrate, the drop shape varies until an equilibrium configuration is reached. The angle formed by the liquid-air interface of the drop with respect to the horizontal solid surface can be used to characterize the wetting state of the solid-liquid system, and takes the name of equilibrium *contact angle* (CA).

The contact angle θ_0 that a drop of the considered liquid forms in contact with the ideally flat, homogeneous, and rigid surface is described by Young's equation [117]:

$$\cos\theta_0 = \frac{\gamma_{SV} - \gamma_{SL}}{\gamma_{LV}}, \tag{5.1}$$

where γ_{SV}, γ_{SL} and γ_{LV} represent the interfacial free energies per unit area of solid-vapor, solid-liquid, and liquid-vapor interfaces, respectively. This relation derives by the simple balance of the forces acting on the unit length of the line of liquid contact, also termed Triple-phase Contact Line (TCL) with the solid substrate, as schematized in Figure 5.1(a). Generally, solid surfaces characterized by $\theta_0 < 90°$ are considered to be hydrophilic, while those having $\theta_0 > 90°$ are hydrophobic. However, the ideal situation described by Young's relation is never realized in the practice, since solid surfaces are typically both heterogeneous and rough. In particular, the roughness has been found to play a crucial role in determining the wetting properties of the substrate.

The first model describing the contact angle of a liquid drop in contact with a solid surface on the basis of the geometry of its texture, was proposed by Wenzel in 1936 [111]. In this model, the liquid drop is assumed to completely wet the surface asperities (*wetted* regime, Figure 5.1(c)). The model assumes that the roughness of the surface, described by the roughness parameter *r* defined as the ratio of the actual area of the rough surface to the geometric projected one, is characterized by a dimension scale much smaller that the drop size. In this hypothesis, the apparent contact angle θ^* can be evaluated by considering a small displacement dx of the contact line along the parallel direction of the surface, as indicated in Figure 5.1(b). In this situation, the total free energy changes by an amount dF and can be written, for the unit length of the contact line, as:

$$dF = r\left(\gamma_{SL} - \gamma_{SV}\right)dx + \gamma_{LV}\,dx\cos\theta^*. \tag{5.2}$$

The system will reach the thermodynamic equilibrium for the particular value of the contact angle that minimizes the system free energy, so that $dF = 0$. The minimum condition leads to *Wenzel's relation* [118]:

$$\cos\theta_W = r\cos\theta_0, \tag{5.3}$$

where θ_0 is Young's contact angle. As the roughness parameter r is always larger than 1, in the Wenzel model the surface roughness always magnifies the intrinsic wetting behavior of the solid flat surface. More specifically, when $\theta_0 < 90°$, θ_W decreases as the roughness parameter r increases, leading to a more hydrophilic surface. In the opposite case, when $\theta_0 > 90°$, a more rough surface produce a more hydrophobic behavior. Should be noted that for high roughness ($r \gg 1$), the right-hand side of equation (5.3) can assume a value larger than 1. In this situation the Wenzel model is no longer valid.

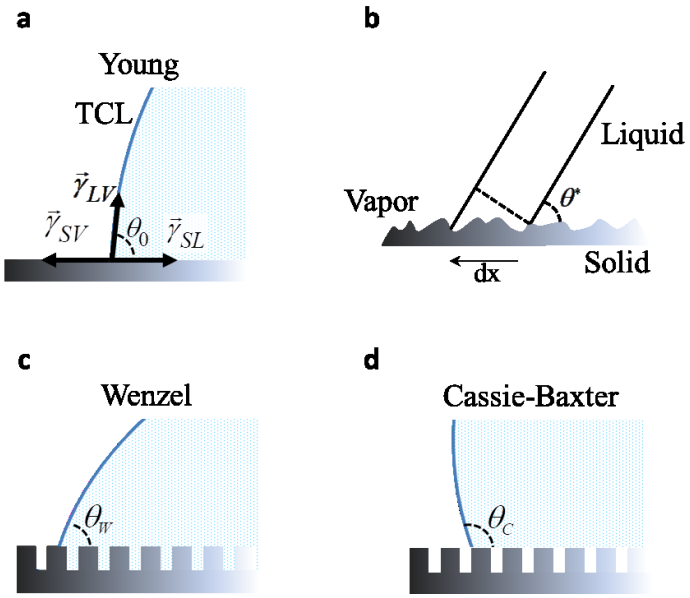

Figure 5.1| Schematic representation of the different wetting regimes. (a) Definition of the contact angle θ_0 of a liquid drop lying onto an ideally flat and homogenous solid surface as described by the Young model. (b) Scheme of the TCL placed in a rough surface. (c) Configuration assumed by the liquid drop onto the rough surface in the wetted Wenzel regime. (d) Schematic representation of the composite wetted regime described by the Cassie-Baxter model.

The second thermodynamic model commonly used for the description of the wetting of solid rough substrates, was proposed by Cassie and Baxter in 1944 [112].

The equation was derived for the description of the contact angle of a liquid lying on a *composite* heterogeneous but smooth surface constituted of two chemical species, each characterized by its own contact angle θ_1 and θ_2. Denoting with f_1 and f_2 the fractional surface areas occupied by each of these species (with $f_1 + f_2 = 1$) and assuming that each individual area is small compared with the droplet size, the system energy variation associated with a small displacement dx of the contact line is written as [118]:

$$dF = f_1\left(\gamma_{SL} - \gamma_{SV}\right)_1 dx + f_2\left(\gamma_{SL} - \gamma_{SV}\right)_2 + \gamma_{LV}\, dx \cos\theta^* . \tag{5.4}$$

The contact angle corresponding to the lowest system free energy, leads to:

$$\cos\theta_C = f_1 \cos\theta_{0,1} + f_2 \cos\theta_{0,2} , \tag{5.5}$$

where the subscript C denotes the composite wetting regime described by this relation and the angles $\theta_{0,1}$ and $\theta_{0,2}$ are, respectively, the Young's contact angles for the species 1 and 2. The application of equation (5.5) to a rough homogeneous surface requires that the liquid drop lies suspended at the composite interface constituted by the solid texture and the air trapped in the surface asperities. In this situation, the liquid does not fill the porous structure (*non-wetted* regime, Figure 5.1(d)). The two species involved in the calculation above hence become the considered solid (characterized by the area fraction $f_1 = f$) and the air (considered for the fractional area $f_2 = 1 - f$) trapped in the surface asperities. As the contact angle between air and water $\theta_{0,2}$ is 180°, relation (5.5) can be rewritten as:

$$\cos\theta_C = f\cos\theta_{0,1} - (1 - f) , \tag{5.6}$$

which defines the *Cassie-Baxter relation* for the rough surfaces in the composite wetting regime.

The Cassie-Baxter model is the one typically used to describe the *superhydrophobic* wetting regime, characterized by high water contact angles ($\theta > 150°$) and low adhesion of the liquid drop to the solid substrate, quantified by the contact angle hysteresis (CAH). The contact angle hysteresis is the difference of the *advancing* θ_a and the *receding* θ_r contact angles, defined, respectively, as the highest contact angle the liquid droplet shows before collapsing when it is pressed against the solid surfaces, and the minimum contact angle observable before the droplet detaches from the substrate when it is pushed away. In the superhydrophobic regime, the CAH is typically low (< 5°) and the droplet tends to roll away from the substrate (while keeping the spherical shape associated to the high CA value) in presence of even a very small tilt. This mechanism is at the basis of the above cited self-cleaning properties of the lotus leaves.

On the other side, drops lying in the Wenzel wetting regime are typically characterized by high values of the CAH, meaning high difficulty, or even the impossibility, of the water detachment from the surface. This situation is for example realized onto the petals of roses (from which it is named "petal effect") and can be useful in situations where liquid retaining is needed [115,119].

Which of the two wetting regimes is effectively realized by a liquid drop wetting a rough substrate depends on which contact angle produces a lower minimum in the system energy. This gives the possibility of designing ad-hoc the texture geometries, to induce, in a controlled way, one or the other wetting state. However, it was found that in many cases where the Wenzel's state is the thermodynamically favored regime, a liquid drop gently poured onto the substrate lies in the Cassie-Baxter state, which can be then forced irreversibly in the Wenzel state by providing the system with some additional energy in form of vibration or pressure. This implies that the Cassie-Baxter state can be established also if it is not the global minimum in the system energy, but constitutes a meta-stable state. As there is a great interest in the development of superhydrophobic surfaces for technological and industrial applications, many studies have been oriented toward the geometry-induced raising of these metastable effects.

5.1.2 Omniphobicity

In order to establish which of the Wenzel or Cassi-Baxter regime is energetically favored, we can note, by equating the relations (5.3) and (5.6), that a critical value exists for the intrinsic contact angle θ_{critic} of the considered liquid onto the textured surface which defines the transition between the two wetting regimes. The critical angle is written as:

$$\theta_{critic} = \cos^{-1}\left(\frac{f-1}{r-f}\right). \tag{5.7}$$

Because $f < 1$ and $r > 1$, $\theta_{critic} > 90°$. As the energy of the system decreases monotonically with the increase of $\cos\theta^*$ [113], when the liquid contacts the rough surfaces with $\theta_0 < \theta_{critic}$ Wenzel state is favored, while for $\theta_0 > \theta_{critic}$ Cassie-Baxter is energetically preferred. From this consideration it follows that a thermodynamic condition for the realization of the Cassie-Baxter regime, and hence eventually of superhydrophobicity, is a surface-liquid system for which results $\theta_{critic} < \theta_0 < 90°$. While this condition can be realized for liquids having high enough values of the liquid-vapor interface (for example water, whose surface tension is $\gamma_{LV} = 72.1$ mN/m), it is difficult to be satisfied by liquid having low surface tensions, as organic liquids (for

example octane, whose surface tension is $\gamma_{LV} = 21.6$ mN/m) [120]. However, the design of peculiar superficial micro-textures having reentrant edges can be used to induce extreme resistance to the wetting for almost all liquids, including liquids with very low surface tension [120–122]. The necessary conditions to realize this situation (often named as *omniphobicity*) are the presence of a metastable Cassie-Baxter state, and the consequent presence of a geometry-established energy barrier separating this metastable state and the energetically favored Wenzel state. This energy barrier can be provided by the capillary force acting onto the liquid contact line, which can prevent the liquid penetration into the texture. However, the crucial parameter determining the direction of the net traction of the capillary force is the angle ϕ formed by the lateral side of the reentrant structure with respect to the horizontal axis, as described qualitatively in Figure 5.2(a). In particular, for a liquid with $\theta_0 < 90°$, the situation $\phi > \theta_0$ described in the left panel of Figure 5.2(a), produces a concave liquid-air interface and the net capillary force F is directed toward the inside of the texture, favoring the complete wetting of the surface. On the contrary, when $\phi < \theta_0$, the net force is directed toward the liquid volume and it contrasts the liquid imbibition (left panel in Figure 5.2(a)). In this case, a composite solid-liquid-air interface can be induced and a metastable Cassie-Baxter state rises. Taking advantage from this effect, several omniphobic textured surfaces have been effectively fabricated [120–122].

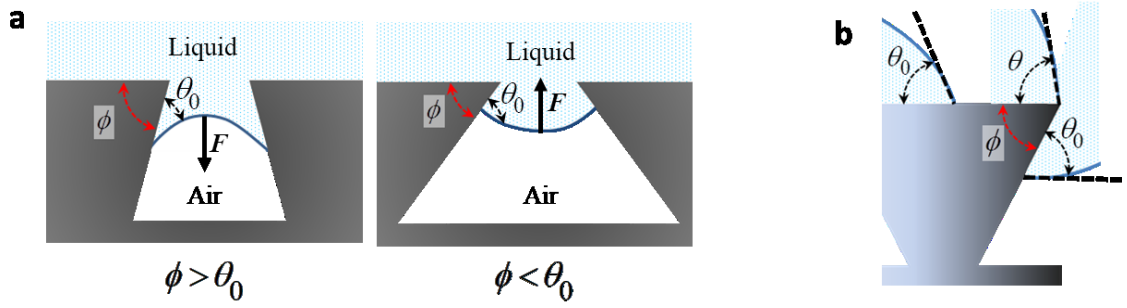

Figure 5.2| Wetting effects produced by sharp reentrant geometry in the superficial micro-textures. (a) Schematic representation of the capillary force favoring (left) or contrasting (right) liquid imbibition depending on the angle ϕ of the reentrant edge. (b) Sketch of the pinning effect of the sharp reentrant edges on a liquid drop.

Discrete superficial structures characterized by sharp and reentrant edges can be used also to control the directional spreading of liquids. The sharp edges, indeed, are able to constrain the contact angle of liquid drops to values that depends on the geometry of the edges. Gibbs constructed a geometrical relation, named Gibbs

inequality [123], which describes the range of possible contact angles of the liquid reaching the edge of a such sharp structure (Figure 5.2(b)):

$$\theta_0 \le \theta \le (180° - \phi) + \theta_0 , \tag{5.8}$$

where θ is the apparent equilibrium contact angle, ϕ is the edge angle of the microstructure measured respect to the horizontal axis and θ_0 is the Young's contact angle of the liquid on the surface. From relation (5.8), it follows that the upper limit for the contact angle θ onto structures having reentrant sharp edges ($\phi < 90°$) can approach 180°, regardless the actual value of the intrinsic contact angle θ_0, and even for liquids completely wetting the surface ($\theta_0 \approx 0°$). This effect suggests a strategy for designing spreading paths for liquids onto solid surfaces characterized by connected microstructures (for example parallel grooves) with an undercut height profile. Because of the pinning in the direction of the undercut, the liquid is free to propagate only in the directions of the connected structures [124]. However, the pinning strength of simple sharp edges is quite weak and it is easily destroyed by a small amount of vibrational energy provided to the system and in real applications multiple rather than a single parallel pinning edges are used.

5.1.3 Wetting anisotropy

The thermodynamic Wenzel and Cassie models discussed above concern the wetting behavior of isotropic rough surfaces, which induces an almost spherical shape for the liquid drop deposited over the surface and a nearly uniform contact angle observed from different directions of the contact line. However, if the texture of the solid surface has geometrical anisotropy, the shape of the contact line deviates from the circle and the observed contact angle varies along different directions over the surface ([125–128]). Such wetting anisotropy is not contemplated into the standard wettability models, which would predict a single value of the contact angle dependent only on the wetted area of solid surface and not on the actual asymmetric shape of the superficial architectures. A typical example of simple asymmetric roughness able to induce wetting anisotropy is constituted by parallel sinusoidal microgrooves. On such structures, the contact angle observed along the direction parallel to the grooves is larger than that measured along the perpendicular direction. In this simple situation, the observed wetting anisotropy can be qualitatively described by a thermodynamic model that takes into account the changes in the surface free energy induced by the asymmetric topography as the TCL

moves over the substrate along different directions. Here, the anisotropic wetting model proposed by Zhao et al. [126] is briefly illustrated.

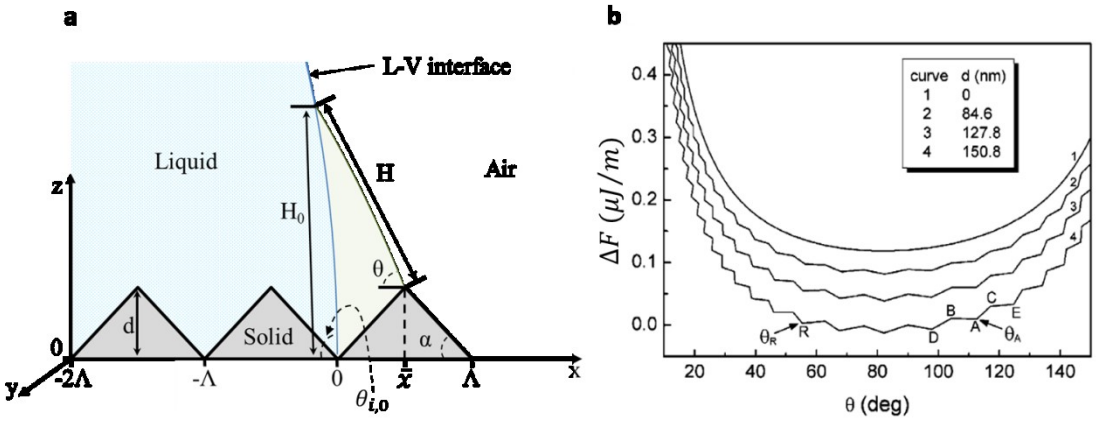

Figure 5.3| Wetting anisotropy model. (a) Schematic representation of the wetting situation defining the geometrical parameters used for the anisotropic wettability model. (b) Adaptation of the plot in ref [126] of the calculated free energy variation as function of the instantaneous contact angle. The parameters used for calculation were $\gamma_{LV} = 72.6$ mJ/m, $\theta_0 = 82°$, $H_0 = 2\ \mu m$ and $\Lambda = 396$ nm.

The situation describing a liquid drop wetting a rough substrate with one-dimensional asymmetric architectures (parallel grooves) is schematized in Figure 5.3(a). For simplicity, in the following calculations the sinusoidal grooved profile (of wavelength Λ) is substituted with isosceles triangles (Figure 5.3(a)), characterized by the geometrical angle α, defined by:

$$\tan\alpha = \frac{2d}{\Lambda}, \tag{5.9}$$

where d is the groove depth. In this model we assume that the initial state of the wetting, which corresponds to the initial contact of the drop with the surface, is characterized by an instantaneous contact angle $\theta_{i,0} = 90°$, observed in correspondence of the initial contact point of the TCL in $x = 0$ (schematized by the blue droplet profile in Figure 5.3(a)). After the contact, the TCL moves along the substrate and this motion is accompanied by a variation of the free energy of the system. Moving the TCL from the reference position at $x = 0$ to the position x (where the liquid-vapor interface is schematized by the gray profile in Figure 5.3(a)), the system free energy variation can be divided into two contributions:

$$\Delta F = \Delta F_1 + \Delta F_2 , \tag{5.10}$$

where ΔF_1 is the interfacial energy change due to the variation of the solid-vapor and solid-liquid interfacial areas, and ΔF_2 is the interfacial energy variation resulting from the change in the liquid-vapor interfacial area. Eventual gravity effects are neglected here. Explicitly, the two terms in (5.10) can be written (for the unit TCL length in the y direction) as:

$$\Delta F_1 = -\left(\gamma_{SV} - \gamma_{SL}\right)\frac{x}{\cos\alpha} \tag{5.11}$$

$$\Delta F_2 = \gamma_{LV}\Delta H , \tag{5.12}$$

where ΔH is the change in the length of the liquid-vapor interface, which cannot be calculated exactly. However, assuming that the size of the roughness is much smaller than the size of the droplet, the liquid-vapor interface can be approximated with a straight line in proximity of the contact line. In this approximation, as the liquid front moves in the x direction, the contact angle changes of a small quantity ($\theta = \theta_{i,0} + d\theta$) while the liquid-vapor interface remains straight and ΔH is given by

$$\Delta H = H - H_0 = \sqrt{\left(H_0 - z\right)^2 + x^2} - H_0 . \tag{5.13}$$

H_0 is the length of the initial liquid front (Figure 5.3(a)) and z is the height of the contact point situated in x. The z coordinate can be expressed in terms of x coordinate from geometrical considerations leading to the relation $z = z(x)$. Substituting into equation (5.10), the system free energy variation is expressed as:

$$\Delta F = -\gamma_{LV}\cos\theta_0\frac{x}{\cos\alpha} + \gamma_{LV}\left[\sqrt{\left(H_0 - z(x)\right)^2 + x^2} - H_0\right], \tag{5.14}$$

where θ_0 is the Young contact angle given by equation (5.1). The expression of the free energy given in equation (5.14) can be explicated in terms of the instantaneous contact angle $\theta = \theta(x)$ using geometrical considerations:

$$\tan\left[\theta(x)\right] = \frac{H_0 - z(x)}{x} . \tag{5.15}$$

Using the relations (5.9),(5.14) and (5.15), equation (5.14) can be calculated as function of the instantaneous contact angle and the geometrical parameters of the solid texture. The calculated behavior of ΔF, reproduced and adapted from the results reported in reference [126], is shown in Figure 5.3(b). In particular the different curves

correspond to the different values of the groove depth, at fixed period Λ. When $d = 0$, ΔF is a smooth curve of θ. However, when the groove pattern is not vanishing, a series of maxima and minima are observable. This implies that there are energy barriers, defined as the difference in the free energy between a local minimum and the adjacent maximum, the system encounters while the TCL moves in the direction perpendicular to the grooves. These energy barriers are associated to metastable states for the system, in which the actual observed contact angle can be forced to a particular value corresponding to one of the local minima in the free energy, even if this is not the global minimum in the system energy. As such energy barriers are not present for the TCL motion in the direction parallel to the grooves, a difference in the contact angle, as viewed from the two perpendicular directions of the substrate, arises. Such contact angle difference induces a deformation of the TCL and a directional wetting anisotropy onto asymmetric superficial roughness. As we will see in section 5.3, this framework can be used to interpret the wetting anisotropy observed onto the array of asymmetric micro-structures resulting from the light-reconfiguration process of the azopolymer pillar array.

5.2 The wetting state of the array of cylindrical azopolymer micro-pillars

From the discussion elaborated in the previous sections, the great influence of the superficial geometry in determining the wettability of the solid surface emerges clearly. With the aim of technological applications, the mass migration in azomaterials, being a smart and cost-effective tool for large-scale superficial patterning, is an attractive approach for the texture-based wettability engineering. The potentialities offered by the light-modulated surfaces have been already recognized with the anisotropic wetting induced by the sinusoidal SRGs [126], the reversible reconfiguration of superficial microposts [102] and the omniphobic behavior of some light-reconfigured structures [116,129]. However, the range of easily accessible applications based on this material platform is encouraging a great amount of new wettability studies. The results presented in the next sections of this chapter are framed in this trend of increasing interest toward the wettability studies. In particular, the wettability tailoring ability of the light-reconfigured azopolymer micropillars presented in chapter 1 is described here. Non-trivial wetting effects, as tunable wetting anisotropy or unidirectional liquid spreading will be presented as arising from the asymmetric reconfigured microstructures. This clearly demonstrates the versatility of the experimental framework

for practical applications. However, even the wetting state of the pristine structures resulted in a non-conventional wetting phenomenon where the observed contact angle onto the textures was determined by the TCL pinning rather than by the energy minimization of the standard wetting states. Part of the contents presented here have been published in the reference [12].

5.2.1 Water contact angle measurement

The wettability properties of the array of azopolymer micropillars are characterized by standard static contact angle measurements. The images of the drop profiles used for contact angle (CA) measurements are collected by a homemade optical setup, while their analysis is performed by the open source imageJ plugin DropAnalysis [130]. In the typical CA measurement, a 1,0 µL liquid droplet is carefully deposited onto the sample surface controlling the contact velocity with a mechanical translation stage. The digital image of the drop profile is collected about 5 s after the drop contact, in order to let the liquid relax and assume the equilibrium configuration. The temperature and the humidity of the room during the measurements were 23 °C and 50%, respectively. The contact angle values reported are the mean of at least three independent measurements in different regions of the samples.

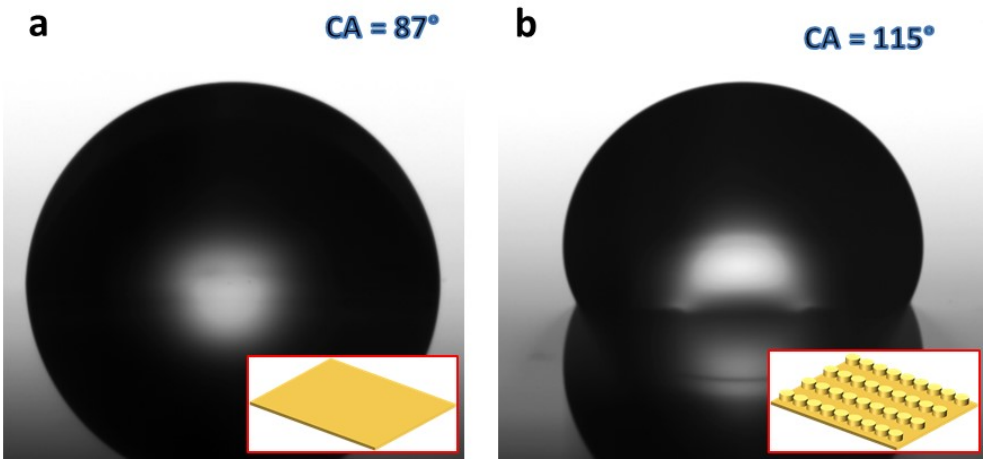

Figure 5.4| Water contact angle variation induced by the azopolymer pristine pillar texture. (a) Image of 1 µL water droplet deposited onto the flat azopolymer surface, resulting in the observed contact angle $\theta_0 = 87° \pm 3°$. (b) Image of the same volume of the water droplet cast onto the pristine azopolymer pillar array reported in Figure 4.6, showing the CA value $\theta = 115° \pm 3°$.

Figure 5.4(a) and Figure 5.4(b) show respectively the images of 1 μL water droplets deposited onto the flat untextured polymer surface and onto the cylindrical pillar array reported in Figure 4.6, with the relative measured contact angles. The micropillar superficial texture produced an increase of about 20° in the of the observed CA which passed from the value $\theta_0 = 87° \pm 3°$ measured onto the flat un-textured surface to value $\theta = 115° \pm 3°$ onto the patterned array, meaning a roughness-induced transition from the hydrophilic regime (CA < 90°) of the flat surface to the hydrophobic regime (CA > 90°).

In order to explain the observed contact angle, the wetting state of the azopolymer textured surface are first assessed by comparing the measured water contact angle θ with the values predicted by the standard Wenzel and Cassie–Baxter models, specified for the actual pillar geometry. However, neither of them adequately describes the experimental observed contact angle. In particular, as discussed in section 5.1.1, the superficial roughness in the Wenzel model always enhance the intrinsic hydrophilic/hydrophobic behavior of the flat surface, and equation (5.3) does not contemplate the geometrically-driven transition from the hydrophilic to the hydrophobic regime observed in Figure 5.4. Such a transition would be, in principle, allowed in the Cassie-Baxter model, where the liquid droplet lies suspended on the composite solid/air interface formed by the solid surface and the air trapped into the roughness asperities. However, no evidence of such air gaps can be seen from Figure 5.4(b), which instead suggests a wetted regime. The discrepancy of the CA value predicted by the Cassie-Baxter model for the actual pillar geometry (significantly higher than that observed one), and the experimental absence of droplet roll-off at any tilt angle, meaning high CA hysteresis, confirms the inadequacy of this model too.

The experimental framework can be, instead, properly explained by assuming the triple-phase contact line pinning rather than the minimization of the system energy in the wetted superficial area as governing the actual wetting situation, as described in the next section.

5.2.2 The pinning model

Recently Suzuki and Ueno [131], proposed a new set of equations able to describe the observed static contact angle of liquid droplets lying in the wetted regime onto surfaces with controlled micro-textures (pillars, grooves and holes). The model assumes, differently from the thermodynamical standard models, that the liquid contact angle depends only on the forces able to pin the TCL rather than on the minimization of the

system energy in the wetted sample area. From this assumption, the authors established, for the description of the apparent static contact angle θ, a relation between the contact angle θ_0 that the liquid shows on the ideally flat surface of the same material, the geometrical parameters of the texture, and the ability of the sharp edges of superficial textures in pinning the TCL. This pinning ability can be quantified by a pinning angle θ_1, defined by the balance of the forces acting on the unit length of the TCL pinned at the edge of the top flat surface of the micron-sized three-dimensional structure.
From Figure 5.5(a), the force balance for the unit length of the TCL in the horizontal axis can be written as:

$$-\gamma_{LV}\cos\theta_1 = \gamma_{SL}\,, \tag{5.16}$$

from which it follows

$$\cos\theta_1 = -\frac{\gamma_{SL}}{\gamma_{LV}}\,. \tag{5.17}$$

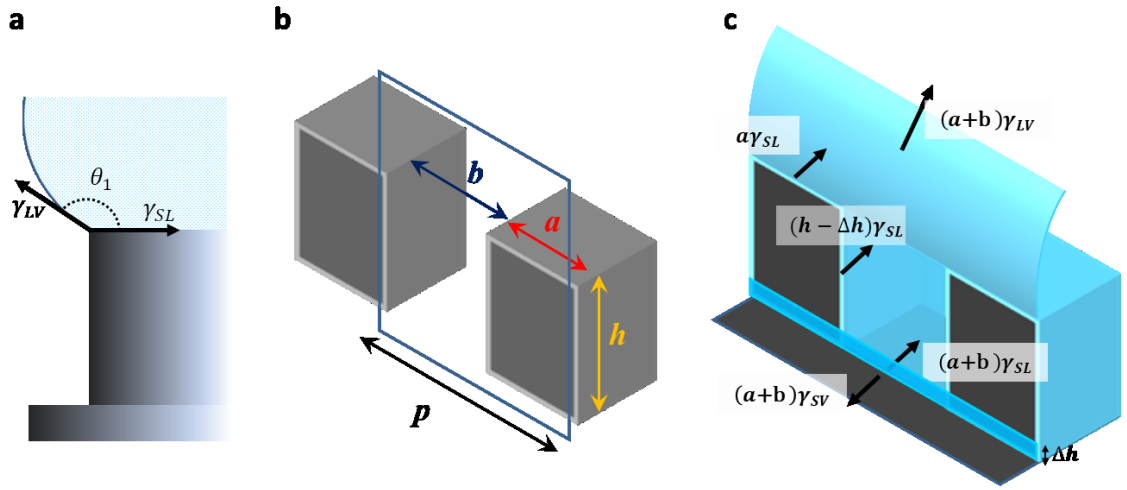

Figure 5.5| Definition of the pinning model parameters. (a) Sketch defining the pinning angle by the equilibrium of the interfacial tensions at the sharp edge of the structure. (b) Description of the of the unitary cell geometrical parameters of the square pillar array used for the derivation of the equation (5.19). (c) Schematic representation of the liquid pinned at pillar edges together with the direction of the interfacial forces acting onto the TCL in the unitary cell.

The relation (5.17), defines the pinning angle as the ratio of the solid-liquid and liquid-vapor interfacial tension, and can be interpreted as the angle of a liquid film pinned at the edge of one ideally infinite long groove of the considered material.

The same argument about the force equilibrium experienced by the TCL unit length can be used to define the static contact angle θ of al liquid droplet deposited onto the

pillar patterned surface. In Figure 5.5(b), the unit cell of an array of square pillars characterized by width a, inter-pillars gap b and pillar height h is presented. For simplicity it is assumed that only one lateral face of the pillar is not completely covered by the liquid (the gray face in Figure 5.5(c)), and that the liquid is allowed to go around the bottom base of the pillar, wetting this face for a small height Δh that will tend to zero in the following calculations (schematized with the narrow liquid film at the bottom base of the pillar in Figure 5.5(c)). From Figure 5.5(c), the equilibrium of forces acting on the TCL in the horizontal direction is written as:

$$-(a+b)\gamma_{LV}\cos\theta+(a+b)\gamma_{SV}=(a+b)\gamma_{SL}+a\gamma_{SL}+2(h-\Delta h)\gamma_{SL}. \quad (5.18)$$

For $\Delta h \to 0$, using the Young relation and the definition of cos θ_1, equation (5.18) can be rewritten as

$$\cos\theta=\cos\theta_0+\frac{a+2h}{a+b}\cos\theta_1, \quad (5.19)$$

which defines the relation between the observed contact angle θ, the surface geometrical parameters and the pinning angle. For the application of the model to the cylindrical azopolymer microposts, equation (5.19) has to be specified for the actual experimental situation of water droplets deposited onto the pristine azopolymer micropillar array.

The first parameter to be determined is the pinning angle θ_1. In particular, from equation (5.17), the determination of the angle θ_1 needs the evaluation of the solid-liquid interfacial tension γ_{SL} of the analyzed material. According to literature [132], a direct estimation of γ_{SV} can be obtained by measuring the contact angles of polar and non-polar liquids onto the same flat solid surface. In our case, the used liquids were water (polar) and Diiodomethane (CH_2I_2) (non-polar). The images of the 1 μL sessile liquid droplets together with the measured CA are presented in Figure 5.6(a) and (b), respectively. From the static CA measurements and the relative elaboration, the measured γ_{SV} gave the value (estimated by the control software of the commercial tensiometer Dataphysics OCA 20, used in this specific measuremet) $\gamma_{SV} = (48.1 \pm 0.5)\ mN/m$, which permitted the estimation of the solid-liquid interfacial tension $\gamma_{SL} = 39 \pm 3\ mN/m$ from the Young relation. Equation (5.19) with the measured γ_{SL} provides the value $\theta_1 = 122.5° \pm 0.1°$ for the pinning angle. For comparison, the direct measurement of θ_1 as the CA of 1 μL of a water droplet onto parallel azopolymer grooves (width 50 μm, pitch 100 μm and height 10μm) presented in Figure 5.6(c), gave

a value of $\theta_{1,m} = 124° \pm 3°$ (Figure 5.6(d)), in accordance with the predicted value obtained from the interfacial tension measurements.

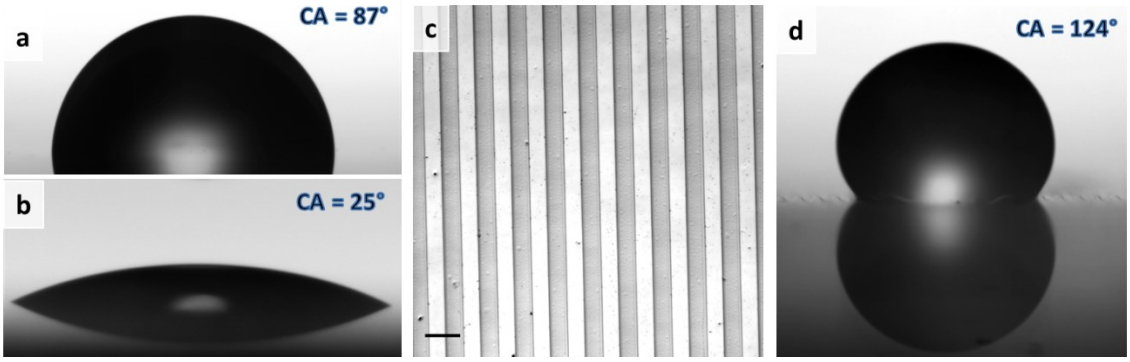

Figure 5.6| Estimate of the pinning angle for our azopolymer. (a) and (b) images of 1 µL droplet profiles defining the CA, respectively, for water and Diiodomethane onto the flat azopolymer surface. (c) Optical micrograph of parallel grooves patterned onto the azopolymer surface (scalebar 100 µm). (d) Orthogonal water contact angle of 1 µl water droplet deposited onto the parallel groove of panel (c).

The observation of the TCL of a water droplet deposited onto the pristine posts by means of the optical microscope shown in Figure 5.7(a) suggests that, at the equilibrium, the TCL pins at the diameter of the pillars. This observation permits to approximately relate the geometrical parameters of the cylindrical texture to the geometrical parameters of the pinning model. In particular, the parameter a in the equation (5.19) can be substituted with the pillar diameter d, while the parameter b became the gap between pillars, measured along the direction of the line joining two neighbor pillar centers (Figure 5.7(b)). Using the pitch $p = d + b$ of the array, equation (5.19) is then written as:

$$\cos\theta = \cos\theta_0 + \frac{d+2h}{p}\cos\theta_1 . \qquad (5.20)$$

Equation (5.20) describes the observed CA for the array of cylindrical microposts in the approximated TCL geometrical configuration described above, which provides the estimated CA value of $\theta_1 = 122.5° \pm 0.1°$, using the geometrical parameters of the azopolymer pillar array $(d = (4.5 \pm 0.1)\mu m;\quad b = (5.3 \pm 0.1)\,\mu m;\quad h = (2.0 \pm 0.1)\mu m)$, the measured $\theta_0 = 87° \pm 3°$ and estimated pinning angle $\theta_1 = 122.5° \pm 0.1°$. The estimated value θ_{calc} has to be compared with the measured $\theta_{meas} = 115° \pm 3°$ of Figure 5.4(b). The agreement between θ_{calc} and θ_{meas} implies that the model fully

explains the observed contact angle even in this simplified application, where the actual shape of the TCL at pillar edges in not taken into account. A possible generalization could include also this contribution, considering for example the length of the semi-circumference of the circular pillar instead of the pillar diameter for the parameter a (d), however no significant variation in the estimated CA were found (operating the substitution $d \rightarrow \frac{\pi}{2} d$ in the equations; $\theta_{calc,extention} = 115° \pm 3°$) and the agreement with the experimental data is verified as well.

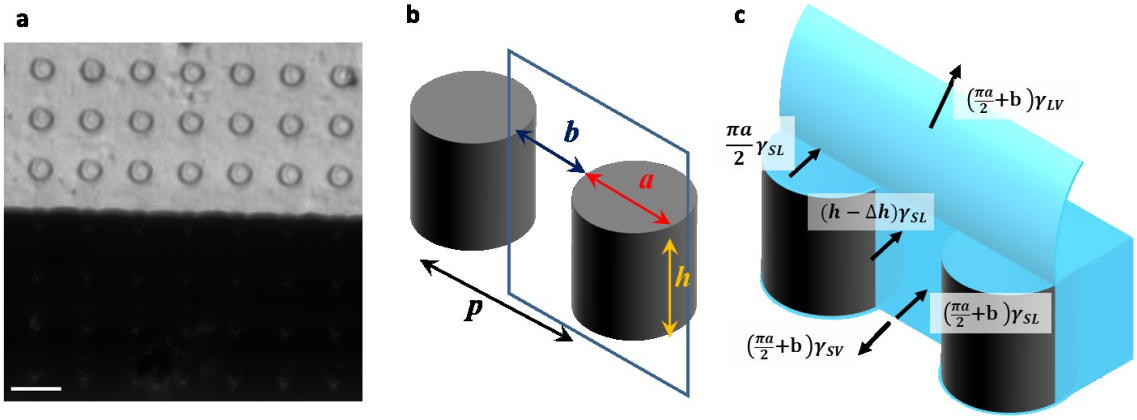

Figure 5.7| (a) Bright-field optical micrograph of a section of the TCL pinned at pillar edges, The image is collected by an inverted microscope equipped with 40X objective. Scale bar 10 μm. (b) Geometrical description and (c) application of the model to the cylindrical pillar array assuming the TCL pinned along the line connecting two closest neighbor pillars.

The quantitative agreement of the observed CA with the value obtained from the pinned model, together with the discrepancy between the observed and the CA values predicted by the thermodinamical models, unambiguously recognizes the TCL as governing the wetting behavior of our pristine azopolymer micro-pillars.

5.3 Light-induced wetting anisotropy

As demonstrated in the section 4.2.3, significant directional anisotropy can be inscribed in the tridimensional superficial roughness by illuminating the pristine azopolymer array with linearly polarized light. From the discussion made in section 5.1.3, it becomes also clear how such asymmetric textures are able to induce wetting anisotropy over the surface. Indeed, the three-dimensional architectures constituted by the light-

reconfigured posts induce directional energy barriers for the pinning and the motion of the TCL of a liquid droplet deposited onto the texture, acting analogously to the parallel grooves described by the anisotropic wetting model [126]. A consequent obvious directional dependence of the CA observed along different directions of reconfigured array is also found. However, as the structural asymmetry of the light-reconfigured structures depends on the actual illumination conditions, and can be easily modified by controlling few trivial illumination parameters, also does the anisotropic wetting behavior of such textured surfaces.

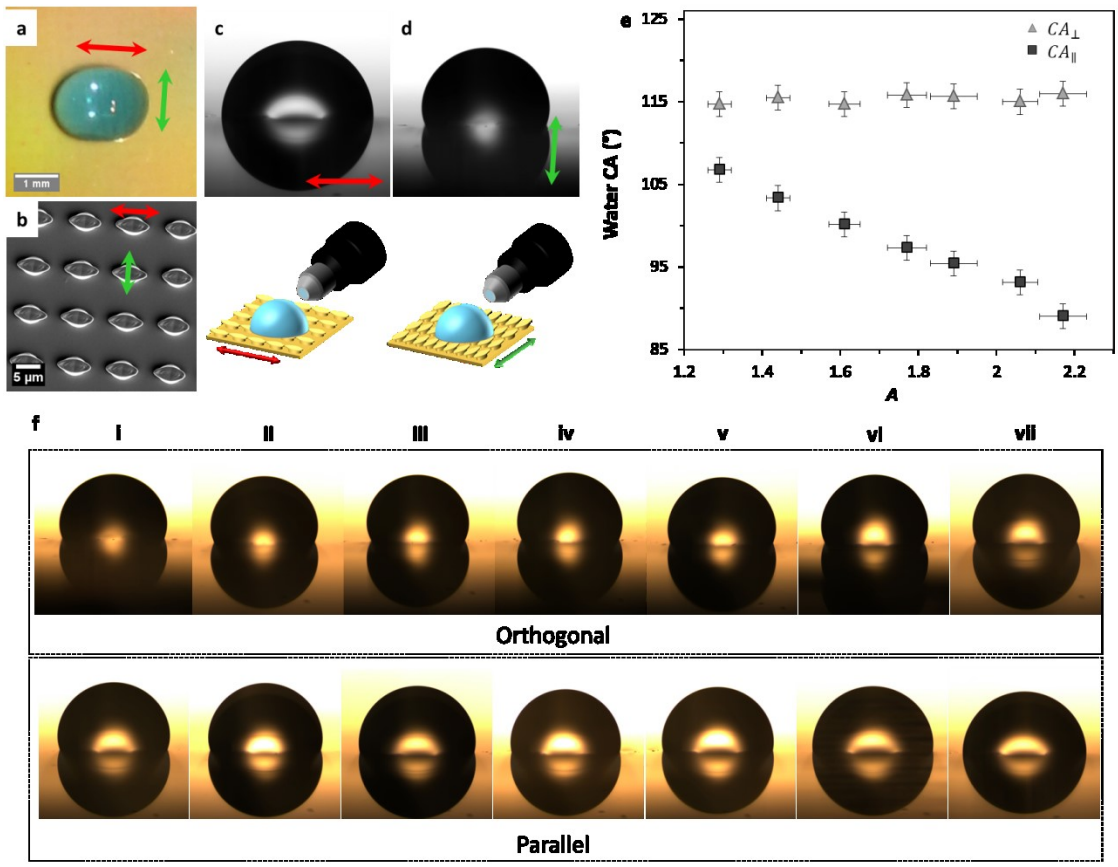

Figure 5.8| Wetting anisotropy on the light-reconfigured azopolymer micropillars. (a) Anisotropic water droplet deposited onto the asymmetric pillars presented in (b). The red and green arrows represent the directions of the long and short axes of the reshaped structures, respectively. (c and d) Side views of the droplet in the direction parallel (red) and orthogonal (green) to the asymmetric pillars. (e) Parallel ($CA_\parallel$) and orthogonal ($CA_\perp$) water contact angles measured for different values of the texture asymmetry *A*. (f) Images of the orthogonal and parallel profiles of 1µL water droplets deposited onto the azopolymer arrays presented in Figure 4.9(c).

In particular, in the situation of linear polarized light irradiating the pristine array at normal incidence, the reconfigured structured are characterized by "pseudo-elliptic" geometry (Figure 4.8(a-b) and Figure 4.9). Then, in the light of the anisotropic wetting model, the directions of the sample parallel to the long axis of the asymmetric micro-structures are characterized by smaller energy barriers to the liquid propagation. The TCL motion in these directions is energetically favored with respect to the motion in the orthogonal ones. As a consequence, the TCL results mainly elongated in the direction of the long axis of the reconfigured structures, as reported in Figure 5.8(a). This image shows the photograph of a sessile water droplet (with blue dye) deposited onto the reconfigured asymmetric pillar array reported in Figure 5.8(b). The red and green arrows indicate, respectively, the directions parallel and perpendicular to the illuminating light polarization that correspond to elongation (red arrow) and pinning (green arrow) directions of the drop TCL.

The level of induced droplet TCL anisotropy depends on the degree of asymmetry in the light-reshaped superficial micro-pillars. This wetting anisotropy can be characterized by the differences of the water CA measured in the long (*parallel* CA, Figure 5.8(c)) and the short (*orthogonal* CA, Figure 5.8(d)) axis directions of the reshaped pillar as function of the measured mean asymmetry A in the superficial micro-structures. Figure 5.8(e) reports the parallel and the orthogonal contact angles of 1 μL water droplet deposited onto the sequence of light-reconfigured microstructures described in Figure 4.9, having different superficial degree of asymmetry as consequence of different light exposure time.

Table 5.1| Data of the wettability anisotropy at varying light-induced superficial asymmetry. The contact angle measurement reported on each sample is relative to the corresponding array of Figure 4.9 and Table 4.1.

Array	Pillar asymmetry	Orthogonal CA	Parallel CA
i	1.29 ± 0.05	116° ± 3°	107° ± 3°
ii	1.44 ± 0.07	115° ± 3°	103° ± 3°
iii	1.61 ± 0.08	116° ± 3°	100° ± 3°
iv	1.8 ± 0.1	116° ± 3°	97° ± 3°
v	1.9 ± 0.1	115° ± 3°	95° ± 3°
vi	2.0 ± 0.1	115° ± 3°	93° ± 3°
vii	2.2 ± 0.1	115° ± 3°	89° ± 3°

From the contact angle measurements, no significant dependence of the orthogonal the orthogonal ($CA_{\perp}$, Figure 5.8(e)) on the structure asymmetry was found, since the

measured values at different degrees of structural asymmetry remain unchanged (within the experimental measurement errors) with respect to the pristine pillar array. These values are about 115° regardless of the actual value of the superficial asymmetry. This behavior can be explained with the small contraction of the pillars in the short axis direction after the post reconfiguration described (in section 4.2.4), not producing significant structural modifications and hence any decrease of the energetic barriers for the TCL motion in that direction.

The measured parallel contact angle ($CA_{//}$, Figure 5.8(e)) shows instead a strong dependence on the pillar asymmetry A. As expected from energy barrier considerations, higher values of A induce a decrease of the observed contact angle in the parallel direction. A variation of about 20° is found in parallel $CA_{//}$ by increasing the posts asymmetry from 1.3 to 2.1, following an approximately linear trend. For greater clarity, the image sequence of the water droplet profiles data in the direction of the long and short axes of the reshaped pillars and the relative wetting anisotropy data are reported in the image sequence of Figure 5.8(f) and in Table 5.1, respectively.

5.4 Unidirectional and bidimensional wetting anisotropy

In section 4.2.6, the peculiar slanted geometry of the azopolymer pillars reconfigured with linear light polarization and non-zero incidence angle was presented. These asymmetric structures are characterized by a unidirectional superficial asymmetry (Figure 5.9(a)), which can be directly translated into a unidirectional wetting anisotropy. Also in this case indeed, because of the directional dependence of the energy barriers for the spreading over the substrate, a liquid droplet deposited on the reshaped structures assumes an asymmetric TCL along the deformation direction. However, the slanted reconfigured architectures introduce a further energy difference in the azopolymer array along the direction of the structural tilt. This non-trivial wettability behavior is shown in Figure 5.9(b), where the image of a 2 µL water droplet (with 0.1 wt % Triton X-100 surfactant) deposited on the tilted structures is presented. In this experiment, the droplet, after the contact with the asymmetric substrate, becomes elongated toward the reconfigured pillar slant direction ,with a measured contact angle difference of about 25°. Such unidirectional wetting anisotropy is one of the situations where the use of the light-reconfigurable shows all its potentiality in the wetting related experiments. Similar effects, which actually mimics the wetting behavior of butterfly wings [133], is achieved with complex approaches, which typically requires also multiple fabrication steps [103–106,134].

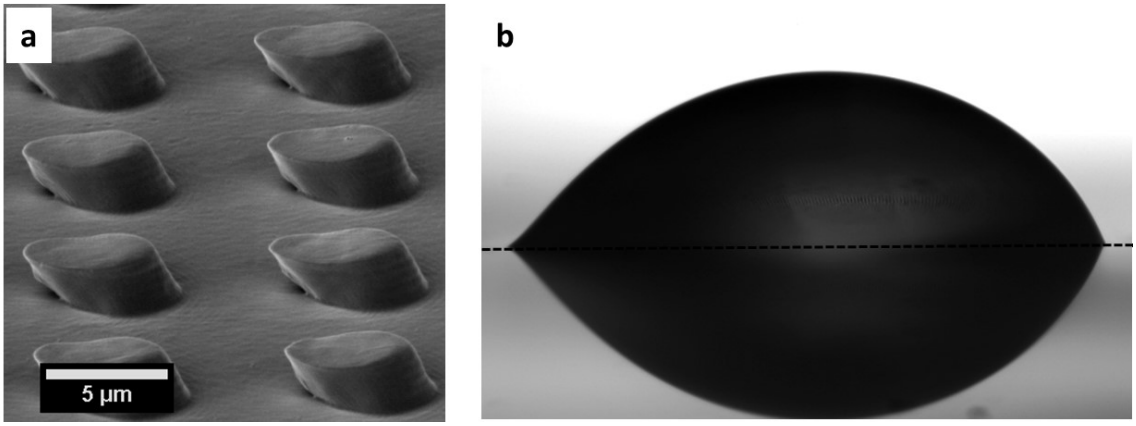

Figure 5.9| Left−right contact angle asymmetry induced by the reconfigured tilted pillars. (a) SEM side-view image of the tilted light-reconfigured pillars. (b) Image of 2 µL water droplet with surfactant Triton X-100, 0.1 wt %, deposited onto the slanted pillar array. The measured contact angles are $CA_{Left} = 40°$ and $CA_{Right} = 65°$.

The dependence of the induced asymmetry direction in the light-reconfigured microposts on the polarization direction of the illuminating beam can be used to design a 2D asymmetry pattern on the same pristine pillar array. This can be achieved, in principle, by illuminating the sample with a pure 2D spatially varying polarization pattern or with sequential spatially structured illumination intensity distributions, coupled with a controlled polarization state. Such a bidimensional asymmetry translates into the bidimensional modification of the wetting behavior of the reconfigured azopolymer substrate, giving the possibility of designing different liquid drop shapes and orientations in the illuminated areas of the same pristine array. An example of a pure polarization bidimensional pattern is given by a configuration based on radial (R) or azimuthal (A) polarization states, in which the optical electric field of the light beam oscillates in a direction that is radial or azimuthal respect to the center of the spot [55,62]. R and A polarizations can be obtained through the *θ-cell* which, as discussed in detail in section 2.2.2, is able to transform the linear polarization of the light beam in both R and A polarization states, depending on the direction of the original linear polarization with respect to the θ-cell axis.

Radial and azimuthal reconfigurations of azopolymer pillars are realized by illumination of the prepatterned area (1 cm × 1 cm wide) with the properly modulated laser beam emerging from the θ-cell. The experimental setup is schematized in Figure 5.10(a), which differs from the setup used for the reconfiguration experiments reported

until now (Figure 4.7) only for the insertion of the polarization modulator along the beam path. The representations of the optical field configurations for R and A polarizations in the two experiments are shown in Figure 5.10(a) and (b), while the optical bright-field microscope images of the reconfigured pillars in different regions of the illuminated sample are shown in Figure 5.10(c) and Figure 5.10(e), respectively.

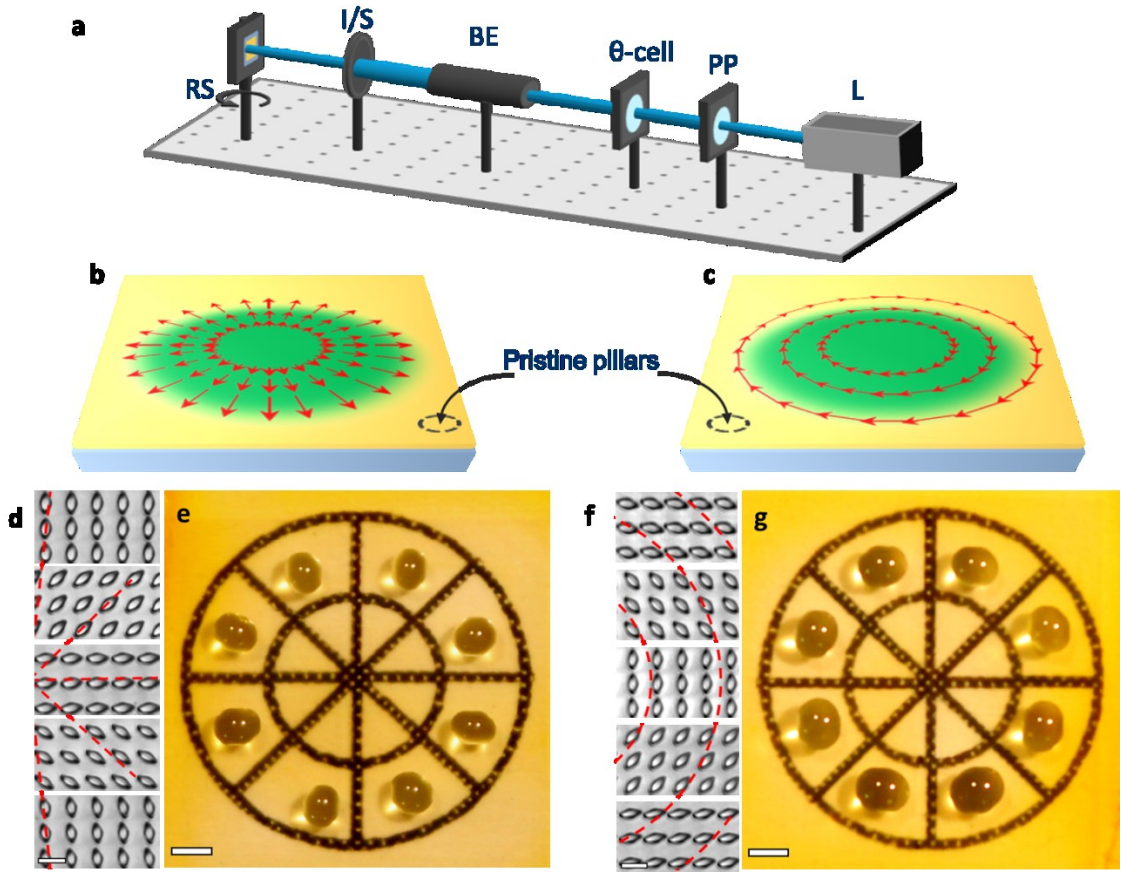

Figure 5.10| Radial and Azimuthal wettability patterns. (b) and (c) schematic representation of the illumination configuration for R and A polarization, respectively. (d) micrographs of different regions of the array, reshaped with the radially polarized beam (scalebare 10 μm). The red dotted lines schematize the light polarization direction during the one-step reconfiguration process. (e) Photograph of the liquid droplet placed in different regions of the radially reconfigured array (Scale bar 1 mm). The droplets are elongated toward the center of the illuminated region in radial directions. (f) Micrographs and (g) photograph of the same experimental situation for azimuthal polarization of the illuminating beam.

As far as the oscillation direction of the electric field can be locally approximated as linear for both R and A polarizations, neighboring pillars are deformed approximately in the same direction (this is more true as the distance from the beam center increases) as

shown in each subpanel of Figure 4(d) and Figure 4(f). However, the deformation direction significantly changes in the millimeter-scale, and the long axis of the reconfigured pillars properly orients in order to reproduce the radial or the azimuthal pattern of the illuminating beam polarizations.

The induced two-dimensional wetting anisotropy of the reconfigured arrays is clearly observed from the photographs in Figure 5.10(d) and Figure 5.10(f), where the droplets of an ionic liquid (1-butyl-3-methylimidazolium iodide) deposited onto the reconfigured samples at fixed distance from the center are shown. The liquid droplets become anisotropically elongated in the direction of the local long axis of the reshaped posts, which varies angularly across the sample and globally reconstructs the two-dimensional radial and azimuthal patterns.

Since the light-driven reconfiguration is induced only in the illuminated regions of the pristine cylindrical azopolymer pillars, a spatially modulated intensity of the illuminating beam can be used to induce surface asymmetries with spatial selectivity. As a consequence, a two-dimensional wetting anisotropy path can be in principle arbitrarily designed onto the pillar array using a proper combination of incidence angle, polarization state, and spatial distribution of the light intensity. The proof of concept of the droplet TCL deformation path design is demonstrated in the simple experimental situation illustrated in Figure 5.11. Here, a single pristine pillar array is illuminated in three different regions by a laser beam which is spatially cut by a rectangular slit in a stripe of light about 2 mm wide. This constitutes the prototype of a simple structured intensity pattern. The polarization and the incidence angle of the illuminating beam are tuned to achieve different reconfigured pillar geometries in each illuminated rectangular sample area (marked by the blue rectangle and labeled with progressive numbers). Figure 5.11(a) and Figure 5.11(b) show, respectively, the illumination scheme and the optical micrographs of the reshaped pillars in each area. The laser polarization direction is indicated by the red arrows in the relative numbered box. In particular, areas 1 and 2 are illuminated at normal incidence angle, while area 3 is illuminated at an incidence angle of 45° and the slanted pillar elongation direction is schematized by the one-directional arrow pointing toward the left in the light polarization direction. Each of the illuminated regions has a defined directional asymmetry (Figure 5.11(c)) due to the different reconfiguration conditions which directly translates in position dependent liquid droplet anisotropy over the pillar array. Despite the very simple illumination condition shown here, more complex intensity/polarization combinations can be easily conceived and experimentally realized, giving the possibility of exploiting the light-driven mass migration phenomenon in azobenzene-containing materials to effectively

draw complex anisotropic bidimensional wetting distributions on single prepatterned macroscopic regions.

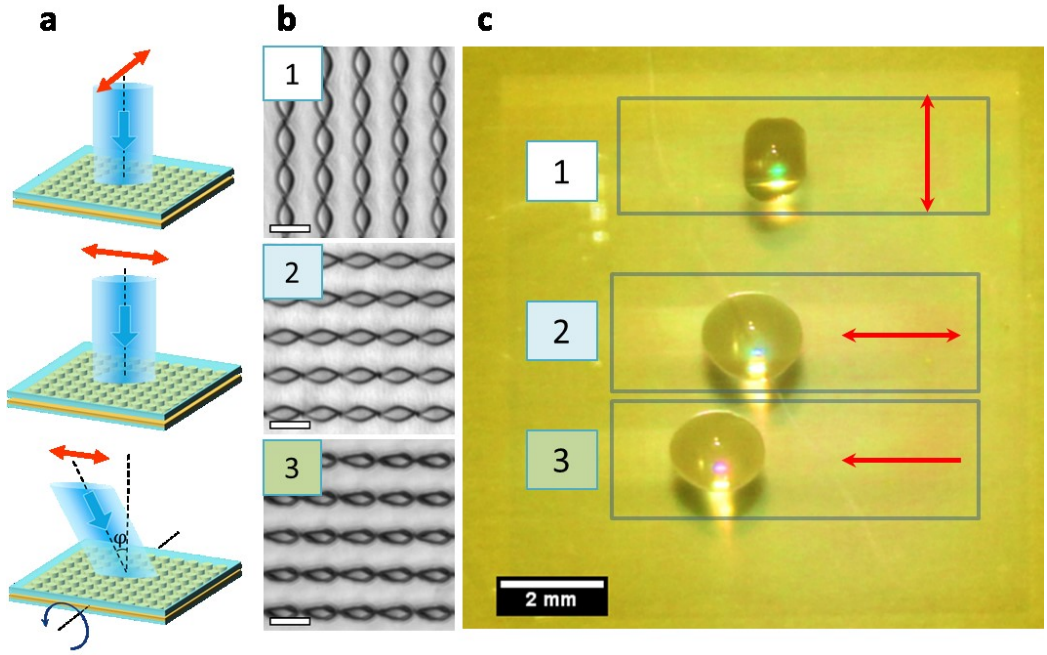

Figure 5.11| Two-dimensional wettability path induced by polarization/intensity light patterns. (a) Schematic representation of the illumination configuration in each reconfigured area of the azopolymer array. (b) Optical micrographs of the different reconfigured pillar areas. (c) Photograph of the water droplets deposited in the relative numbered regions. The red double arrows of regions 1 and 2 represent the direction of the linear light polarization at normal incidence, while the single arrow in region 3 indicates a nonzero incidence angle producing pillars elongated in the direction of the arrow.

5.5 Anisotropic liquid spreading

The anisotropic wetting effects induced by the asymmetric geometries of the light-reconfigured posts can be even enhanced by a chemical modification of the azopolymer surface. For example, a superficial hydrophilization treatment of the reshaped posts is able to turn the directional wetting anisotropy in a directional spreading of water droplets. Oxygen plasma treatment is a commonly used technique for modification of organic polymer surfaces to induce or enhance hydrophilicity [135–137]. By means of this treatment, aliphatic and/or aromatic carbon on the surface can be readily oxidized to functional groups with C-O and/or C=O bonds such as alcohol, ketone, and carboxylic acid derivatives. These groups are responsible for the induced polarity of the exposed

polymer surface and increased hydrophilicity. As a proof, Figure 5.12 shows the photographs of the spreading of water droplets resulting from the O_2-plasma hydrophilization treatment of the pillar array after the light-reconfiguration process.

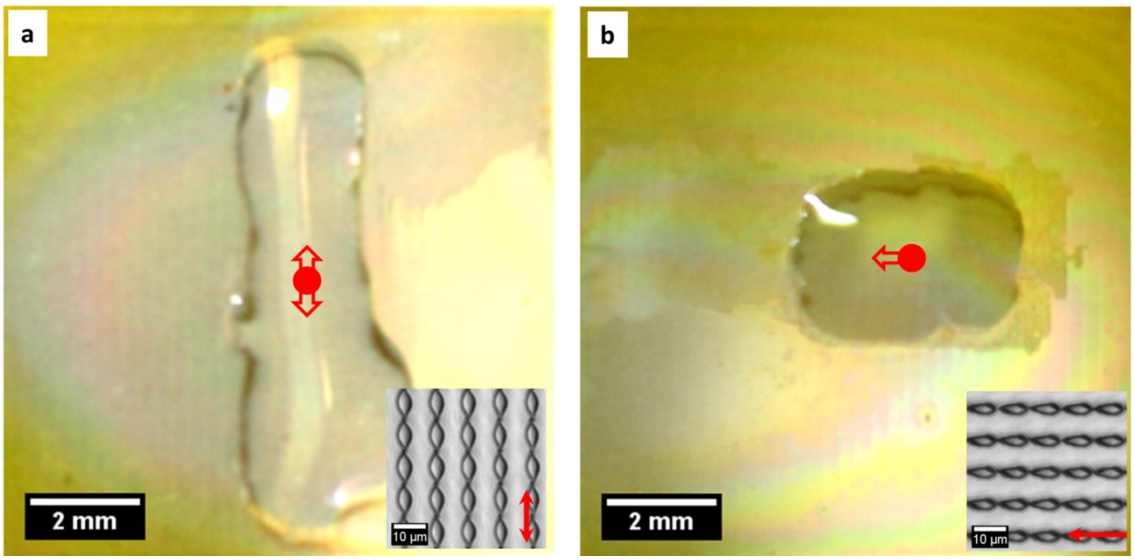

Figure 5.12| Directional liquid spreading on O2-plasma treated surfaces (15 W, 5 sccm, 1 min). (a) Symmetrically spreading droplet onto the symmetric reshaped pillars (optical micrographs in the inset). (b) Unidirectional droplet spreading in the direction of the slanted reconfigured pillars presented in the inset. The red spot represent the initial position of the droplets which then propagate mainly in the directions marked by the arrows.

In particular, the posts in Figure 5.12(a) are reshaped with linear polarization at normal incidence angle, which results in the symmetrically elongated structures shown in the inset. The liquid volume, initially dispensed in the position indicated by the red spot, flows symmetrically in the direction of the red arrows, which corresponds to the direction of the long axis of the reconfigured microposts. Despite the fact that the surface is made homogeneously superhydrophilic by the plasma treatment, the stronger energy barrier arising in the direction of the short axis is able to pin the spreading TCL along an approximately straight line parallel to the long pillar axis. As a consequence, a symmetric directional spreading is observed in the pillar long axis direction and hence in the illuminating light polarization direction. Unidirectional liquid spreading (Figure 5.12(b)) is instead achieved onto the tilted pillar structures, reconfigured at the laser incidence angle $\varphi = 45°$ (inset). Also in this case the water droplet spreads in the direction of the pillar deformation axis (which corresponds to the light polarization direction), but the liquid flows mainly toward the tilted side of the reconfigured pillars

and gives rise to a unidirectional liquid spreading. This asymmetric spreading behavior is even more highlighted by the thin liquid film propagating ahead to the droplet volume, which spreads on the left side of the droplet until it reaches the edges of the textured array, while it soon results in being pinned on the right side. Moreover, these results, coupled with the capability of the wetting path design demonstrated in Figure 5.11, suggest that the light reconfigured azopolymer microtextures can be used also to delineate bidimensional spreading pathways.

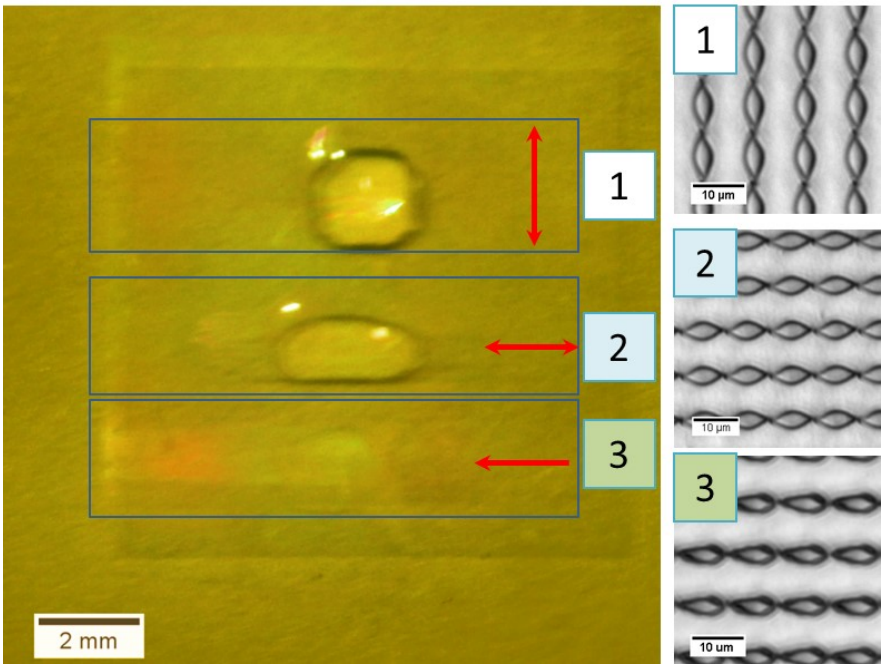

Figure 5.13| Two-dimensional liquid spreading pathways. (a) Photograph of three spreading water droplets placed in different reshaped regions (b) of the O_2-plasma treated azopolymer micro-pillar array. The liquid spreading direction follows the asymmetric geometries of the underlying micro-structures, while the deformation discontinuities at the boundaries of the illuminated regions are able to pin the liquid in the specific directions.

Figure 5.13 presents the photograph of three water droplet, showing different spreading behavior in different reconfigured areas of an oxygen plasma treated pillar array. The reconfiguration geometry is the same as described in Figure 5.11, while the anisotropy produced by the light-induced directional roughness of the texture is enhanced by the superficial hydrophylization treatment. In particular, the droplet in the region 1 spreads in the vertical direction and becomes pinned at the boundaries of the illuminated sample area. As a result only a small distance is covered in the vertical direction by the spreading liquid in region 1. The droplet in region 2 follows the pillar

deformation in the horizontal direction which produces a pronounced liquid spreading in the same direction. In this case, the liquid spreading is hampered along the vertical direction by the energy barriers arising in the short axis direction of the reshaped pillars, while the liquid propagation is favored along the horizontal direction. The same situation is realized in region 3, where the further left-right asymmetry in the slanted pillar geometry results in the uni-directional liquid spreading toward the left side of the illuminated region.

These results, together with all the results discussed in previous sections of the present chapter, prove that the light-induced superficial reconfiguration of azomaterials represents a valid strategy to tailor the wetting properties of the solid surfaces. The use of these materials, and the versatility that the light induced mass migration offers in deterministically determining the final surface architecture, has enormous advantages with respect to the standard lithographic techniques typically used for the fabrication of surfaces in wettability studies. These advantages are related to the very simple fabrication process of the pristine structures and to the possibility to tailor at need the superficial geometry by controlling few illumination parameters. Furthermore, the possibility to further tuning the solid surfaces once fabricated, the dramatic reduction of the fabrication costs and the possibility to transfer the light-reconfigured texture onto other materials having specific chemical nature suitable for specific applications, make the azomaterials a fundamental platform for the next step toward both applications and fundamental studies in the field of geometry-based wettability of solid surfaces.

Conclusions

The results presented in this thesis demonstrate that the light-induced mass migration phenomenon occurring in azomaterial films under the irradiation of Uv/visible light patterns can be effectively used to induce complex superficial topographies.

In Chapter 2 has been described the mass migration phenomenological model introduced few years ago to rationalize the spiral-shaped surface reliefs inscribed onto the surface of an azopolymer. These surface reliefs emerge whenever the azopolymer film is irradiated by a focused Laguerre-Gauss beam, which has an optical vortex along its propagation axis. The model ascribes the sensitivity to the beam wavefront, necessary for the correct description of the spiral mass migration, to a surface mediated interference between the complex distributions of the optical field components generated in the focal region of high NA microscope objective. In Chapter 2, two situations have been presented where the agreement between the superficial modulations, predicted by the model for a given hypothesized optical field distribution, and the experimentally observed surface reliefs are used for an indirect characterization of two light modulating devices. The first device is a dielectric metasurface, able to covert spin angular momentum into orbital angular momentum of light. This device is expected to produce a beam with an optical vortex. Hence, the spiral surface reliefs are predicted to arise by the phenomenological model onto the surface the azopolymer film. The actual observation of these spirals has allowed providing an alternative and elegant characterization of the device, attesting successful design and fabrication strategies. The second device is the liquid crystal θ-cell polarization converter, which is able to produce radially and azimuthally polarized beams. However, because of the fabrication process, the device introduces also a phase-shift in the modulated beam, which affects the field distribution of this beam in the focal plane of high NA microscope objective. The agreement observed also in this case between the surface reliefs predicted by the model in this irradiation configuration and the experimental surface reliefs inscribed (and reported for the first time in this thesis), onto the azopolymer film, allows to further confirm the actual distribution of the field components generated in the modulation of a light beam with a θ-cell converter.

In the thesis, moreover, two different main strategies have been exploited to enlarge the range of possible textures obtainable onto the surface of azopolymer films in different irradiation conditions.

The first approach, described in Chapter 3, deals with the illumination of the flat surface of the azopolymer film with holographic spatially structured intensity patterns. These are realized through the use of phase-only computer-generated holograms, able to achieve almost any arbitrary light distributions in the azopolymer surface plane. The calculation of such holograms is based on the Fourier relations existing between the focal planes of a lens realizing the 2f-geometry configuration. In this configuration, once that the desired complex intensity pattern is specified by a digital grayscale image, a calculation algorithm provides an hologram which is directly related to the phase profile of the Fourier transform of the target intensity distribution. The effective power of such optical scheme is fully accomplished by the use of a computer controlled spatial light modulator to realize the actual beam modulation. This device is the core of the optical setup we used for the reconstruction of complex intensity light patterns. Beside the precise and arbitrary control of the light distribution over the azopolymer film, the illumination scheme based on the computer-generated holograms has also another fundamental advantage with respect to the standard interference scheme typically used for the surface relief inscription onto the azomaterials. This is the possibility to control, in a completely independent way, the intensity pattern and the polarization state of the light field illuminating the azopolymer. A similar feature can also play a crucial role in the study of the intricate fundamental aspects of the light-induced mass migration phenomenon. In the results reported in chapter 3 of the thesis, many of the potentialities offered by our powerful holographic setup emerge clearly. The complex holographic intensity patterns are directly replicated into spatially structured surface reliefs onto the azopolymer film using circularly polarized light. In the typical illumination configuration, the highly focused illumination pattern (obtained through a 100X microscope objective) allows to reach a spatial resolution of few-hundreds of nanometers for the inscribed surface reliefs, opening to the possibility of employing this illumination configuration in photo-nanolithography. However, scalable surface reliefs can be simply achieved by using lens at lower magnification factors. The independent control of the polarization state and the intensity distribution of the holographic light patterns allowed underlining a non-trivial polarization dependent behavior of the mass migration phenomenon in our azopolymer. Depending on the actual relative directions between the local intensity gradient and the light polarization direction, an inversion in the mass migration direction has been found. In particular, in the case of polarization direction parallel the intensity gradient, the material moves from the regions at highest

intensity toward the regions at lower intensity. O the contrary, the material motion is completely inversed in the case of polarization direction orthogonal to the intensity gradient. The study of the growth dynamics of the surface reliefs in these two illumination configurations has shown a comparable growing rate. This is quite unexpected because the two illumination configurations can be assimilated to the p-p and s-s polarization configurations, which typically show very different mass migration efficiency it the SRG inscription experiments. Despite a similar inversion in the direction of the material movement has been described few times in literature, the holographic illumination setup used here has allowed for the first time its highlight in a very clear way. While every attempt toward its rationalization must necessary pass through the investigation of different azomaterials, the situation described, shows the potentialities that this illumination approach can have in the future studies on the mass migration phenomenon as a whole.

The second strategy presented in the thesis to achieve complex superficial textures is the light-driven reconfiguration of pre-patterned micro-volumes of the azopolymer under uniform light beam irradiation. In Chapter 4 has been demonstrated that the intensity/polarization dependence of the light-driven mass migration phenomenon occurring in this material can be used for finely tuning the three-dimensional geometry of soft-lithographic imprinted micro-cylinders. Both symmetric and asymmetric structures are achieved by using circular or linear polarized irradiating light. The deterministic control on the final structures has also demonstrated by the predictions of the phenomenological mass migration model described before. Its theoretical framework has resulted to be valid also in this uniform illumination conditions, where many other models would predict, instead, inefficient material movement. By tuning the laser fluence, controllable and directional superficial asymmetry can be induced onto the array of a single pristine micro-pillar array, even in a reversible way. The versatility offered by this light controlled surface structuring has been demonstrated, in Chapter 5, to be a tool of crucial relevance in order to control the wettability properties of the surfaces. In particular, a non-standard wetting phenomenon has been recognized as governing the wetting state of the pristine cylindrical pillars, while the structures obtained by tuning simple illumination parameters such as the light polarization state and the beam incidence angle had been demonstrated to induce a directional controlled wettability anisotropy. Despite the relatively simple experimental fabrication framework, phenomena such as unidirectional anisotropy and spreading were achieved onto the reconfigured microstructures. Furthermore, spatially structured intensity and polarization patterns allowed the design of tailored bidimensional anisotropic wetting paths. These nontrivial wetting applications usually require expensive and multistep

fabrication processes for tailoring the superficial geometry, and typically the obtained structures cannot be further tuned once fabricated. The soft imprinting technique used for azopolymer pristine texturing is based on the replica-molding from a single silicon master and permits the fabrication of hundreds of light-customizable samples, with a dramatic reduction of fabrication time and costs with respect to the standard lithographic methods. Besides the potential applications in many fields of research such as photonics, electronics, and biology, such reversible light-configurable surfaces can be used as a powerful tool for both experimental and theoretical studies relying on the topography-based superficial wetting design. Furthermore, the light-reconfigured azopolymer surfaces can be used as molding templates for soft-lithographic transfer of the texture on other materials, which can have improved mechanical and chemical properties required in specific applications.

Appendix A

Azopolymer used in the experiments

The polymer used all the mass-migration experiments reported in the thesis is an acrylic polymer bearing the photoresponsive azobenzene moieties as side chains of the polymeric backbone [8,12]. The chemical structure of the polymer is presented in Fig. A1(a). The azopolymer presents the typical azomaterial absorption spectrum (Fig. A1 (b)), with a maximum absorbance occurring at the wavelength around $\lambda_{max} \approx 370$ nm. All the samples having flat polymer surface are prepared in form of thin film (typical thickness <1 μm) by spin coating the polymer from a 1,1,2,2-tetrachloroethane solution onto a microscope coverslip. For the fabrication of the surfaces pre-patterned with the array of cylindrical micro-pillars reported in chapters 4 and 5, the polymer is dissolved (with a concentration of 10% by weight) in N-methyl-pirrolidone.

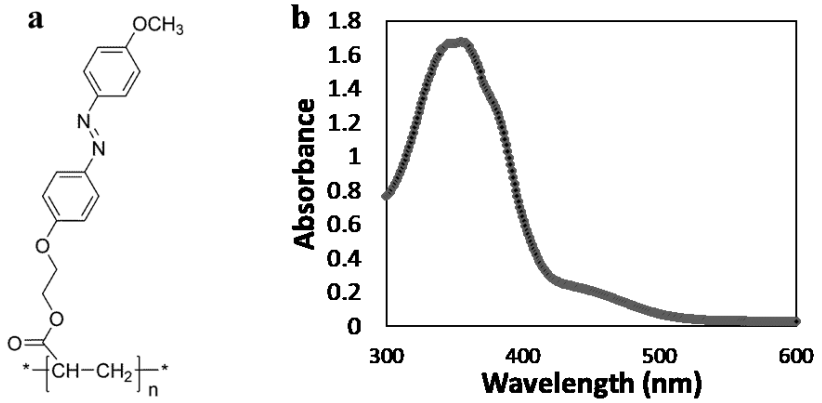

Fig. A1| Description of the azopolymer used in this thesis. (a) Chemical structure. (b) Uv/visible absorption spectrum.

Topographic characterization of the light-induced surface reliefs

The topography of the structured azopolymer surfaces is characterized by atomic-force microscopes (Alpha 300-RAS by WITec or XE-100 by Park Systems Corp.) equipped with a silicon cantilever operating in non-contact mode. The image analysis is performed by the SPM open-source software "Gwyddion".

Acknowledgements

The work reported in this thesis is the result of three years of very intense research activities which have been required a total involvement of my scientific and personal life. In this respect, the persons surrounding me in this journey have played a crucial role, believing in me when I did not and pushing me every day toward the awareness of my love for Science.

The first person I really want to acknowledge is my supervisor Prof. Pasqualino Maddalena. He has been my scientific guidance since my bachelor degree. I'm indebted to him and to his willingness to invest resources and time in my formation. During all these years I had also the opportunity to know and appreciate more and more his personality, besides his scientific abilities. We share also the common passion for football (and for Napoli team) which makes our discussions always a really interesting and funny mix of Science, football and life.

The other person to whom I owe so much is Dr. Antonio Ambrosio. His brilliant personality is my main scientific inspiration reason. Every confrontation with him is a collection of new ideas, new problems and, above all, new solutions. He has given to me the desire and the strength to go deep in the every scientific subject we have faced together. I want to acknowledge him also for the opportunities he gives to me for meeting other research realities, enriching greatly my personal and scientific experiences.

I wish to express my sincerest gratitude also to Dr. Fabio Borbone. He has been my lighthouse for every experiment I performed. Without him, his incredible abilities and his patience, the great majority of the results presented herein would never have been obtained. Special thanks go to all the colleagues I had the pleasure to work with: Dr. Felice Gesuele, Dr. Fulvia Villani, Prof. Corrado De Lisio, Prof. Marco D'Ischia, Prof. Dr. Alessandro Pezzella, Dr. Chiara Fedele, Dr. Giovanni De Gregorio. I want also to express my gratitude to Prof. Federico Capasso and Prof. Arri Priimagi for the hospitality during my research visits at Harvard University and at Tampere University of Technologies, respectively. A particular tank goes also to my friend Dr. Hao Zeng for the continuous input of new ideas and the encouragement to follow my way.

Acknowledgements

I absolutely need to express my gratitude to my Ph.D. colleagues Marco Chianese, Rosa Miele and Adriana Pecoraro (and our coffee machine). They have been of essential importance during this three years, sharing with me joys and pains of our study path, but above all the became my special friends.

Finally, the last lines of these pages are reserved to Claudia and to my family, to thank them for their love and their continuous and unconditional support.

Naples, 8 December 2017

Stefano Luigi Oscurato

List of publications

[1] M.L. Alfieri, R. Micillo, L. Panzella, O. Crescenzi, **S.L. Oscurato**, P. Maddalena, A.Napolitano, V.Ball, M. D'Ischia, *The structural basis of polydopamine film formation: probing 5,6-dihydroxyindole-based eumelanin type units and the porphyrin issue,* ACS Applied Materials & Interfaces, Article ASAP, DOI: 10.1021/acsami.7b09662.

[2] **S. L. Oscurato**, F. Borbone, P. Maddalena, A. Ambrosio; *Light-driven wettability tailoring of azopolymer surfaces with reconfigured three-dimensional posts,* ACS Applied Materials & Interfaces, 9 (35), pp 30133–30142, (2017).

[3] J..JJ. Nivas, F. Gesuele, E. Allahyari, **S.L. Oscurato**, R Fittipaldi, A. Vecchione, R. Bruzzese, S. Amoruso, *Effects of ambient air pressure on surface structures produced by ultrashort laser pulse irradiation,* Optics Letters, Vol. 42, Issue 14, pp. 2710-2713 (2017).

[4] **S. L. Oscurato**, F. Borbone, R. C. Devlin, F. Capasso, P. Maddalena, A. Ambrosio, *New microscopy technique based on position localization of scattering particles,* Optics Express, Vol. 25, Issue 10, pp. 11530-11549 (2017).

[5] R. C. Devlin, A. Ambrosio, D. Wintz, **S. L. Oscurato**, A. Y. Zhu, M. Khorasaninejad, J. Oh, P. Maddalena, and F. Capasso, *Spin-to-orbital angular momentum conversion in dielectric metasurfaces*, Optics Express, Vol. 25, Issue 1, pp. 377-393 (2017).

Conference Proceedings

[6] **S. L. Oscurato**, F. Borbone, P. Maddalena, A.Ambrosio, *Light driven directional mass transport of azo-benzene containing materials for complex tri-dimensional surface structures,* Proceedings of 9th Word Congress on Materials Science and Enegineering, Volume 6, Iussue 4, ISSN:2169-0022- June 2017.

[7] **S. L. Oscurato**, P. Maddalena, E. Orabona, A. Ambrosio, *Holographic Laser Scanning Microscopy,* Nano-Optics: Principles Enabling Basic Research and Applications, Springer, Dordrecht, pp 541-543, (2017).

References

1. A. Natansohn and P. Rochon, "Photoinduced Motions in Azo-Containing Polymers," Chem. Rev. **102**, 4139–4176 (2002).
2. K. G. Yager and C. J. Barrett, "Novel photo-switching using azobenzene functional materials," J. Photochem. Photobiol. Chem. **182**, 250–261 (2006).
3. S. Lee, H. S. Kang, and J.-K. Park, "Directional Photofluidization Lithography: Micro/Nanostructural Evolution by Photofluidic Motions of Azobenzene Materials," Adv. Mater. **24**, 2069–2103 (2012).
4. A. Priimagi and A. Shevchenko, "Azopolymer-based micro- and nanopatterning for photonic applications," J. Polym. Sci. Part B Polym. Phys. **52**, 163–182 (2014).
5. J. Vapaavuori, R. H. A. Ras, M. Kaivola, C. G. Bazuin, and A. Priimagi, "From partial to complete optical erasure of azobenzene–polymer gratings: effect of molecular weight," J. Mater. Chem. C **3**, 11011–11016 (2015).
6. P. Rochon, E. Batalla, and A. Natansohn, "Optically induced surface gratings on azoaromatic polymer films," Appl. Phys. Lett. **66**, 136–138 (1995).
7. D. Y. Kim, L. Li, X. L. Jiang, V. Shivshankar, J. Kumar, and S. K. Tripathy, "Polarized Laser Induced Holographic Surface Relief Gratings on Polymer Films," Macromolecules **28**, 8835–8839 (1995).
8. A. Ambrosio, L. Marrucci, F. Borbone, A. Roviello, and P. Maddalena, "Light-induced spiral mass transport in azo-polymer films under vortex-beam illumination," Nat. Commun. **3**, 989 (2012).
9. A. Ambrosio, S. Girardo, A. Camposeo, D. Pisignano, and P. Maddalena, "Controlling spontaneous surface structuring of azobenzene-containing polymers for large-scale nano-lithography of functional substrates," Appl. Phys. Lett. **102**, 093102 (2013).
10. S. Lee, H. S. Kang, A. Ambrosio, J.-K. Park, and L. Marrucci, "Directional Superficial Photofluidization for Deterministic Shaping of Complex 3D Architectures," ACS Appl. Mater. Interfaces **7**, 8209–8217 (2015).
11. F. Pirani, A. Angelini, F. Frascella, R. Rizzo, S. Ricciardi, and E. Descrovi, "Light-Driven Reversible Shaping of Individual Azopolymeric Micro-Pillars," Sci. Rep. **6**, 31702 (2016).
12. S. L. Oscurato, F. Borbone, P. Maddalena, and A. Ambrosio, "Light-Driven Wettability Tailoring of Azopolymer Surfaces with Reconfigured Three-Dimensional Posts," ACS Appl. Mater. Interfaces (2017).
13. S.-A. Lee, H. S. Kang, J.-K. Park, and S. Lee, "Vertically Oriented, Three-Dimensionally Tapered Deep-Subwavelength Metallic Nanohole Arrays Developed by Photofluidization Lithography," Adv. Mater. **26**, 7521–7528 (2014).

14. C. Rianna, A. Calabuig, M. Ventre, S. Cavalli, V. Pagliarulo, S. Grilli, P. Ferraro, and P. A. Netti, "Reversible Holographic Patterns on Azopolymers for Guiding Cell Adhesion and Orientation," ACS Appl. Mater. Interfaces **7**, 16984–16991 (2015).
15. C. J. Barrett, P. L. Rochon, and A. L. Natansohn, "Model of laser-driven mass transport in thin films of dye-functionalized polymers," J. Chem. Phys. **109**, 1505–1516 (1998).
16. T. G. Pedersen and P. M. Johansen, "Mean-Field Theory of Photoinduced Molecular Reorientation in Azobenzene Liquid Crystalline Side-Chain Polymers," Phys. Rev. Lett. **79**, 2470–2473 (1997).
17. S. Bian, J. M. Williams, D. Y. Kim, L. Li, S. Balasubramanian, J. Kumar, and S. Tripathy, "Photoinduced surface deformations on azobenzene polymer films," J. Appl. Phys. **86**, 4498–4508 (1999).
18. P. Lefin, C. Fiorini, and J.-M. Nunzi, "Anisotropy of the photo-induced translation diffusion of azobenzene dyes in polymer matrices," Pure Appl. Opt. J. Eur. Opt. Soc. Part A **7**, 71 (1998).
19. M. L. Juan, J. Plain, R. Bachelot, P. Royer, S. K. Gray, and G. P. Wiederrecht, "Multiscale Model for Photoinduced Molecular Motion in Azo Polymers," ACS Nano **3**, 1573–1579 (2009).
20. H. Galinski, A. Ambrosio, P. Maddalena, I. Schenker, R. Spolenak, and F. Capasso, "Instability-induced pattern formation of photoactivated functional polymers," Proc. Natl. Acad. Sci. **111**, 17017–17022 (2014).
21. J. W. Goodman, *Introduction to Fourier Optics* (Roberts and Company Publishers, 2005).
22. C. Hubert, C. Fiorini-Debuisschert, I. Maurin, J.-M. Nunzi, and P. Raimond, "Spontaneous Patterning of Hexagonal Structures in an Azo-Polymer Using Light-Controlled Mass Transport," Adv. Mater. **14**, 729–732 (2002).
23. Y. Gritsai, L. M. Goldenberg, and J. Stumpe, "Efficient single-beam light manipulation of 3D microstructures in azobenzene-containing materials," Opt. Express **19**, 18687–18695 (2011).
24. G. S. Kumar and D. C. Neckers, "Photochemistry of azobenzene-containing polymers," Chem. Rev. **89**, 1915–1925 (1989).
25. T. Fujino, S. Y. Arzhantsev, and T. Tahara, "Femtosecond Time-Resolved Fluorescence Study of Photoisomerization of trans-Azobenzene," J. Phys. Chem. A **105**, 8123–8129 (2001).
26. G. S. Hartley, "The Cis-form of Azobenzene," Nature **140**, 281–281 (1937).
27. G. S. Hartley and R. J. W. L. Fèvre, "119. The dipole moments of cis - and trans - azobenzenes and of some related compounds," J. Chem. Soc. Resumed **0**, 531–535 (1939).
28. T. Hugel, N. B. Holland, A. Cattani, L. Moroder, M. Seitz, and H. E. Gaub, "Single-Molecule Optomechanical Cycle," Science **296**, 1103–1106 (2002).
29. N. B. Holland, T. Hugel, G. Neuert, A. Cattani-Scholz, C. Renner, D. Oesterhelt, L. Moroder, M. Seitz, and H. E. Gaub, "Single Molecule Force Spectroscopy of Azobenzene Polymers: Switching Elasticity of Single Photochromic Macromolecules," Macromolecules **36**, 2015–2023 (2003).

References

30. T. Ikeda and O. Tsutsumi, "Optical Switching and Image Storage by Means of Azobenzene Liquid-Crystal Films," Science **268**, 1873–1875 (1995).
31. A. Sobolewska, J. Zawada, S. Bartkiewicz, and Z. Galewski, "Mechanism of Photochemical Phase Transition of Single-Component Phototropic Liquid Crystals Studied by Means of Holographic Grating Recording," J. Phys. Chem. C **117**, 10051–10058 (2013).
32. C. L. van Oosten, K. D. Harris, C. W. M. Bastiaansen, and D. J. Broer, "Glassy photomechanical liquid-crystal network actuators for microscale devices," Eur. Phys. J. E **23**, 329–336 (2007).
33. C. L. van Oosten, C. W. M. Bastiaansen, and D. J. Broer, "Printed artificial cilia from liquid-crystal network actuators modularly driven by light," Nat. Mater. **8**, 677–682 (2009).
34. Y. Zhang, J. Xu, F. Cheng, R. Yin, C.-C. Yen, and Y. Yu, "Photoinduced bending behavior of crosslinked liquid-crystalline polymer films with a long spacer," J. Mater. Chem. **20**, 7123–7130 (2010).
35. H. Zeng, O. M. Wani, P. Wasylczyk, and A. Priimagi, "Light-Driven, Caterpillar-Inspired Miniature Inching Robot," Macromol. Rapid Commun. (2017).
36. O. M. Wani, H. Zeng, and A. Priimagi, "A light-driven artificial flytrap," Nat. Commun. **8**, ncomms15546 (2017).
37. K. G. Yager and C. J. Barrett, "Temperature modeling of laser-irradiated azo-polymer thin films," J. Chem. Phys. **120**, 1089–1096 (2003).
38. N. K. Viswanathan, D. Y. Kim, S. Bian, J. Williams, W. Liu, L. Li, L. Samuelson, J. Kumar, and S. K. Tripathy, "Surface relief structures on azo polymer films," J. Mater. Chem. **9**, 1941–1955 (1999).
39. F. Fabbri, Y. Lassailly, K. Lahlil, J. P. Boilot, and J. Peretti, "Alternating photoinduced mass transport triggered by light polarization in azobenzene containing sol-gel films," Appl. Phys. Lett. **96**, 081908 (2010).
40. F. Fabbri, D. Garrot, K. Lahlil, J. P. Boilot, Y. Lassailly, and J. Peretti, "Evidence of Two Distinct Mechanisms Driving Photoinduced Matter Motion in Thin Films Containing Azobenzene Derivatives," J. Phys. Chem. B **115**, 1363–1367 (2011).
41. F. Fabbri, Y. Lassailly, S. Monaco, K. Lahlil, J. P. Boilot, and J. Peretti, "Kinetics of photoinduced matter transport driven by intensity and polarization in thin films containing azobenzene," Phys. Rev. B **86**, 115440 (2012).
42. N. S. Yadavalli and S. Santer, "In-situ atomic force microscopy study of the mechanism of surface relief grating formation in photosensitive polymer films," J. Appl. Phys. **113**, 224304 (2013).
43. S. Bian, L. Li, J. Kumar, D. Y. Kim, J. Williams, and S. K. Tripathy, "Single laser beam-induced surface deformation on azobenzene polymer films," Appl. Phys. Lett. **73**, 1817–1819 (1998).
44. T. Ubukata, T. Seki, and K. Ichimura, "Surface Relief Gratings in Host–Guest Supramolecular Materials," Adv. Mater. **12**, 1675–1678 (2000).
45. D. Bublitz, B. Fleck, and L. Wenke, "A model for surface-relief formation in azobenzene polymers," Appl. Phys. B **72**, 931–936 (2001).

46. A. Ambrosio, P. Maddalena, and L. Marrucci, "Molecular model for light-driven spiral mass transport in azopolymer films," Phys. Rev. Lett. **110**, 146102 (2013).
47. J. Kumar, L. Li, X. L. Jiang, D.-Y. Kim, T. S. Lee, and S. Tripathy, "Gradient force: The mechanism for surface relief grating formation in azobenzene functionalized polymers," Appl. Phys. Lett. **72**, 2096–2098 (1998).
48. S. Bian, W. Liu, J. Williams, L. Samuelson, J. Kumar, and S. Tripathy, "Photoinduced Surface Relief Grating on Amorphous Poly(4-phenylazophenol) Films," Chem. Mater. **12**, 1585–1590 (2000).
49. K. Yang, S. Yang, and J. Kumar, "Formation mechanism of surface relief structures on amorphous azopolymer films," Phys. Rev. B **73**, 165204 (2006).
50. J. F. Nye and M. V. Berry, "Dislocations in wave trains," Proc R Soc Lond A **336**, 165–190 (1974).
51. L. Novotny and B. Hecht, *Principles of Nano-Optics* (Cambridge University Press, 2006).
52. A. Yariv, *Quantum Electronics* (John Wiley & Sons, Incorporated, 1975).
53. L. Marrucci, C. Manzo, and D. Paparo, "Optical Spin-to-Orbital Angular Momentum Conversion in Inhomogeneous Anisotropic Media," Phys. Rev. Lett. **96**, 163905 (2006).
54. S. Franke-Arnold, L. Allen, and M. Padgett, "Advances in optical angular momentum," Laser Photonics Rev. **2**, 299–313 (2008).
55. A. Ambrosio and P. Maddalena, "Effect of radial defect lines in the focalization of unitary polarization order light beams," Appl. Phys. Lett. **98**, 091108 (2011).
56. B. Bellini, J. Ackermann, H. Klein, C. Grave, P. Dumas, and V. Safarov, "Light-induced molecular motion of azobenzene-containing molecules: a random-walk model," J. Phys. Condens. Matter **18**, S1817 (2006).
57. N. R. Heckenberg, R. McDuff, C. P. Smith, and A. G. White, "Generation of optical phase singularities by computer-generated holograms," Opt. Lett. **17**, 221–223 (1992).
58. J. Lin, P. Genevet, M. A. Kats, N. Antoniou, and F. Capasso, "Nanostructured Holograms for Broadband Manipulation of Vector Beams," Nano Lett. **13**, 4269–4274 (2013).
59. M. V. Berry and F. R. S, "Quantal phase factors accompanying adiabatic changes," Proc R Soc Lond A **392**, 45–57 (1984).
60. R. C. Devlin, A. Ambrosio, D. Wintz, S. L. Oscurato, A. Y. Zhu, M. Khorasaninejad, J. Oh, P. Maddalena, and F. Capasso, "Spin-to-orbital angular momentum conversion in dielectric metasurfaces," Opt. Express **25**, 377–393 (2017).
61. R. Yamaguchi, T. Nose, and S. Sato, "Liquid Crystal Polarizers with Axially Symmetrical Properties," Jpn. J. Appl. Phys. **28**, 1730 (1989).
62. M. Stalder and M. Schadt, "Linearly polarized light with axial symmetry generated by liquid-crystal polarization converters," Opt. Lett. **21**, 1948–1950 (1996).
63. A. Bouhelier, M. R. Beversluis, and L. Novotny, "Near-field scattering of longitudinal fields," Appl. Phys. Lett. **82**, 4596–4598 (2003).

References

64. N. Anderson, A. Hartschuh, and L. Novotny, "Chirality Changes in Carbon Nanotubes Studied with Near-Field Raman Spectroscopy," Nano Lett. **7**, 577–582 (2007).
65. D. Gabor, "A New Microscopic Principle," Nature **161**, 777–778 (1948).
66. E. R. Dufresne, G. C. Spalding, M. T. Dearing, S. A. Sheets, and D. G. Grier, "Computer-generated holographic optical tweezer arrays," Rev. Sci. Instrum. **72**, 1810–1816 (2001).
67. J. Leach, K. Wulff, G. Sinclair, P. Jordan, J. Courtial, L. Thomson, G. Gibson, K. Karunwi, J. Cooper, Z. J. Laczik, and M. Padgett, "Interactive approach to optical tweezers control," Appl. Opt. **45**, 897–903 (2006).
68. R. W.Gerchberg and W. O. Saxton, "A practical algorithm for the determination of the phase from image and diffraction plane pictures," Optik **35**, 237–246 (1972).
69. B. E. A. Saleh and M. C. Teich, *Fundamentals of Photonics*, Wiley Series in Pure and Applied Optics (John Wiley & Sons, Inc., 1991).
70. R. D. Leonardo, F. Ianni, and G. Ruocco, "Computer generation of optimal holograms for optical trap arrays," Opt. Express **15**, 1913–1922 (2007).
71. F. J. Salgado-Remacha, "Reducing the variability in random-phase initialized Gerchberg-Saxton Algorithm," Opt. Laser Technol. **85**, 30–34 (2016).
72. E. Orabona, A. Ambrosio, A. Longo, G. Carotenuto, L. Nicolais, and P. Maddalena, "Holographic patterning of graphene-oxide films by light-driven reduction," Opt. Lett. **39**, 4263–4266 (2014).
73. J. W. Goodman, "Some fundamental properties of speckle," J. Opt. Soc. Am. **66**, 1145 (1976).
74. J. Amako, H. Miura, and T. Sonehara, "Speckle-noise reduction on kinoform reconstruction using a phase-only spatial light modulator," Appl. Opt. **34**, 3165–3171 (1995).
75. S. L. Oscurato, F. Borbone, R. C. Devlin, F. Capasso, P. Maddalena, and A. Ambrosio, "New microscopy technique based on position localization of scattering particles," Opt. Express **25**, 11530–11549 (2017).
76. M. Draijer, E. Hondebrink, T. van Leeuwen, and W. Steenbergen, "Review of laser speckle contrast techniques for visualizing tissue perfusion," Lasers Med. Sci. **24**, 639–651 (2009).
77. D. A. Boas and A. K. Dunn, "Laser speckle contrast imaging in biomedical optics," J. Biomed. Opt. **15**, (2010).
78. H. S. Kang, S. Lee, S.-A. Lee, and J.-K. Park, "Multi-Level Micro/Nanotexturing by Three-Dimensionally Controlled Photofluidization and its Use in Plasmonic Applications," Adv. Mater. **25**, 5490–5497 (2013).
79. H. S. Kang, S. Lee, and J.-K. Park, "Monolithic, Hierarchical Surface Reliefs by Holographic Photofluidization of Azopolymer Arrays: Direct Visualization of Polymeric Flows," Adv. Funct. Mater. **21**, 4412–4422 (2011).
80. N. Tsutsumi and A. Fujihara, "Pulsed laser induced spontaneous gratings on a surface of azobenzene polymer," Appl. Phys. Lett. **85**, 4582–4584 (2004).
81. R. Barille, J.-M. Nunzi, S. Ahmadi-Kandjani, E. Ortyl, and S. Kucharski, "One step inscription of surface relief microgratings," Opt. Commun. **280**, 217–220 (2007).

82. C. Hubert, C. Fiorini-Debuisschert, L. Rocha, P. Raimond, and J.-M. Nunzi, "Spontaneous photoinduced patterning of azo-dye polymer films: the facts," JOSA B **24**, 1839–1846 (2007).
83. H. Leblond, R. Barille, S. Ahmadi-Kandjani, J.-M. Nunzi, E. Ortyl, and S. Kucharski, "Spontaneous formation of optically induced surface relief gratings," J. Phys. B At. Mol. Opt. Phys. **42**, 205401 (2009).
84. A. Ambrosio, P. Maddalena, A. Carella, F. Borbone, A. Roviello, M. Polo, A. A. R. Neves, A. Camposeo, and D. Pisignano, "Two-Photon Induced Self-Structuring of Polymeric Films Based on Y-Shape Azobenzene Chromophore," J. Phys. Chem. C **115**, 13566–13570 (2011).
85. L. Mazaheri, R. G. Sabat, O. Lebel, and J.-M. Nunzi, "Unraveling the nucleation and growth of spontaneous surface relief gratings," Opt. Mater. **62**, 378–391 (2016).
86. M. Bolle and S. Lazare, "Characterization of submicrometer periodic structures produced on polymer surfaces with low-fluence ultraviolet laser radiation," J. Appl. Phys. **73**, 3516–3524 (1993).
87. J. J. Nivas, F. Gesuele, E. Allahyari, S. L. Oscurato, R. Fittipaldi, A. Vecchione, R. Bruzzese, and S. Amoruso, "Effects of ambient air pressure on surface structures produced by ultrashort laser pulse irradiation," Opt. Lett. **42**, 2710–2713 (2017).
88. L. Mazaheri, S. R. Bobbara, O. Lebel, and J.-M. Nunzi, "Photoinduction of spontaneous surface relief gratings on Azo DR1 glass," Opt. Lett. **41**, 2958–2961 (2016).
89. A. Ambrosio, R. C. Devlin, F. Capasso, and W. L. Wilson, "Observation of Nanoscale Refractive Index Contrast via Photoinduced Force Microscopy," ACS Photonics **4**, 846–851 (2017).
90. R. Barillé, R. Janik, S. Kucharski, J. Eyer, and F. Letournel, "Photo-responsive polymer with erasable and reconfigurable micro- and nano-patterns: An in vitro study for neuron guidance," Colloids Surf. B Biointerfaces **88**, 63–71 (2011).
91. M. Guo, Z. Xu, and X. Wang, "Photofabrication of Two-Dimensional Quasi-Crystal Patterns on UV-Curable Molecular Azo Glass Films," Langmuir **24**, 2740–2745 (2008).
92. A. Ambrosio, A. Camposeo, A. Carella, F. Borbone, D. Pisignano, A. Roviello, and P. Maddalena, "Realization of submicrometer structures by a confocal system on azopolymer films containing photoluminescent chromophores," J. Appl. Phys. **107**, 083110 (2010).
93. C. Fedele, M. De Gregorio, P. A. Netti, S. Cavalli, and C. Attanasio, "Azopolymer photopatterning for directional control of angiogenesis," Acta Biomater. **63**, 317–325 (2017).
94. S. Lee, Y.-C. Jeong, and J.-K. Park, "Facile fabrication of close-packed microlens arrays using photoinduced surface relief structures as templates," Opt. Express **15**, 14550–14559 (2007).
95. S. Y. Chou and Q. Xia, "Improved nanofabrication through guided transient liquefaction," Nat. Nanotechnol. **3**, 295–300 (2008).

References

96. X. Kong, X. Wang, T. Luo, Y. Yao, L. Li, and S. Lin, "Photomanipulated Architecture and Patterning of Azopolymer Array," ACS Appl. Mater. Interfaces **9**, 19345–19353 (2017).
97. Y. Li, Y. He, X. Tong, and X. Wang, "Photoinduced Deformation of Amphiphilic Azo Polymer Colloidal Spheres," J. Am. Chem. Soc. **127**, 2402–2403 (2005).
98. J. Li, L. Chen, J. Xu, K. Wang, X. Wang, X. He, H. Dong, S. Lin, and J. Zhu, "Photoguided Shape Deformation of Azobenzene-Containing Polymer Microparticles," Langmuir **31**, 13094–13100 (2015).
99. W. Wang, Y. Yao, T. Luo, L. Chen, J. Lin, L. Li, and S. Lin, "Deterministic Reshaping of Breath Figure Arrays by Directional Photomanipulation," ACS Appl. Mater. Interfaces **9**, 4223–4230 (2017).
100. S. G. Sorkhabi, R. Barille, S. Ahmadi-Kandjani, S. Zielinska, and E. Ortyl, "A new method for patterning azopolymer thin film surfaces," Opt. Mater. **66**, 573–579 (2017).
101. D. Qin, Y. Xia, and G. M. Whitesides, "Soft lithography for micro- and nanoscale patterning," Nat. Protoc. **5**, 491–502 (2010).
102. F. Pirani, A. Angelini, S. Ricciardi, F. Frascella, and E. Descrovi, "Laser-induced anisotropic wettability on azopolymeric micro-structures," Appl. Phys. Lett. **110**, 101603 (2017).
103. V. Jokinen, M. Leinikka, and S. Franssila, "Microstructured Surfaces for Directional Wetting," Adv. Mater. **21**, 4835–4838 (2009).
104. L. Courbin, E. Denieul, E. Dressaire, M. Roper, A. Ajdari, and H. A. Stone, "Imbibition by polygonal spreading on microdecorated surfaces," Nat. Mater. **6**, 661–664 (2007).
105. K.-H. Chu, R. Xiao, and E. N. Wang, "Uni-directional liquid spreading on asymmetric nanostructured surfaces," Nat. Mater. **9**, 413–417 (2010).
106. T. Kim and K. Y. Suh, "Unidirectional wetting and spreading on stooped polymer nanohairs," Soft Matter **5**, 4131–4135 (2009).
107. T. Sun, L. Feng, X. Gao, and L. Jiang, "Bioinspired Surfaces with Special Wettability," Acc. Chem. Res. **38**, 644–652 (2005).
108. L. Feng, S. Li, Y. Li, H. Li, L. Zhang, J. Zhai, Y. Song, B. Liu, L. Jiang, and D. Zhu, "Super-Hydrophobic Surfaces: From Natural to Artificial," Adv. Mater. **14**, 1857–1860 (2002).
109. M. J. Hancock, K. Sekeroglu, and M. C. Demirel, "Bioinspired Directional Surfaces for Adhesion, Wetting, and Transport," Adv. Funct. Mater. **22**, 2223–2234 (2012).
110. S. Wang, K. Liu, X. Yao, and L. Jiang, "Bioinspired Surfaces with Superwettability: New Insight on Theory, Design, and Applications," Chem. Rev. **115**, 8230–8293 (2015).
111. R. N. Wenzel, "RESISTANCE OF SOLID SURFACES TO WETTING BY WATER," Ind. Eng. Chem. **28**, 988–994 (1936).
112. A. B. D. Cassie and S. Baxter, "Wettability of porous surfaces," Trans. Faraday Soc. **40**, 546–551 (1944).

113. L. Barbieri, E. Wagner, and P. Hoffmann, "Water Wetting Transition Parameters of Perfluorinated Substrates with Periodically Distributed Flat-Top Microscale Obstacles," Langmuir **23**, 1723–1734 (2007).
114. S.-Z. Wu, D. Wu, J. Yao, Q.-D. Chen, J.-N. Wang, L.-G. Niu, H.-H. Fang, and H.-B. Sun, "One-Step Preparation of Regular Micropearl Arrays for Two-Direction Controllable Anisotropic Wetting," Langmuir **26**, 12012–12016 (2010).
115. A. M. Telford, B. S. Hawkett, C. Such, and C. Neto, "Mimicking the Wettability of the Rose Petal using Self-assembly of Waterborne Polymer Particles," Chem. Mater. **25**, 3472–3479 (2013).
116. J. Choi, W. Jo, S. Y. Lee, Y. S. Jung, S.-H. Kim, and H.-T. Kim, "Flexible and Robust Superomniphobic Surfaces Created by Localized Photofluidization of Azopolymer Pillars," ACS Nano **11**, 7821–7828 (2017).
117. T. Young, "III. An essay on the cohesion of fluids," Philos. Trans. R. Soc. Lond. **95**, 65–87 (1805).
118. *Capillarity and Wetting Phenomena - Drops, Bubbles, | Pierre-Gilles de Gennes | Springer* (n.d.).
119. L. Feng, Y. Zhang, J. Xi, Y. Zhu, N. Wang, F. Xia, and L. Jiang, "Petal Effect: A Superhydrophobic State with High Adhesive Force," Langmuir **24**, 4114–4119 (2008).
120. A. Tuteja, W. Choi, M. Ma, J. M. Mabry, S. A. Mazzella, G. C. Rutledge, G. H. McKinley, and R. E. Cohen, "Designing Superoleophobic Surfaces," Science **318**, 1618–1622 (2007).
121. A. Tuteja, W. Choi, J. M. Mabry, G. H. McKinley, and R. E. Cohen, "Robust omniphobic surfaces," Proc. Natl. Acad. Sci. **105**, 18200–18205 (2008).
122. L. Cao, H.-H. Hu, and D. Gao, "Design and Fabrication of Micro-textures for Inducing a Superhydrophobic Behavior on Hydrophilic Materials," Langmuir **23**, 4310–4314 (2007).
123. Josiah Willard Gibbs, *Scientific Papers of J. Willard Gibbs ...* (Longmans, Green and co, 1906).
124. V. Liimatainen, V. Sariola, and Q. Zhou, "Controlling Liquid Spreading Using Microfabricated Undercut Edges," Adv. Mater. **25**, 2275–2278 (2013).
125. Y. Chen, B. He, J. Lee, and N. A. Patankar, "Anisotropy in the wetting of rough surfaces," J. Colloid Interface Sci. **281**, 458–464 (2005).
126. Y. Zhao, Q. Lu, M. Li, and X. Li, "Anisotropic Wetting Characteristics on Submicrometer-Scale Periodic Grooved Surface," Langmuir **23**, 6212–6217 (2007).
127. J. Y. Chung, J. P. Youngblood, and C. M. Stafford, "Anisotropic wetting on tunable micro-wrinkled surfaces," Soft Matter **3**, 1163–1169 (2007).
128. W. Li, G. Fang, Y. Li, and G. Qiao, "Anisotropic Wetting Behavior Arising from Superhydrophobic Surfaces: Parallel Grooved Structure," J. Phys. Chem. B **112**, 7234–7243 (2008).
129. J. Choi, W. Cho, Y. S. Jung, H. S. Kang, and H.-T. Kim, "Direct Fabrication of Micro/Nano-Patterned Surfaces by Vertical-Directional Photofluidization of Azobenzene Materials," ACS Nano **11**, 1320–1327 (2017).

130. A. F. Stalder, G. Kulik, D. Sage, L. Barbieri, and P. Hoffmann, "A snake-based approach to accurate determination of both contact points and contact angles," Colloids Surf. Physicochem. Eng. Asp. **286**, 92–103 (2006).
131. S. Suzuki and K. Ueno, "Apparent Contact Angle Calculated from a Water Repellent Model with Pinning Effect," Langmuir **33**, 138–143 (2017).
132. S. Wu, "Calculation of interfacial tension in polymer systems," J. Polym. Sci. Part C Polym. Symp. **34**, 19–30 (1971).
133. H. Mei, D. Luo, P. Guo, C. Song, C. Liu, Y. Zheng, and L. Jiang, "Multi-level micro-/nanostructures of butterfly wings adapt at low temperature to water repellency," Soft Matter **7**, 10569–10573 (2011).
134. D.-K. Lee, E.-H. Lee, and Y. H. Cho, "A superoleophobic surface with anisotropic flow of hexadecane droplets," Microsyst. Technol. **23**, 421–427 (2017).
135. D. Bodas and C. Khan-Malek, "Hydrophilization and hydrophobic recovery of PDMS by oxygen plasma and chemical treatment—An SEM investigation," Sens. Actuators B Chem. **123**, 368–373 (2007).
136. V. Jokinen, P. Suvanto, and S. Franssila, "Oxygen and nitrogen plasma hydrophilization and hydrophobic recovery of polymers," Biomicrofluidics **6**, 016501-016501-10 (2012).
137. D. Xia, X. He, Y.-B. Jiang, G. P. Lopez, and S. R. J. Brueck, "Tailoring Anisotropic Wetting Properties on Submicrometer-Scale Periodic Grooved Surfaces," Langmuir **26**, 2700–2706 (2010).